



**HAL**  
open science

# Modeling and monitoring of the aging of Li-ion accumulators by coupling with a dual-tank model

Joël-Louis Kone

► **To cite this version:**

Joël-Louis Kone. Modeling and monitoring of the aging of Li-ion accumulators by coupling with a dual-tank model. Materials Science [cond-mat.mtrl-sci]. Université Grenoble Alpes [2020-..], 2021. English. NNT: 2021GRALI003 . tel-03192887

**HAL Id: tel-03192887**

**<https://theses.hal.science/tel-03192887>**

Submitted on 8 Apr 2021

**HAL** is a multi-disciplinary open access archive for the deposit and dissemination of scientific research documents, whether they are published or not. The documents may come from teaching and research institutions in France or abroad, or from public or private research centers.

L'archive ouverte pluridisciplinaire **HAL**, est destinée au dépôt et à la diffusion de documents scientifiques de niveau recherche, publiés ou non, émanant des établissements d'enseignement et de recherche français ou étrangers, des laboratoires publics ou privés.



## THÈSE

Pour obtenir le grade de

### DOCTEUR DE L'UNIVERSITÉ GRENOBLE ALPES

Spécialité : 2MGE : Matériaux, Mécanique, Génie civil,  
Electrochimie

Arrêté ministériel : 25 mai 2016

Présentée par

**Joël-Louis KONE**

Thèse dirigée par **Yann BULTEL**, Professeur Grenoble INP  
et codirigée par **Maxime MONTARU**  
et **Sébastien FIETTE**

préparée au sein du **Laboratoire CEA Grenoble / LITEN**  
dans l'**École Doctorale I-MEP2 - Ingénierie - Matériaux,**  
**Mécanique, Environnement, Énergétique, Procédés,**  
**Production**

### **Modélisation et suivi du vieillissement d'accumulateurs Li-ions par couplage avec modèle Dual-tank**

### **Modeling and monitoring of the aging of Li- ion accumulators by coupling with a dual- tank model**

Thèse soutenue publiquement le **8 janvier 2021**,  
devant le jury composé de :

**Monsieur YANN BULTEL**

PROFESSEUR DES UNIVERSITES, GRENOBLE INP, Directeur de  
thèse

**Monsieur PASCAL VENET**

PROFESSEUR DES UNIVERSITES, UNIVERSITE LYON 1 - CLAUDE  
BERNARD, Président

**Monsieur SERGE PELISSIER**

DIRECTEUR DE RECHERCHE, UNIVERSITE GUSTAVE EIFFEL,  
Rapporteur

**Monsieur CHRISTOPHE FORGEZ**

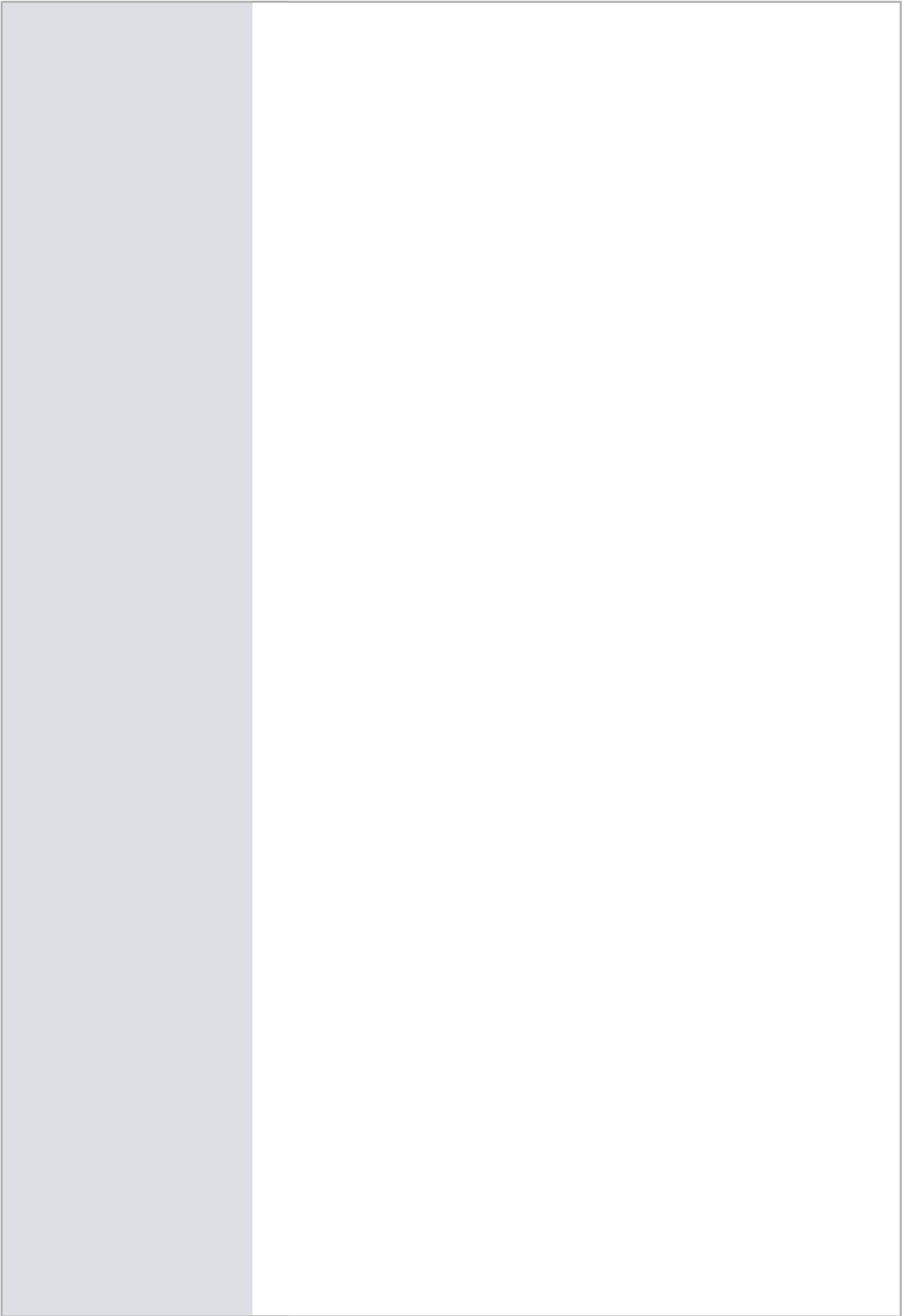
PROFESSEUR DES UNIVERSITES, UNIVERSITE DE TECHNOLOGIE  
DE COMPIEGNE, Rapporteur

**Madame ODILE CAPRON**

INGENIEUR DOCTEUR, VITO/EnergyVille, Examinatrice

**Madame ISABEL JIMENEZ GORDON**

INGENIEUR DOCTEUR, TECHNOCENTRE RENAULT, Examinatrice



A mon père et à mon frère jumeau

A tous mes amis

A tous ceux que j'aime

“Sometimes you just don't know the answer

‘Till someone's on their knees and asks you”

Champagne problems, Taylor Swift.



## **ACKNOWLEDGMENTS**

This work was conducted at the French Alternative Energies and Atomic Energy Commission(CEA-CEA Grenoble), within the Laboratory for Electrochemical Storage based at the National Institute of Solar Energy(INES).

I would like to thank Professor Yann BULTEL for his leadership in this work. His calm has always been something strange to me and I wish I could be as wise as he is. Thank you for always having me express my ideas whenever I felt the need to. I would express my gratitude to him for his scientific rigor and for his availability to supervise this manuscript.

I would like to thank my supervisors MAXIME MONTARU and SEBASTIEN FIETTE. Thank you for the time you dedicated to my training on MATLAB and all the brilliant ideas you both brought. I will never forget all those quiet times I was able to talk to you Maxime, a very pleasant moment.

I am very grateful to MATHIAS GERARD and JEAN-MARIE KLEIN for making my relationships with the laboratory so easy. I benefited from their experience, patience, but above all their great sense of listening to my feelings.

A special thanks to the MOBICUS PROJECT partners, without you, I would not have been able to access those riches amount of experimental data for my models.

To all my colleagues at INES and Grenoble, I spent such a special time, I cannot thank you enough. I also want to thank my friends for their support.

Finally, I dedicate this thesis to my twin brother, the love of my life.

To my twin brother  
SIMON-PIERRE KONE

## ABSTRACT

The battery models used in system studies are generally based on one-tank OCV models coupled with semi-empirical aging models predicting the evolution of the tank's capacity. In these models, the state-of-health of a cell is therefore represented by a single value, which is too limiting. Dual-tank OCV models are another type of models used in the literature. These models are useful to consider the modification of the OCV signature depending on the battery degradation path. Coupling dual-tank OCV models with aging models allows to predict variables related to the electrodes for the prognosis of the battery SOH. In this work, semi-empirical models and aging model used to describe the influence of SEI layer are coupled with a dual-tank OCV model. The semi-empirical approach aims to directly predict the evolution electrodes capacities along with aging electrodes. The approach, inspired by physics, introduces the notion of parasitic current at the origin of the loss of lithium inventory and aims to predict the offset between the electrode potentials signals. These different approaches are implemented with the experimental results of the MOBICUS project, a French national project on aging modeling of a production graphite-NMC/LMO battery.

*Keywords: Lithium-ion batteries, calendar aging model, prognostic model, loss of lithium inventory, loss of active material, SEI growth, open-circuit voltage model, electrodes aging, dual-tank model, Physics-based model.*

# Table des matières

GENERAL INTRODUCTION .....	4
CHAPTER 1: STATE-OF-THE-ART AND OBJECTIVES OF THE STUDY .....	6
Introduction .....	7
I.1. Lithium-ion battery presentation.....	7
I.2. Aging of Li-ion batteries.....	8
I.2.1. Aging mechanisms on the negative and positive electrode.....	8
I.2.2. Degradation modes on the electrodes.....	10
I.2.3. Aging modes .....	10
I.2.4. OCV measurements at different aging states .....	11
I.3. Prognosis of lithium-ion batteries SOH and OCV .....	13
I.3.1. One-tank OCV and aging models .....	13
I.3.1.1. One-tank OCV model.....	13
I.3.1.2. One-tank capacity aging model .....	14
I.3.1.3. One-tank aging models limitation .....	18
I.3.2. Dual-tank OCV and aging models.....	18
I.3.2.1. Dual-tank OCV model .....	18
I.3.2.2. Dual-tank aging model .....	20
I.4. Purpose of this thesis.....	22
CHAPTER 2: MOBICUS PROJECT PRESENTATION AND EXPERIMENTAL AGING RESULTS .....	23
INTRODUCTION .....	24
II.1. MOBICUS PROJECT.....	24
II.1.1. Presentation and aims of the project.....	24
II.1.2. Production Gr/NMC-LMO cell and coin cells manufacture .....	24
II.1.2.1. Production cell characteristics .....	24
II.1.2.2. Coin cells manufacture .....	25
II.2. Protocol of check-up on 43 Ah Gr/NMC-LMO for aging tests.....	26
II.3. Aging campaign and experimental results.....	27
II.3.1. Experimental measurements of the cell SOH .....	28
II.3.1.1. Fixed calendar conditions.....	28
II.3.1.2. Thermal cycling, fixed SOC .....	30
II.3.1.3. Variable SOC, fixed temperature.....	32
II.3.2. Experimental measurements of the cell voltage at C-10 .....	33
CHAPTER 3: ONE-TANK AGING MODEL .....	34
Introduction .....	35
III.1. MOBICUS aging model.....	35
III.1.1. MOBICUS aging laws .....	35
III.1.1.1. Degradation rate $J_{cal}$ .....	35
III.1.1.2. Degradation loss function $f_{deg}$ .....	36
III.1.2. Identification of the parameters of the MOBICUS aging model.....	36

III.1.2.1.	Identification method and results .....	36
III.1.2.2.	Experimental and simulated cell SOH from the MOBICUS aging model.....	38
III.1.2.3.	MOBICUS aging model error .....	40
III.1.3.	Model validation .....	41
III.2.	One-tank aging model.....	42
III.2.1.	One-tank aging model laws.....	42
III.2.1.1.	Degradation rate $J_{cal}$ .....	42
III.2.1.2.	Degradation loss function $f_{deg}$ .....	43
III.2.2.	One-tank aging model parameters identification .....	43
III.2.2.1.	Identification method and results .....	43
III.2.2.2.	Experimental and simulated cell SOH from the one-tank aging model.....	47
III.2.2.3.	One-tank aging model error .....	48
III.2.3.	Validation of the one-tank aging model.....	49
III.3.	Comparison of the MOBICUS aging model prediction versus One- tank aging model .....	50
III.3.1.	Identification process at 60°C and 65% of SOC .....	50
III.3.2.	Validation process for the thermal cycling condition at SOC 65% .....	51
	Conclusion.....	53
	CHAPTER 4: STUDY OF A COUPLING BETWEEN A DUAL-TANK OCV MODEL AND CALENDAR EMPIRICAL AGING MODEL.....	54
	Introduction .....	55
IV.1.	Dual-tank OCV model .....	55
IV.1.1.	Model presentation .....	55
IV.1.2.	Parameter's identification of the dual-tank model .....	57
IV.1.2.1.	Identification method.....	57
IV.1.2.2.	Dual-tank parameters evolution with aging .....	58
IV.1.2.3.	Validation from the literature .....	61
IV.1.2.4.	Influence of the degradation path.....	62
IV.2.	Dual-tank aging model.....	64
IV.2.1.	Dual-tank aging model equations .....	64
IV.2.2.	Parameters identification.....	64
IV.2.2.1.	$C_{pos}$ aging model parameters identification.....	65
IV.2.2.2.	$C_{neg}$ aging model parameters identification .....	68
IV.2.2.3.	OFS aging model parameters identification .....	71
IV.2.3.	Aging model validation.....	74
IV.3.	Evolution of the dual-tank model parameters with aging .....	76
IV.3.1.	Simulation of the calendar aging condition at T=45°C and SOC=65%: reference case.....	76
IV.3.1.1.	Aging evolution of the dual-tank OCV parameters and full cell capacity. ....	76
IV.3.1.2.	Evolution of the positive and negative electrode potential signals.....	77
IV.3.1.3.	Evolution of the maximum and minimum lithium content .....	78
IV.3.2.	Influence of the degradation rate on the electrode lithium contents .....	79
IV.3.2.1.	Acceleration of the positive electrode capacity $C_{pos}$ aging parameter .....	79
IV.3.2.2.	Acceleration of the electrode capacity $C_{neg}$ aging parameter .....	80

IV.3.2.3.	Acceleration of OFS aging.....	81
IV.3.3.	Influence of the electrodes sizing on the electrode potential signals and lithium content .....	82
IV.3.3.1.	Positive electrode undersized .....	82
IV.3.3.2.	Positive electrode oversized.....	83
Conclusion.....		85
CHAPTER 5: DUAL-TANK PHYSIC BASED AGING MODEL .....		87
Introduction .....		88
V.1.	SEI modeling .....	89
V.1.1.	Full cell representation .....	89
V.1.2.	SEI mechanisms and equations.....	90
V.1.2.1.	Kinetic of intercalation of the lithium-ion : .....	90
V.1.2.2.	SEI growth model and the parasitic reaction of lithium-ions consumption .....	91
V.2.	Physics-based aging model .....	94
V.2.1.	<i>OFS</i> aging law .....	94
V.2.2.	Influence of degradation modes on the offset aging.....	96
V.2.2.1.	Influence of <i>LLI</i> on the offset parameter .....	96
V.2.2.2.	Influence of the loss of active mass <i>LAM<sub>pos</sub></i> on the offset parameter .....	97
V.2.2.3.	Influence of the loss of active mass <i>LAM<sub>neg</sub></i> on the offset parameter.....	98
V.2.3.	Identification of the parameters of the physics-based aging model.....	99
V.2.3.1.	Identification method and results .....	100
V.2.3.2.	SEI thickness growth.....	103
V.2.4.	Aging evolution of the parameters of the physics-based aging model .....	104
V.2.4.1.	Evolution of the electrode potential signals with aging .....	104
V.2.4.2.	Evolution of the cell voltage and capacity with aging .....	106
V.2.5.	Validation of the physics-based aging model and comparison with the one-tank aging model.....	107
Conclusion:.....		109
GENERAL CONCLUSION AND PERSPECTIVES .....		110
VI.1.	General conclusion .....	110
VI.2.	Perspectives .....	111
VI.2.1.	Dual-tank OCV model: hysteresis effect and validation of the identification process .....	111
VI.2.2.	Dual-tank aging model: Effect of temperature and state-of-charge .....	111
VI.2.3.	Physics-based aging model: modeling of the active mass loss on the electrodes.....	112
VI.2.4.	Physics-based aging model: Introduction of other mechanisms for the SEI .....	112
REFERENCES .....		112

## GENERAL INTRODUCTION

Lithium-ion (Li-ion) batteries are widely used for applications in electric vehicles (EVs) and hybrid electric vehicles (HEVs) due to their high energy and power density [1]. The challenge for operators and managers of electric-vehicle fleets is to ensure the profitability of their vehicle rental business models. One of their levers is to promote the reliability of batteries by optimizing vehicle usage. Compromises must be determined between available autonomy, battery durability, and for the recharge: the frequency, the duration, and power level. For this, robust models representing the aging of batteries according to actual conditions of use are essential. Over the past years, several projects including the French national project MOBICUS [2] had been launched for the prognosis of Li-ion batteries aging. The main objectives of this project were to understand the coupling between calendar and cycling aging but also to design and validate strategies enabling to extend battery life according to real vehicle usage.

To increase the lifetime of Li-ion batteries, the prediction of the battery End-Of-Life (EOL) is an important task. The prognosis of internal states such as the State Of Health (SOH) and the estimation of the loss of performances due to aging are necessary to ensure reliable operating batteries. The SOH represents the ratio between the total cell capacity at a given aging state and the total capacity at the Beginning-Of-Life (BOL). The prediction of the SOH of the battery must be inferred from models depending on the usage and operating conditions such as temperature, State of Charge (SOC), or current flowing through the battery. The SOC traduces the level of charge of the battery and represents the ratio between the available cell capacity measured at a given C-rate and nominal capacity at a given aging state.

Some recent works propose semi-empirical and physics-based aging models to forecast the cell capacity change during battery aging. The Open-Circuit Voltage (OCV), which is the difference of potential between the positive and negative electrodes when no current flows, is related to the cell capacity. Indeed, these electrode potential signals are modified due to various parasitic mechanisms. Therefore, the understanding of the aging mechanisms of lithium-ion batteries plays an important role in the prediction of the OCV and cell capacity evolution along with aging. As the battery capacity decreases along with aging (SOH fading), the OCV-SOC signal is modified. The works proposed in the literature develop two sorts of OCV models to update the OCV-SOC signal along with aging: the one-tank OCV model and the dual-tank OCV one. The one-tank OCV model modifies the OCV-SOC signal knowing the battery SOH while the dual-tank OCV model considers the evolution of the electrode capacities and the offset between the electrode potential signals.

The research work, presented in this thesis, explores issues related to the evolutions of the electrode potential signals during aging and how they impact the prediction of the cell capacity through aging as well as the battery OCV. The aim is to develop new aging models considering the operating conditions of the battery to improve the prediction of the cell capacity. Based on calendar aging tests, a semi-empirical aging model will be proposed to predict the aging of electrode capacities and the evolution of the offset between electrode potential signals. Besides, a physics-based aging model, based on existing models in the literature, will be proposed to have a better understanding of the contributions of the aging mechanisms on the battery prognosis.

This thesis manuscript is divided into five chapters corresponding to the different lines of research developed during this work.

The first chapter presents the operating principles of the production lithium-ion battery used during this thesis work. This chapter focuses on the aging mechanisms and degradation modes reducing the performance of the battery. The state-of-art prognosis of battery capacity using aging models is depicted at the end of the first chapter.

The second chapter is devoted to the MOBICUS project and experimental setup. The specification of the cells used during the project and protocols of check-up used during the aging campaign are described. Also, the experimental results of the SOH evolution for various calendar conditions are detailed in the last section of the chapter.

The third chapter begins with the presentation of the MOBICUS aging model developed during the project by CEA team. Moreover, a new one-tank aging model also based on the cell capacity prognosis is developed in this thesis, with different aging factor expressions. In both cases, the two aging models are identified and validated using the experimental aging conditions detailed in chapter 2. Finally, the MOBICUS aging model and the new one-tank aging models are compared.

In the fourth chapter, a dual-tank OCV model is developed, and its parameters are identified for different aging states, i.e., the positive electrode capacity  $C_{pos}$ , the negative electrode capacity  $C_{neg}$  and the offset (*OFS*). This dual-tank OCV model is then coupled to three semi-empirical aging models aiming at predicting the evolution of these three parameters. This model has been evaluated, validated, and compared to the one-tank aging model.

In the fifth chapter, a physics-based aging model for the offset parameter (*OFS*) is proposed, focusing on the modeling of the SEI growth at graphite/SEI interface. The evolution of the SEI growth and lithium contents in the electrodes are studied through this physics-based aging model. Finally, the physics-based aging model and the one-tank aging model are compared for the prognosis of the cell SOH.

CHAPTER 1: STATE-OF-THE-ART AND OBJECTIVES OF THE STUDY

## Introduction

This first chapter addresses the state-of-the-art of aging mechanisms and prognosis models used in the literature to predict the evolution of the cell SOH and OCV.

The first part of this chapter presents the principle of operation of the lithium-ion cell and the battery technology used in the MOBICUS project [2] with its different compounds.

The second part proposes a bibliographic study on the main aging mechanisms, degradation modes, and types of aging studied in the framework of the thesis. These mechanisms are responsible for the degradation of the battery SOH and the evolution of the open-circuit voltage OCV shape.

The state-of-the-art aging models proposed in the literature for the prognosis of the battery SOH and OCV are presented in the third part of the chapter. Two types of models are described: the one-tank and the dual-tank aging models. These models are used to predict the evolution of the performances of the production cell depending on the operating conditions applied to the battery.

Finally, the objectives of this thesis are presented in the fourth part.

### 1.1. Lithium-ion battery presentation

Lithium-ion batteries are composed of a succession of cells in series and/or in parallel. A single cell contains two electrodes (negative and positive electrodes) separated by a separator; the whole system filled with electrolyte. Both electrodes are composed of an active material deposited on a current collector. Typical current collectors are made with copper for the negative electrode and aluminum for the positive electrode. The representation of a lithium-ion cell is illustrated in [FIGURE I-1](#).

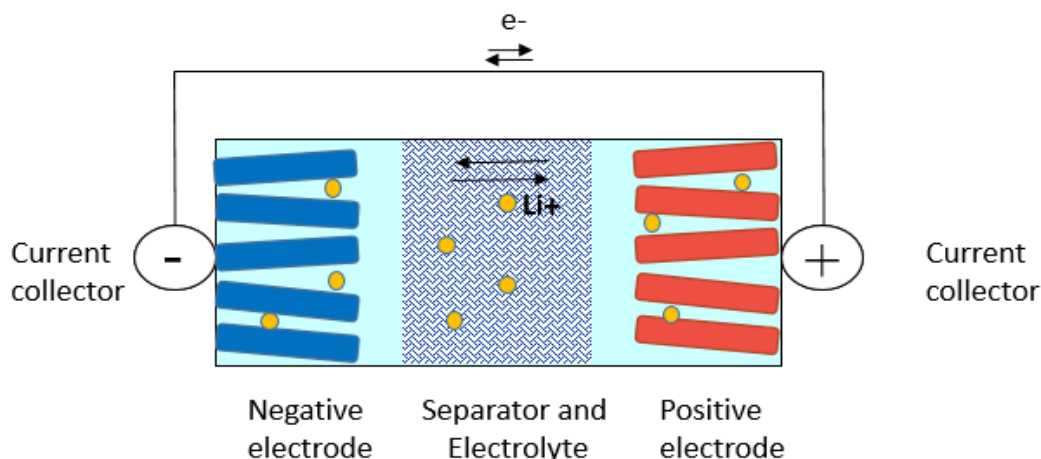


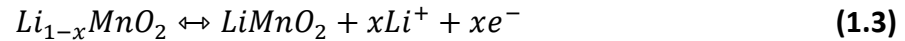
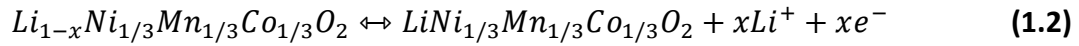
Figure I-1: Li-ion battery presentation.

For the scope of this thesis, the battery technology uses graphite for the negative electrode and a blend of lithium Nickel Manganese Cobalt Oxide and Lithium Manganese Oxide materials (NMC/LMO) for the positive electrode.

- Reactions at the graphite electrode:



- Reactions at the NMC-LMO electrode:



The electrolyte used in the Li-ion battery is composed of a mixture of solvents. This mixture comprises alkyl carbonates (Ethylene Carbonate (EC), Dimethyl Carbonate (DMC)). The salt, most used, is the lithium hexafluorophosphate ( $LiPF_6$ ). Some additives are combined to the mixture by 5 % either by weight or by volume of the battery, which significantly improves the cycle life of the Li-ion battery. These additives also reduce the irreversible capacity and enhance  $LiPF_6$  thermal stability against the organic electrolyte solvents.

The separator is an electrically insulating material, which prevents the electrons from flowing from one electrode to another.

## 1.2. Aging of Li-ion batteries

The study of aging mechanisms (see [FIGURE I-2](#)) on the electrodes is a key issue as aging depends on the type of materials used for the electrodes and the operating conditions. It has been reviewed by Vetter et al. [3] who evaluated the aging on carbonaceous negative electrode, lithium manganese oxides ( $LiMn_2O_4$ ) with spinel structure and lithium nickel cobalt mixed oxides [ $Li(Ni, Co)O_2$ ] with layered structures. All those aging mechanisms lead to the loss of battery performance in terms of capacity decay. The stress factors (temperature, current, state-of-charge) applied to the battery highly impact the battery loss of performance [4].

### 1.2.1. Aging mechanisms on the negative and positive electrode

One of the most documented phenomena in the literature is the growth of a passivation layer called SEI [5]–[8] (Solid Electrolyte Interphase) as shown in [FIGURE I-2](#). The SEI is formed during the first charge cycle of the battery. Its formation leads to an irreversible loss of capacity within the cell. The SEI layer formed during the first charge reduces the SEI growth by slowing down the diffusion of the molecules of solvents towards the interface between graphite and SEI. Also, the SEI layer protects the graphite from the intercalation of the molecules of solvents in the layers of the negative electrode that may cause its deformation (graphite exfoliation).

On the positive electrode, a passivation layer may also appear due to the decomposition of the electrolyte on the positive electrode/electrolyte surface [9].

Another mechanism often mentioned in the literature is lithium plating [10], which corresponds to the deposition of Li-ions on the surface of the negative electrode. Part of the plated lithium will be consumed irreversibly due to either the reaction with electrolyte to form new SEI film or the formation of “dead” lithium which is electrically isolated with anode [11]. The rest of plated lithium is considered as a reversible part. The reversible part of plated

lithium can re-intercalate in the negative electrode known as “lithium stripping”. Finally, this accumulation of lithium can promote the formation of dendrites [12] and thereby cause a short circuit between the two electrodes leading to a possible thermal runaway of the battery.

Another type of aging mechanism on the electrodes is the deactivation of the material particles, which are electrically insulated from the current collectors. On the negative electrode, the graphite exfoliation due to the solvent intercalation, the material delamination as well as the particle cracking due to the intercalation/extraction of the lithium are considered as a cause of graphite particle deactivation. On the positive electrode, the particles cracking, and active material dissolutions are also considered as deactivation of the active material.

Some studies in the literature evoke the influence of the positive electrode on the negative electrode during cycling, in particular the positive electrode materials based on Manganese ( $Mn_{2+}$  ions) which can contaminate the negative electrode [13] or be found in the SEI [14]. The main hypothesis evoked in the literature is that these  $Mn_{2+}$  ions can diffuse into the SEI layer and destabilize it. This can possibly create cracks in this layer during cycling and increase the SEI formation. Another hypothesis different from the latter is proposed by Wang et al. [15] which associated the destabilization of the SEI layer due to acid impurities (HF) as the only cause of capacity fade. However, this hypothesis has been contradicted by Charles Delacourt et al. [16] who demonstrated that delamination of the LMO material is also a cause of capacity loss as it produces  $Mn_{2+}$  ions which are trapped on the SEI layer. The capacity loss is even higher when the  $Mn_{2+}$  are trapped in the SEI layer compared to when they simply diffuse into the SEI layer and intercalate in the graphite electrode because they provoke more structural change of the SEI.

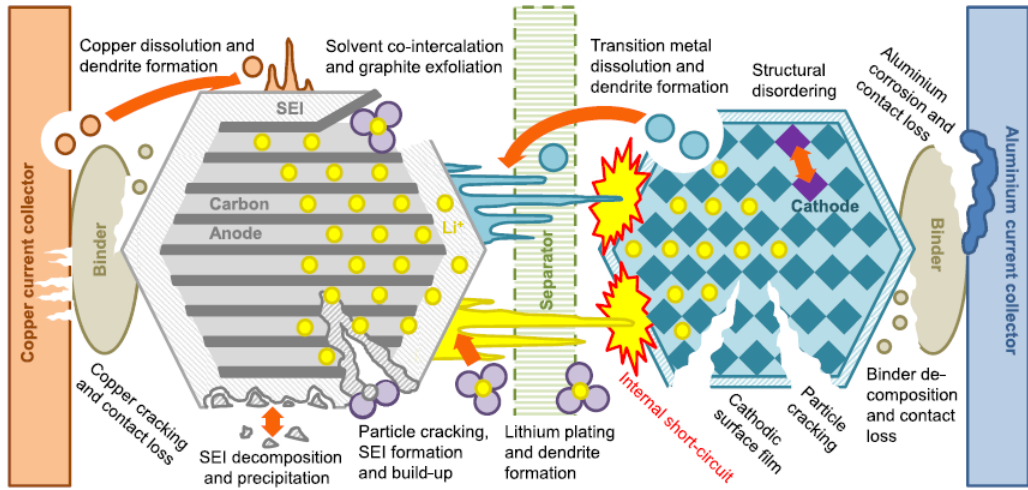


Figure I- 2 : Aging mechanism on the negative and positive electrodes [3].

### 1.2.2. Degradation modes on the electrodes

The degradation modes are the direct consequence of the degradation mechanisms. From what we mentioned previously, they can be categorized into two groups: Loss of Lithium Inventory (LLI) and Loss of Active Material (LAM).

The definition of loss of lithium inventory diverges in the literature. It can account for either the loss of Li ions only due to the parasitic reaction of SEI formation ([8], [17]) or the total Li loss included the Li trapped in the active material ([18], [19]). The loss of active mass occurs when Li can no longer be inserted in (or extracted from) active material due to the electrode deterioration.

Some factors such as current, temperature, and state of charge can accentuate the physical and chemical interactions within the battery. The degradation modes listed in the literature are summed up in **FIGURE I-3** [19].

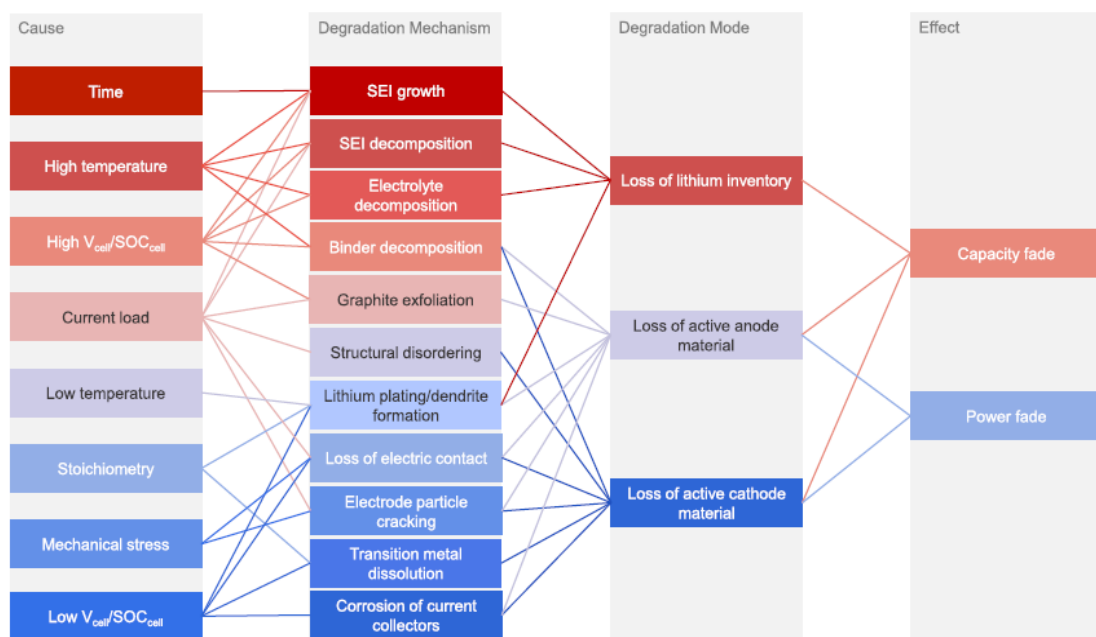


**Figure I-3: CAUSES AND EFFECTS OF DEGRADATION MECHANISMS AND ASSOCIATED DEGRADATION MODES [19]**

### 1.2.3. Aging modes

There are generally two modes of aging for Li-ion batteries, calendar and cycling aging:

- Calendar aging represents the capacity loss of the battery during storage. There are generally two types of capacity losses: reversible capacity losses and irreversible losses. Reversible capacity losses correspond to the self-discharge of the battery. The quantity of Ah that failed to be fully charged is called the irreversible part [4]. The temperature and state of charge stress factors are important during calendar aging. Li-ion cells generally undergo higher aging at high temperatures and states of charge, but often the effect of temperature is predominant.
- Aging during cycling is synonymous with deterioration of battery performance following a charge/discharge sequence. It depends on the temperature, current, and depth of discharge profiles applied to the cell.

#### 1.2.4. OCV measurements at different aging states

The SOH is defined by:

$$SOH(\%) = \frac{Q_{nominal}(t)}{Q_{nominal}(t=0)} * 100 \quad (1.4)$$

$Q_{nominal}(t)$  being the current total capacity and  $Q_{nominal}(t=0)$  the total capacity measured at the Beginning-Of-Life (BOL), expressed in Ah.

The SOC is calculated as the ratio between remaining capacity  $Q_{remaining}(t)$  and the nominal one  $Q_{nominal}(t)$  as follows:

$$SOC(\%) = \frac{Q_{remaining}(t)}{Q_{nominal}(t)} * 100 \quad (1.5)$$

The OCV, at a given battery SOH, is commonly characterized versus the SOC.

Experimentally, the OCV-SOC signal is measured using two methods:

The first method is the Galvanostatic Intermittent Titration Technique (GITT). This is the most common method used. This method is performed by successive charge (or discharge) the battery at different SOC's followed by a resting time. This resting time allows the battery to reach the equilibrium state. The OCV is then measured at that equilibrium state. Following this step, we can deduce the OCV-SOC curve.

The second method is the continuous OCV measurement at a low rate ( $\leq C/10$ ). Initially, the battery is fully discharged (or charged). Then a constant current  $I$  is applied until the battery reaches the SOC 100% (or 0%). The same current is applied to completely discharge the battery to reach 0% of SOC (or completely charge to reach the SOC 100%). The main advantage of this method is that it required less time than the GITT method. Between the two phases (complete charge and discharge), a resting time is applied to stabilize the cell voltage as shown **FIGURE I-4** [20]. In fact, the OCV signal in **FIGURE I-5** is considered as a pseudo-OCV. Even at low current, the battery is still influenced by the polarization effect.

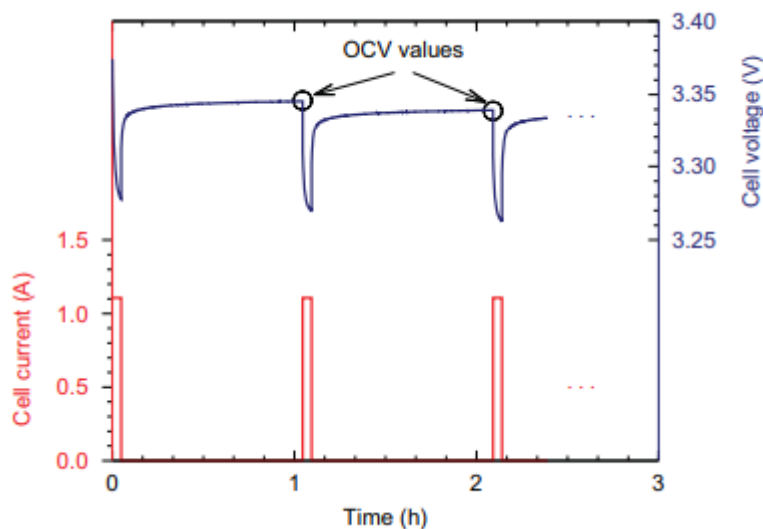
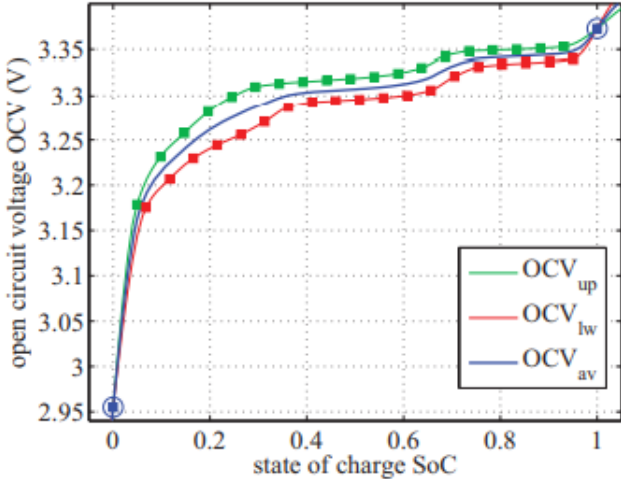


Figure I-4: Measurement of a galvanostatic charge signal [20]

So, to build the real cell OCV ( $OCV_{av}$ ), the pseudo-OCV charge signal ( $OCV_{up}$ ) and discharge signal ( $OCV_{lw}$ ) are averaged as illustrated in **FIGURE I-5**.



**Figure I- 5: OCV AND CHARGE/DISCHARGE PSEUDO-OCV [20]**

The OCV-SOC change is dependent upon the operating conditions and aging stages and must be experimentally characterized depending on the cell SOH [21]. An example is given in **FIGURE I-6** where the OCV has been characterized at different SOH for the cell battery. The data come from an internal project conducted at the French Atomic Energy and Alternative Energies Commission (CEA).

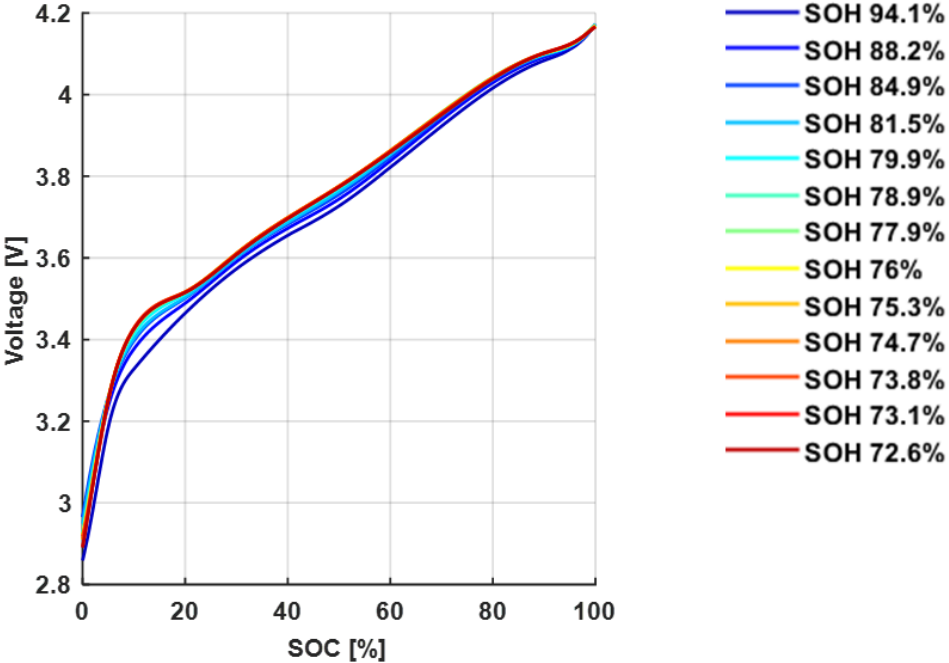


**FIGURE I- 6: PSEUDO-OCV CURVE VERSUS SOC AT DIFFERENT SOH [CEA INTERNAL PROJECT].**

### 1.3. Prognosis of lithium-ion batteries SOH and OCV

The prognosis of the battery SOH and OCV can be performed using data-driven methods. These data-driven methods correspond to prognosis models such as aging models [22] or machine learning methods [23]. In this thesis work, we will only focus on aging models for the prognosis of the battery SOH and OCV. Two types of models are studied in this section: the one-tank and the dual-tank aging models.

#### 1.3.1. One-tank OCV and aging models

The one-tank aging models developed in the literature predict the evolution of the cell SOH (or capacity), which is used to update the OCV versus SOC signal during aging, as illustrated in

FIGURE I- 7.

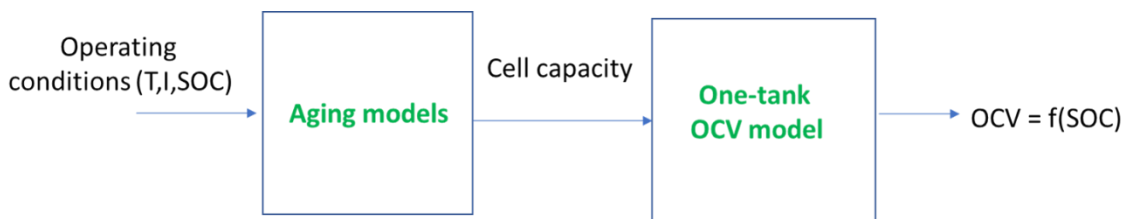


FIGURE I- 7: PROGNOSIS OF THE CELL PERFORMANCES WITH THE ONE-TANK AGING MODEL

#### 1.3.1.1. One-tank OCV model

In the literature, the OCV-SOC signal along with aging is updated using three approaches. In the first approach, the OCV-SOC (or OCV-Q) signal is measured at the BOL. Then the OCV curve is transversely shrunk knowing the cell SOH. Wang et al. [24] studied the characteristic of OCV-Q for LiFePO<sub>4</sub> by transversely shrinking the OCV curve when the battery loses a certain amount of capacity, as shown in FIGURE I- 8. This shrinking is equivalent to multiply the remaining Q abscissa by a constant ratio (SOH). As a result, the shape of the OCV curve is kept constant but it is simply shifted to the left during aging.

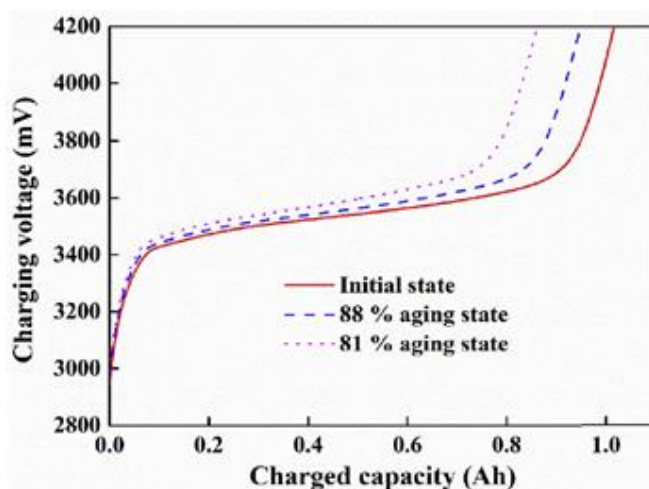


FIGURE I- 8: V-Q curve with different aging state [24]

In fact, the shape of the OCV curve can also be distorted with aging as illustrated in [FIGURE I-6](#). The second and third methods used in the literature to update the OCV are model-based approaches:

- The second approach used for the correction of the OCV signal consists of using a look-up table OCV function of SOC and SOH and performing a linear interpolation at a given SOH to determine the OCV-SOC signal [25].
- The third approach is based on the mathematical functions of OCV versus SOC. Yu et al. [26] reviewed a total of eighteens OCV-SOC functions models in the literature. Those mathematical models include polynomial, exponential, and logarithmic functions. The OCV-SOC signal along with aging is updated by performing an optimization process[27].

### 1.3.1.2. One-tank capacity aging model

The prediction of the battery SOH is done using either semi-empirical or physics-based aging models.

#### 1.3.1.2.1. Semi-Empirical approaches

In the literature, semi-empirical aging models assess the capacity loss variation  $\frac{\partial Q_{loss}}{\partial t}$  as follows [28]:

$$\frac{\partial Q_{loss}}{\partial t} = \varphi(Q_{loss}, stress\ factors) \quad (1.6)$$

Where  $\varphi$  is a mathematical function linking the stress factors (current, temperature, state-of-charge) with the capacity loss  $Q_{loss}$ .

For respecting the principle of cumulative damage as reported by M. T. Todinov et al.[29], the capacity loss variation  $\frac{\partial Q_{loss}}{\partial t}$  must be defined by:

$$\frac{\partial Q_{loss}}{\partial t} = \varphi_a(stress\ factors) * \varphi_b(Q_{loss}) \quad (1.7)$$

Where  $\varphi_a$  represents the accelerating factors of the degradation while  $\varphi_b$  is a function depending on the capacity loss  $Q_{loss}$ .

#### 1.3.1.2.1.1. Accelerating factors

The accelerating factors are used to describe the influence of the operating conditions applied to the battery along with aging. In calendar aging, the accelerating factors depend on the temperature  $T$  and state-of-charge  $SOC$ . In cycling aging, the contributions of the charge current  $I_{cha}$ , the discharge current  $I_{dch}$  are added while the SOC is replaced by the average state-of-charge  $SOC_{av}$  (cycling being carried out around  $SOC_{av}$ ) and the depth of discharge  $DoD$ .

Bagdhdadi et al.[28] highlighted the fact that the choice of the adequate accelerating factor for the aging model is highly dependent on the experimental set-up. They studied the calendar aging of production li-ion batteries in the SIMCAL project [30] and cycling aging for two technologies (SAFT, LG) in the SIMSTOCK project [31]. The aging was carried out for different  $DoD$ ,  $T$ ,  $I$ , and  $SOC$ . A list of equations proposed in the literature to define accelerating factors can be found in [TABLE I-1](#):

Stress factors	Accelerating factor	References
Temperature	$\varphi_T = a \exp\left(\frac{-E_a}{RT}\right)$	Grolleau[32], Wang[33], bloom[29]
	$\varphi_T = a + bT + cT^2$	Hoog[35]
Voltage	$\varphi_V = a * V^n$	Makdessi[36]
	$\varphi_V = a + bV + cV^2$	Schmalstieg[37], Marongiu [38]
SOC	$\varphi_{SOC} = \exp(a * SOC)$	Baghdadi [28]
	$\varphi_{SOC} = a + bSOC + cSOC^2$	Hoog[35], Petit [22]
Current	$\varphi_I = a * \exp\left(\frac{b(I)I}{RT}\right)$	Petit [22]
	$\varphi_I = a * \exp(b(T) * I)$	Baghdadi [28]
DoD	$\varphi_{DoD} = a \exp(b * DoD) + c \exp(d * DoD)$	E. Sarasketa-Zabala[8]
	$\varphi_{DoD} = a + bDoD + cDoD^2$	
Temperature & SOC	$\varphi_{T,SOC} = A(SOC) \exp\left(\frac{-E_a(SOC)}{RT}\right)$	E.Rodondo[74]

TABLE I- 1: A LIST OF STRESS FACTORS IN SEMI-EMPIRICAL AGING MODELS

From TABLE I- 1, we can understand that many accelerating factors are proposed in the literature to establish a semi-empirical aging model. In their model, Wang et al. [39] only considered the effect of the temperature in calendar aging using an Arrhenius law, however, the SOC and other parameters may also have an influence on the battery aging. This influence is highlighted by E.Redondo et al. [74] who generalized an Arrhenius law to other factors than temperature to tackle down this issue.

As pointed out by Baghdadi et al. [28], the accelerating factors mentioned in TABLE I- 1 can be mathematically associated in various ways that diverge in the literature. Usually, each accelerating contribution can be separately added to the total degradation rate in Eq. (1.6) by multiplying them, as shown in TABLE I- 2

Aging mode	Accelerating factors association	References
Calendar	$\varphi_T * \varphi_{SOC}$	Petit [22], Hoog[35]
Cycling	$\varphi_T * \varphi_{SOC} * \varphi_I$	Baghdadi [28]

TABLE I- 2: stress factors association

#### 1.3.1.2.1.2. Degradation function

Various semi-empirical models are proposed in the literature and deduced from experimental data obtained at constant stress factors. Grolleau et al. [32] highlighted the fact that in EV application, the stress factors are usually variable over time. Grolleau et al. [32] proposed a semi-empirical aging model under non-constant stress application:

$$\frac{\partial Q_{oss}}{\partial t} = k(T, SOC) \left(1 + \frac{Q_{loss}}{C_{nom}}\right)^{-\alpha(T)} \quad (1.8)$$

With the cell capacity Q defined by:

$$Q(t) = C_{nom} - Q_{loss}(t) \quad (1.9)$$

$k(T, SOC)$  being the accelerating factor for T and SOC,  $C_{nom}$  the nominal capacity of the cell. The accelerating factor  $k(T, SOC)$  follows a linear dependence with SOC:

$$k(T, SOC) = A(T).SOC + B(T) \quad (1.10)$$

While the degradation loss function in Eq. (1.8) is expressed by:

$$\varphi_b(Q_{loss}) = \left(1 + \frac{Q_{loss}}{C_{nom}}\right)^{-\alpha(T)} \quad (1.11)$$

The individual temperature factors A(T) and B(T) are expressed with an Arrhenius law which is commonly used in the literature to describe the impact of temperature on cell aging unlike the polynomial law proposed by Hoog et al. [35]. This equation established by Grolleau et al. [32] is similar to the empirical aging model proposed by Broussely et al.[40].

1.3.1.2.2. *Physics-based approach*  
 1.3.1.2.2.1. *SEI representation*

There are generally two types of representation for the SEI layer [41]. The first category considers that the SEI is composed of two layers: a compact layer and a porous one. The electrons and lithium ions can tunnel through the compact layer and react with the solvent at the interface between compact/porous layers leading to the continuous growth of the SEI [42], [43]. This first assumption is schematically illustrated in Figure I- 9 for a graphite/LFP cell.

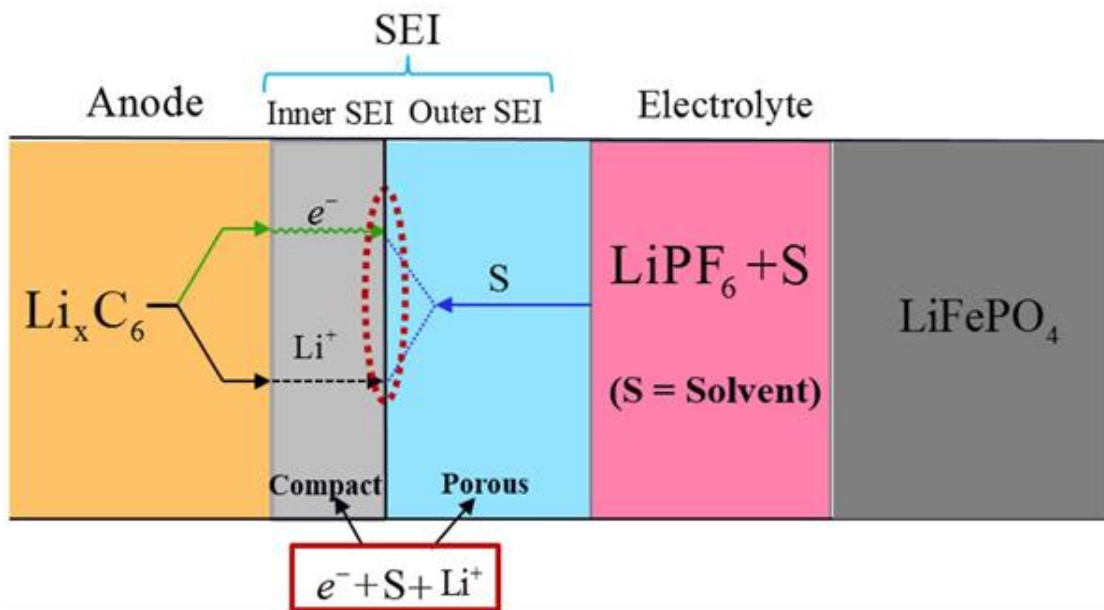


Figure I- 9: SCHEMATIC REPRESENTATION OF A C6/LiFePO4 BATTERY, SHOWING THE FORMATION OF THE INNER- AND OUTER SEI LAYER [44]

For the second assumption, the SEI is assumed to be a single porous layer that is not admissible to the electrons. The SEI formation is due to the solvent diffusion through the porous to be reduced at the interface between the negative electrode surface and SEI [45], [46].

1.3.1.2.2.2. *SEI modeling*

Concerning the SEI modeling, some studies consider the SEI formation to be controlled by either the kinetic of solvent reduction at the graphite/SEI interface [47] or diffusion transport of the solvent through the SEI [48]. Few studies develop a mixed-growth model taking into account simultaneously kinetic and diffusion control[49]. In these models, the equations

trading the kinetic of the solvent reduction at the interface graphite/SEI diverge in the literature.

Safari et al. [50] proposed a mixed growth model to conclude that the SEI formation is more under diffusion control because the kinetic limited model simulation is far from experimental data. The current density for side reactions is defined by a Tafel-like equation:

$$i_s = -Fk_{f,s}c_{EC} \exp \left[ -\frac{\beta_s F}{RT} (\phi_1(SOC) - R_{SEI}i_t) \right] \quad (1.12)$$

$F(C \text{ mol}^{-1})$  being the Faraday constant,  $k_{f,s}$  (m/s) the rate constant of side reactions,  $c_{EC}(\text{mol. m}^{-3})$  the concentration of solvent in the SEI film,  $\beta_s$  the cathodic charge-transfer coefficient for the side reaction,  $R(J \text{ mol}^{-1}K)$  the gas constant,  $T(K)$  the temperature,  $\phi_1(V)$  the potential of the graphite,  $R_{SEI}(\Omega \text{ m}^2)$  the SEI film resistance referred to the interfacial surface area of anode and  $i_t(A \text{ m}^2)$  the total current density referred to the interfacial surface area of the anode. The pre-exponential factor ( $-Fk_{f,s}c_{EC}$ ) represents the exchange current density.

Later, Delacourt et al. [51] proposed an alternative expression for the kinetic reduction of the solvent from safari et al. model [50]. The particularity of Delacourt et al. model [51] is that it addressed the SEI growth phenomena on the negative electrode and a mechanism to account for possible growth of a passivation layer on the positive electrode. The current density for side reactions on the negative electrode was defined similarly by:

$$i_s = -Fk_{f,s}c_{EC} \exp \left[ -\frac{\beta_s F}{RT} (\phi_1(SOC)) \right] \quad (1.13)$$

The SEI film resistance is not considered by Delacourt et al. [51].

Pinson et al.[52] developed a mixed growth model, which takes into account the local potential close to the interface between SEI/electrolyte and the equilibrium potential of the SEI. However, the induced SEI overpotential  $\eta_{SEI}$  does not depend on the SOC [52]:

$$i_s = 2 i_0 \sinh \left( \frac{e \eta_{SEI}}{2 k_B T} \right) \quad (1.14)$$

$i_0(A \text{ m}^{-2})$  being the exchange current density and depends on the solvent concentration,  $\eta_{SEI}$  is the overpotential driving the SEI formation and  $k_B$  the Boltzmann constant. The overpotential  $\eta_{SEI}$  is expressed by:

$$\eta_{SEI} = \phi_1 - \phi_{electrolyte} - R_{SEI}i_t - \Delta\phi_{SEI} \quad (1.15)$$

$\phi_{electrolyte}$  being the local potential close to the interface between SEI/electrolyte and  $\Delta\phi_{SEI}$  the equilibrium potential of the SEI.

In literature, some parameters are omitted in the kinetic equation (1.13) such as the influence of SOC. In addition, different pre-exponential factors are expressed depending or not on the lithium and solvent concentrations ([6], [50], [52]). Finally, different values of equilibrium

potential for the SEI are proposed in literature varying from 0.4 to 0.8V ([53], [54]) when it is not omitted by the authors [55].

For the prognosis of the Li-ion batteries SOH, the physics-based aging models developed in the literature related to the SEI often link the capacity drop of the production cells to the consumption of Li-ions due to the SEI growth. For instance, Ekström et al. [56] developed a prognosis model for the cell capacity  $C_{batt}$  based on the capacity loss  $Q_{sei}$  due to SEI layer growth on the negative electrode as follows:

$$C_{batt}(t) = \frac{C_{batt}(t = 0) - Q_{sei}(t)}{C_{batt}(t = 0)} \quad (1.16)$$

$C_{batt}(t = 0)$  being the nominal cell capacity at Beginning-Of-Life (BOL).

The degradation rate of the capacity loss due to the SEI is expressed by:

$$\frac{dQ_{sei}}{dt} = -I_{sei} \quad (1.17)$$

$I_{sei}$  (A) being the current of the parasitic SEI forming reactions. An aging model for  $I_{sei}$  is developed by Ekström et al. [56].

### 1.3.1.3. One-tank aging models limitation

Semi-empirical and physics-based aging models are widely used in the literature for the prognosis of the Li-ion batteries SOH and OCV. However, production lithium-ion batteries are subjected to complex degradation mechanisms that lead to loss of lithium inventory and active mass losses on both electrodes. These degradation modes can affect differently the electrode potential signals and therefore modify the OCV signal in many possible ways. Using the single value of SOH associated with a one-tank OCV model to update the OCV during aging does not allow to consider many degradation paths of the battery and is not enough to define properly the aged cell OCV.

### 1.3.2. Dual-tank OCV and aging models

Dual-tank OCV models consist of battery models allowing to determine the cell OCV and capacity. They are developed in the literature to consider the degradation paths of the production batteries for a better accurate modification of the OCV along with aging and prediction of the cell capacity.

#### 1.3.2.1. Dual-tank OCV model

Dual-tank OCV models are defined using the electrode potential signals of the cell battery. In the literature, some authors also consider the cell resistance (due to polarization effect) as an additional parameter of the dual-tank OCV model, but some authors do not.

Dubarry et al.[57] was the first to introduce this kind of model which can simulate various scenarios of degradation modes leading to different ways of voltage fading, as shown in [FIGURE 1-10](#). Five terms of degradation modes were identified to describe the cell SOH: Loss of lithium inventory (LLI), loss of lithiated active mass on the negative electrode, loss of delithiated active

mass on the negative electrode, loss of lithiated active mass on the positive electrode and loss of delithiated active mass on the positive electrode. The authors made a hypothesis whether the loss of active mass on the electrodes occurs at a fully lithiated or delithiated state. The loss of active mass can occur at any state of lithiation. The authors added the cell resistance as an additional input parameter of the dual-tank OCV model to define the cell voltage aging.

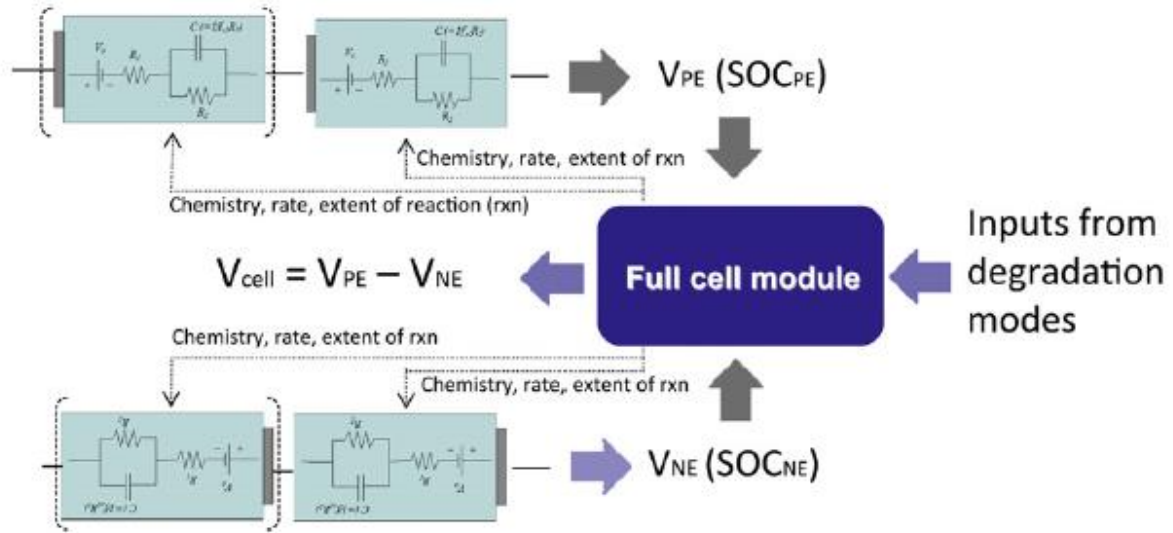


FIGURE I- 10: SCHEMATIC OF THE MODELING APPROACH OF DUBARRY ET AL.[57]

Conversely to Dubarry et al. [57], Zeyu Ma et al.[58] built a dual-tank OCV model where the cell SOH is defined by the internal resistance as well as both electrodes capacities ( $Q_{PE}$ ,  $Q_{NE}$ ) and the initial SOC (SOC at the cell end-of-discharge) for both electrodes ( $SOC_{PE0}$ ,  $SOC_{NE0}$ ) as shown in FIGURE I- 11.

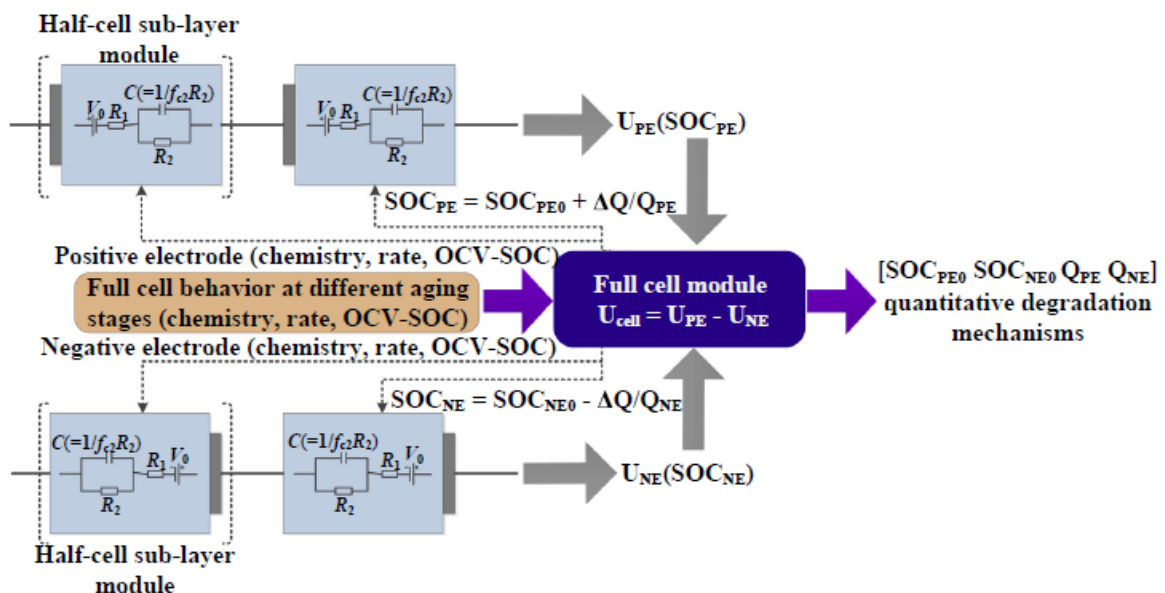


FIGURE I- 11: ZEYU MA ET AL. DUAL TANK MODEL [33]

Han et al. [59]) developed the same model as Zeyu Ma et al. [58]. However, the authors linked the initial SOC of the electrodes ( $SOC_{PE0}, SOC_{NE0}$ ) with a variable called offset (OFS) which represents the decay between electrode potential signals:

$$OFS = (Q_{pe}SOC_{PE0} - Q_{ne}SOC_{NE0}) \quad (1.18)$$

Some authors developed dual-tank OCV models neglecting the cell resistance as the OCV is measured at low current either in charge or discharge mode. Schindler et al. [60] used voltage measurements at very low current ( $C/20$ ) and they only considered the charge signals. Feng et al.[61] also performed galvanostatic voltage measurements but only in discharge mode. These authors did not consider a possible overpotential (voltage drop) that might occur due to the hysteresis effect [62]. This overpotential was introduced in a pseudo-OCV model by Lu et al. [63] during the discharge signal.

Finally, some authors developed a dual-tank OCV model without an overpotential parameter and where the OCV was experimentally measured by GITT tests or by averaging the charge/discharge signals. Marongiu et al.[64] proposed a methodology to track offline the actual capacity of a battery used in a vehicle collecting online data from a BMS. Their method was based on a plateau detection of the OCV curve which is changing during aging due to degradation mechanisms [64].

In their paper, Birkl et al.[19] also developed a dual-tank OCV model by performing GITT tests for the OCV measurements. They were able to diagnose some degradation mechanisms induced to form the cell capacity fade on production Kokam 740 mAh pouch cells. They were the first to perform experiments on Li-ion cells to prove evidence of possible degradation mechanisms depicted by Dubarry et al. [57]. Recently Mergo Mbeya et al. [65] showed that using both pseudo-OCV signals in charge and discharge at  $C/50$  and averaging them is a good strategy while using a dual-tank OCV model. The authors highlighted that contribution of the overpotential signals in charge and discharge can be neglected compared to the average of pseudo-OCV signals.

#### 1.3.2.2. Dual-tank aging model

The prognosis of the battery SOH using a dual-tank aging model is poorly addressed in the literature. Two ways of predicted the cell capacity have been listed in the literature:

##### 1.3.2.2.1. Direct prognosis of the cell capacity

Some authors assumed that the parameters of the dual-tank OCV model,  $LLI$  or  $LAM$  for instance, follow a certain aging law in calendar aging as illustrated in [Figure 1- 12](#). The OCV is built up using the electrode potential signals ( $V_{pos}, V_{neg}$ ) and the parameters  $LLI / LAM$ . In this approach (53), [63]), the authors do not consider the influence of the operating conditions on the battery SOH fading. Dubarry et al. [57] assumed that the loss of lithium inventory ( $LLI$ ) and loss of active mass ( $LAM$ ) follow respectively a linear and an exponential trend function of the cell resting time. However, those trends are only based on assumptions. Unfortunately, they did not consider the influence of operating conditions during calendar aging on the degradation of the cell capacity. The prognosis of the evolution of the battery SOH using a dual-tank OCV model was also performed by T.Lu et al [63] during calendar aging. However,

the authors did not build an empirical aging model depending on the operating conditions. The authors assumed that their aging models for LLI and LAM were directly a function of time without any law depending on the temperature or state-of-charge.

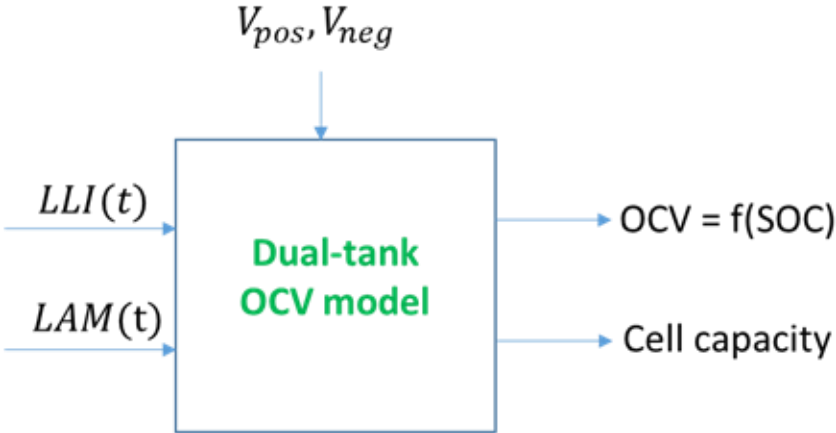


Figure I- 12: Prognosis of the cell capacity without considering the operating conditions.

1.3.2.2.2. Indirect prognosis of the cell capacity

A more elaborate way of predicting the cell capacity consists in developing a semi-empirical law for each parameter of the dual-tank OCV model depending on the operating conditions. Then, the cell capacity is simulated using the dual-tank OCV model as illustrated in Figure I- 13.

In his thesis, Jens groot [66], built a similar semi-empirical aging model but only for the negative electrode capacity. The authors consider the effect of the temperature, state-of-charge and current to link the anode to the cell degradation:

$$C = C_{BOL} (1 - k_{loss}(T, I, SOC))^{CT} \tag{1.19}$$

Where  $C$  is anode capacity,  $C_{BOL}$  the anode capacity at BOL,  $k_{loss}$  a loss function depending on the current, temperature, and state-of-charge and  $CT$  the capacity throughput. However, in his work, Jens Groot did not build an empirical model for each parameter of the dual-tank OCV model to predict the cell capacity aging.

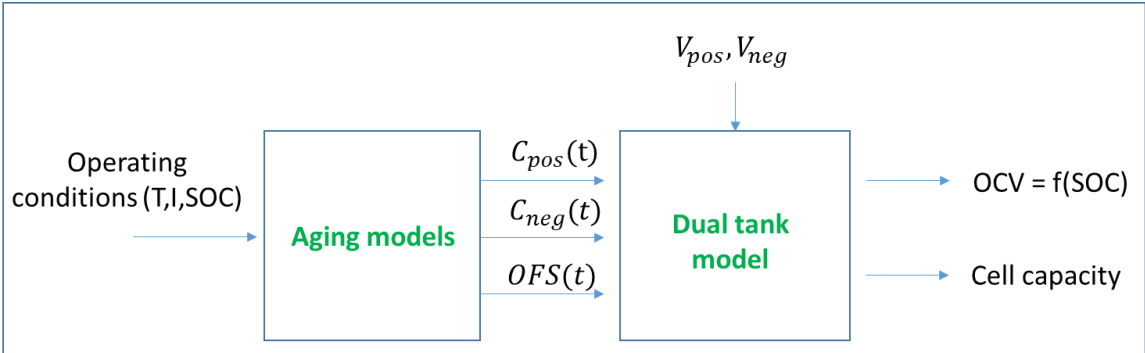


Figure I- 13: PROGNOSIS OF THE CELL CAPACITY TAKING INTO ACCOUNT THE OPERATING CONDITIONS

## I.4. Purpose of this thesis

Several points can be highlighted from the literature review:

- Semi-empirical aging models predicting the cell SOH are useful tools to predict the cell OCV aging. However, these latter do not consider the degradation path of the battery. In other words, these models omit the aging contributions of both electrodes separately and other physical phenomena (e.g., SEI growth) which can modify the OCV shape signals in various ways. A single semi-empirical aging model giving the value of cell SOH is therefore not enough to correctly update the cell OCV.
- The development of a dual-tank OCV model is relevant as it allows to define the cell SOH with more parameters and to consider the degradation path of the battery. Predicting the evolution of the parameters of the dual-tank OCV model along with aging also seems more reliable to predict the SOH and modification of the OCV signal. However, the semi-empirical aging models used in the literature are based on assumptions of LLI/LAM evolution. Indeed, they do not consider the influence of the operating conditions to predict the cell SOH, or do not predict the evolution of all parameters of the dual-tank OCV model along with aging.
- Physics-based aging models are mainly developed in the literature for SEI formation and growth, and for the associated lithium consumption. These models could be appropriate to study the influence of the degradation mode depicted in the literature for the prognosis of the cell capacity. The degradation mechanisms of the Li-ion batteries play an important role in the SOH prognosis. Dual-tank aging models developed in the literature lack physics-based assets to account for some phenomena such as the SEI formation. Using a physics-based aging model coupled to a dual-tank OCV model may be a reliable method.

From the literature review mentioned in the previous sections, we have noticed that combining aging models and OCV models is crucial to have a proper prediction of the battery capacity and OCV.

During this thesis, a dual-tank OCV model is used to study OCV aging. This model is then coupled to three semi-empirical aging models for each parameter of the dual-tank model: the positive electrode capacity  $C_{pos}$ , the negative electrode capacity  $C_{neg}$  and the offset (*OFS*). A new solution to predict the evolution of the battery SOH over time is presented while considering the operating conditions applied to the Li-ion cell. In addition, a physics-based aging model is used to analyze the SEI growth and the evolution of the lithium contents in the electrodes during aging.

## CHAPTER 2: MOBICUS PROJECT PRESENTATION AND EXPERIMENTAL AGING RESULTS

## INTRODUCTION

The development of electric vehicles (EVs) encourages the use of lithium-ion batteries due to the many advantages they offer (high specific energy, high voltage, low maintenance) [67]. Nevertheless, they are very sensitive to the usage (a charge, distance traveled...) and environmental conditions (temperature...) affecting their performances over time. Therefore, there is a need to develop aging models during real usage of a vehicle to promote the expansion of the battery lifespan. In the literature, some projects studied the aging prognosis of Li-ion batteries during calendar (SIMCAL project [30]) or cycling aging (SIMSTOCK project [68]). The main objective of the SIMSTOCK project focused on the coupling between calendar and cycling aging during usage. For this reason, the experience plan was divided into three parts: calendar, cycling, and a mixed one. Major parts of partners from SIMCAL and SIMSTOCK projects were mobilized in the MOBICUS project [2]. The experimental results on calendar aging are presented in the following sections and will be later used for the development of the aging models described in chapters 3, 4, and 5.

### II.1. MOBICUS PROJECT

#### II.1.1. Presentation and aims of the project

The MOBICUS project is a French national project that involves in total 16 partners combining five industrial companies (RENAULT, VALEO, EDF, SIEMENS, and ENEDIS), five research laboratories (CEA, IFPEN, IFFSTAR, IMS and EIGSI), two SMEs (CONTROLSYS and DBT-CEV) and four invited partners (LA POSTE, PSA, SAFT and UTC). This collaboration allowed to perform many aging tests split between each partner. The main objectives of the project are to [69]:

- Perform a huge test campaign in calendar and cycling aging for two technologies of battery.
- Develop an empirical aging model to understand the coupling between calendar and cycling aging.
- Design and validate strategies enabling to extend battery life according to real vehicle usage.

#### II.1.2. Production Gr/NMC-LMO cell and coin cells manufacture

##### II.1.2.1. Production cell characteristics

Two technologies of batteries were tested in the project. A 43Ah pouch cell (Graphite/NMC-LMO) used in the Renault Twizy (see [FIGURE II-1](#)) for EV application and 26Ah prismatic cell (Gr/NMC-Ni rich) for Plug-in Hybrid EV application [70]. The pouch cell voltage thresholds are 3V-4.2V. The configuration of the module (association of three pouch cells) is 3P2S. For the scope of this thesis, we will only recap the experimentation performed on the 43Ah pouch cell battery in this chapter captured in [FIGURE II-1](#):



FIGURE II- 1: RENAULT TWIZY VEHICLE AND 43AH POUCH CELL.

All the technical information is summed up in TABLE II- 1 below:

Characteristics at 25 °C		
Nominal capacity	Ah	43
Format		Pouch
Electrochemistry		NMC-LMO
End of discharge voltage	V	3.00
End of charge voltage	V	4.20
End of charge current under floating voltage	A	2.2 (~C/20)

TABLE II- 1: POUCH CELL TECHNICAL SPECIFICATION SHEET

#### II.1.2.2. Coin cells manufacture

To build a dual-tank OCV model, electrochemical tests to characterize the positive and negative electrode potential signals need to be performed. The pouch cell used during the MOBICUS project was disassembled at beginning-of-life during an internal project involving the CEA. The anode and cathode active materials harvested from the disassembled full cell were used to build coin cells with an active material surface of  $1.53 \text{ cm}^2$ . A cellgard 2400 propylene membrane was used as a separator; the counter electrode consisted of a Li metal material. The coin cells were then filled with LPX electrolyte (1 M Lithium hexafluorophosphate ( $\text{LiPF}_6$ ) in 1:1:3 weight proportion of ethylene carbonate (EC), ethyl methyl carbonate (EMC), and dimethyl carbonate (DMC)).

Then, electrochemical characterizations were performed at 25 °C, at rate of C/10 in lithiation and delithiation state, to extract the potential and the specific capacity of both electrodes (4.25 mAh for the negative electrode and 3.51 mAh for the positive electrode). The electrode potentials were measured versus Li+/Li. The Open Circuit Potential (OCP) of both electrodes is deduced by averaging the electrode potential signals in lithiation and delithiation state as shown in FIGURE II- 2.

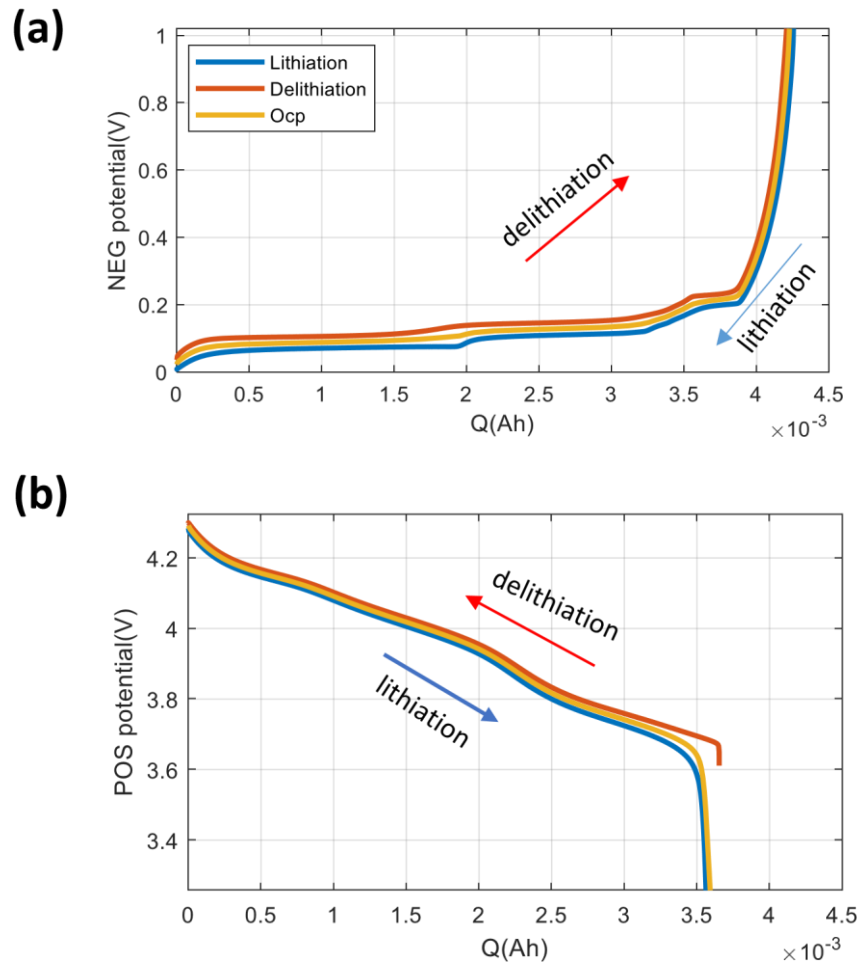


FIGURE II- 2: POTENTIAL SIGNALS VERSUS SPECIFIC CAPACITIES FOR THE A) NEGATIVE ELECTRODE AND B) POSITIVE ELECTRODE C/10.

## II.2. Protocol of check-up on 43 Ah Gr/NMC-LMO for aging tests

A periodical characterization (also known as ‘check-up’) was performed on the cells to record their capacity and internal resistance evolution during aging. First, for the capacity measurement, the cell was charged with a constant current (CC) at a rate of C/10 until it reached the maximum voltage of 4.2V and then at constant voltage (CV) with a floating voltage of 4.2 V until the current drops to the minimum admissible current 2.2 A (C/20). Following the charge mode, the cell was discharged at constant current at C/10 until the minimum voltage of 3 V and then at constant voltage (3V) until the current reaches the value of 2.2 A (C/20). We notice a difference between galvanostatic charge and discharge curves approximately equal to 40 mV. The charge and discharge galvanostatic responses at C/10 carried out from this protocol can be averaged to estimate the cell open-circuit voltage (OCV) as illustrated in

FIGURE II- 3.

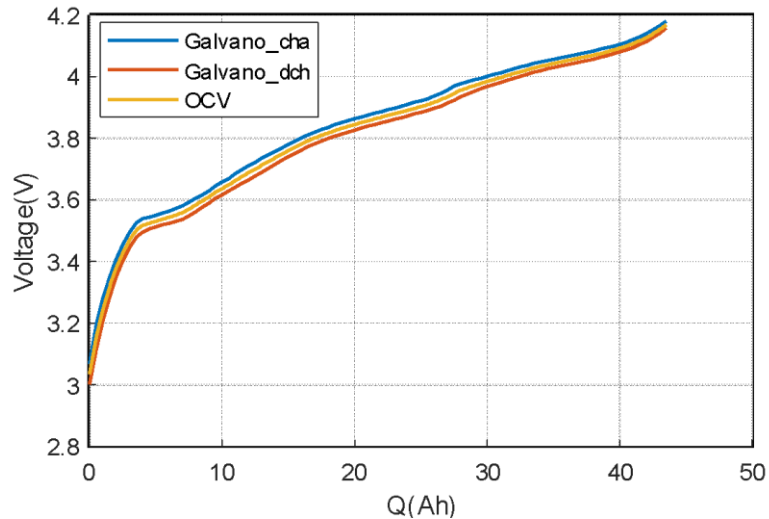


FIGURE II- 3: OCV PERIODICAL MEASUREMENTS ON THE PRODUCTION CELL

### II.3. Aging campaign and experimental results

The aging tests presented in this following chapter are applied on a module compound of three cells.

The temperature and SOC profile (value of Temperature and SOC during the whole aging process) are respectively set at  $T=25^{\circ}\text{C}$  and  $\text{SOC}=100\%$  during the check-up measurements period for the simulation of the MOBICUS aging model that will be described in the next chapter.

Calendar aging is influenced by temperature and state-of-charge. Three different aging conditions are studied in the storage mode: fixed calendar (fixed SOC and temperature), Thermal cycling (variable temperature at fixed SOC) and variable SOC aging (variable SOC at fixed temperature). For this test campaign, the target SOC is reached by discharging a fixed charge quantity defined as a ratio of nominal capacity. Depending on the capacity degradation, this protocol may present a drift of SOC relative to actual capacity during calendar aging tests. An example is shown [FIGURE II- 4](#) below for the calendar condition at temperature  $60^{\circ}\text{C}$  and SOC 65%.

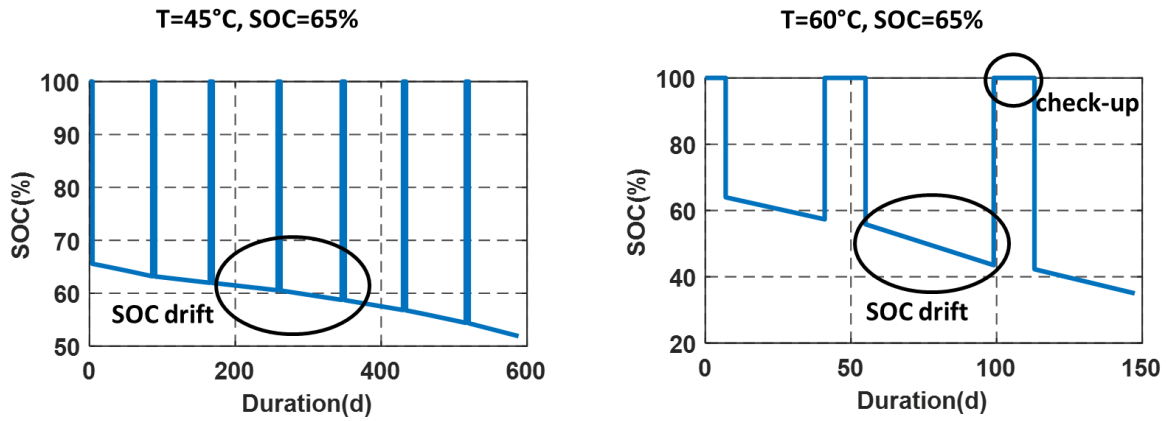


FIGURE II- 4: SOC PROFILE FOR CALENDAR CONDITION AT TEMPERATURE 45°C AND 60°C, SOC=65%.

Three calendar aging conditions were studied during the project: the fixed calendar, thermal cycling, and variable SOC aging tests. The experimental measurements of the cell SOH along with aging are presented in the following sections for the three aging tests. In addition, experimental measurements of the galvanostatic charge and discharge signals at C-10 rate are illustrated for the thermal cycling conditions. The average of the charge and discharge signals is used for the measurements of the cell SOH described in § 3.1.

### II.3.1. Experimental measurements of the cell SOH

#### II.3.1.1. Fixed calendar conditions

Fixed calendar aging was applied for more than one year of resting mode. The production modules were stored at 4 different temperatures namely 0 °C, 25 °C, 45 °C and 60 °C and 5 different states of charge (SOC), namely 0%, 30%, 65 %, 80 % and 100 % as summed up in TABLE II- 2.

	SOC 0%	SOC 30%	SOC 65%	SOC 80%	SOC 100%
T 0°C		X		X	X
T 25°C				X	
T 45°C	X	X	X	X	X
T 60°C			X	X	X

TABLE II- 2: FIXED CALENDAR AGING CONDITIONS.

During the resting time, periodical characterization of the cell capacity was measured every 12 weeks to quantify the battery SOH.

To study the influence of the SOC, FIGURE II- 5(a) below shows the evolution of cell SOH at temperature 45°C at five resting SOC namely 0%,30%, 65%, 80% and 100%. At SOC 0% the degradation of the cell capacity is very low. We can observe a higher degradation rate at SOC 30% but above all at higher SOC (65%, 80%, 100%). The SOH fading is more important at SOC 80% compared to SOC 100%. Surprisingly, the calendar condition at 65% is the most damaging

test and shows a very peculiar trend as well with a slope discontinuity after 79% of SOH representing a sudden cell capacity drop.

FIGURE II- 5(b) illustrates the cell degradation at temperature 60°C for three storage SOC, namely 65%, 80% and 100%. We observe the same trend at 45°C and 60°C for the capacity evolution: the cell SOH is more affected by the storage at SOC 65% than 80%. The cell capacity is still less influenced with a resting condition at SOC 100%.

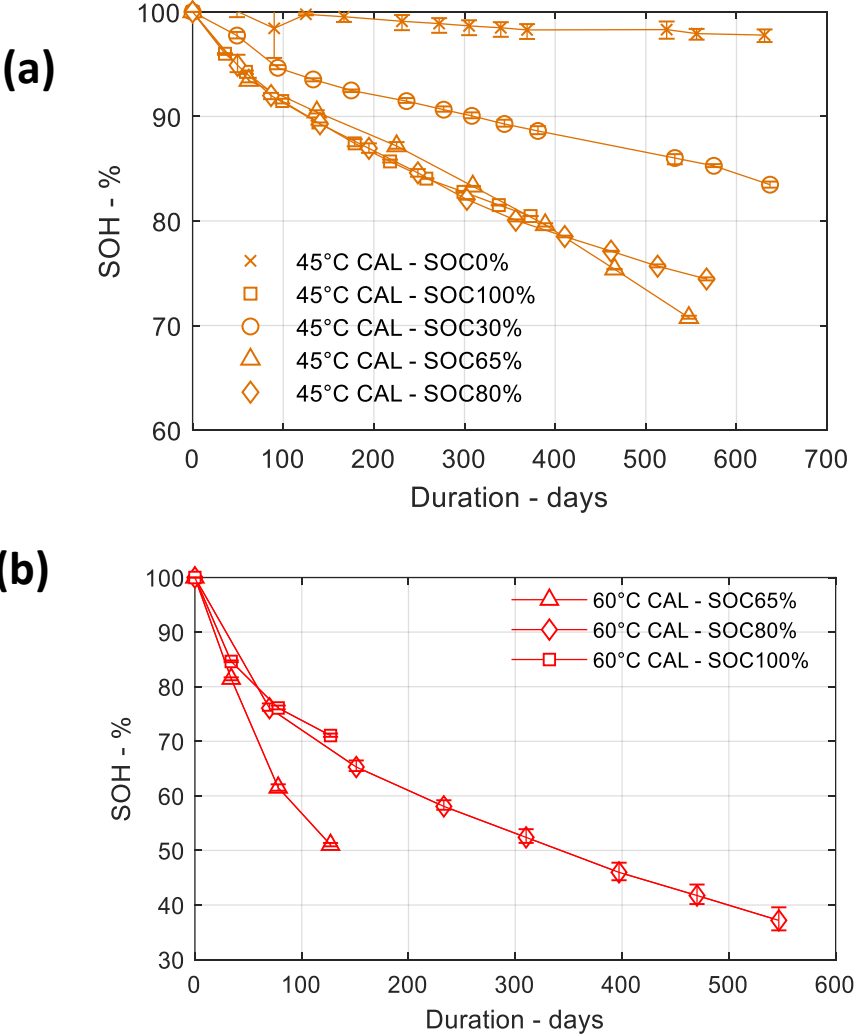


FIGURE II- 5: SOH DEGRADATION AT T=45°C (A) AND AT T=60°C (B).

The influence of the resting temperature is shown FIGURE II- 6, which presents the capacity loss at SOC 80% for four temperatures namely 0°C, 25°C, 45°C and 60°C. The temperature has a large impact on the cell degradation, which increases at a higher temperature. For instance, at 0°C, 25°C and 45°C, the cell SOH is still higher than 80% after 400 days of storage. However, it falls below 70% within 120 days for calendar aging at 60°C. Comparing the overall evolution of the cell capacity at temperature 60°C, we can notice a much larger degradation rate during the first phase of the battery lifetime (<80 days).

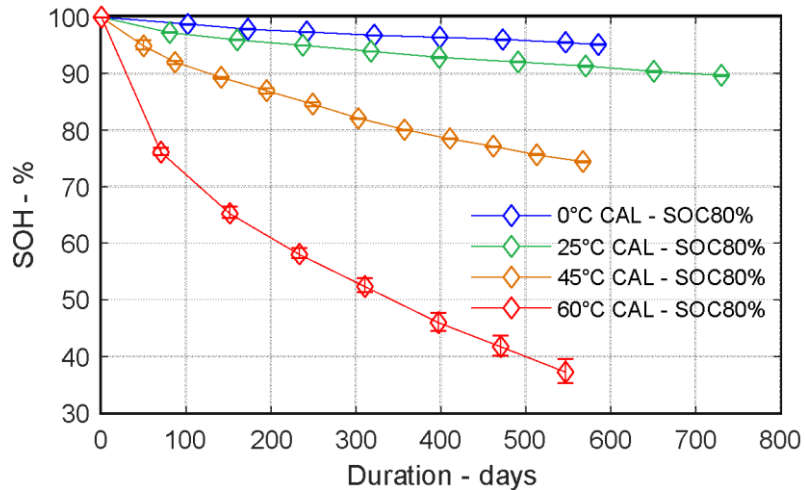


FIGURE II- 6: SOH DEGRADATION AT SOC 80%.

### II.3.1.2. Thermal cycling, fixed SOC

The thermal cycling is more representative of real usage when the storage temperature can vary due to environmental conditions. Performing such a test allows evaluating if thermal variations, here at day scale, can occur additional aging comparing to static calendar conditions.

The cells were stored at a fixed SOC, i.e. 65% or SOC 100%. Thermal cycling was then executed by alternately changing the temperature between 0°C and 30°C with a frequency of one thermal cycle per day for 11 weeks, followed by 1 week of capacity measurement (check-up). After that, the temperature is daily by turns set from 30°C to 60°C for another 11 weeks followed by 1 week of check-up for the capacity measurement. The SOC profile for the thermal cycling at SOC 65% is shown in [FIGURE II- 7](#) and presents a SOC drift from SOC 65% to 30% at the end of aging.

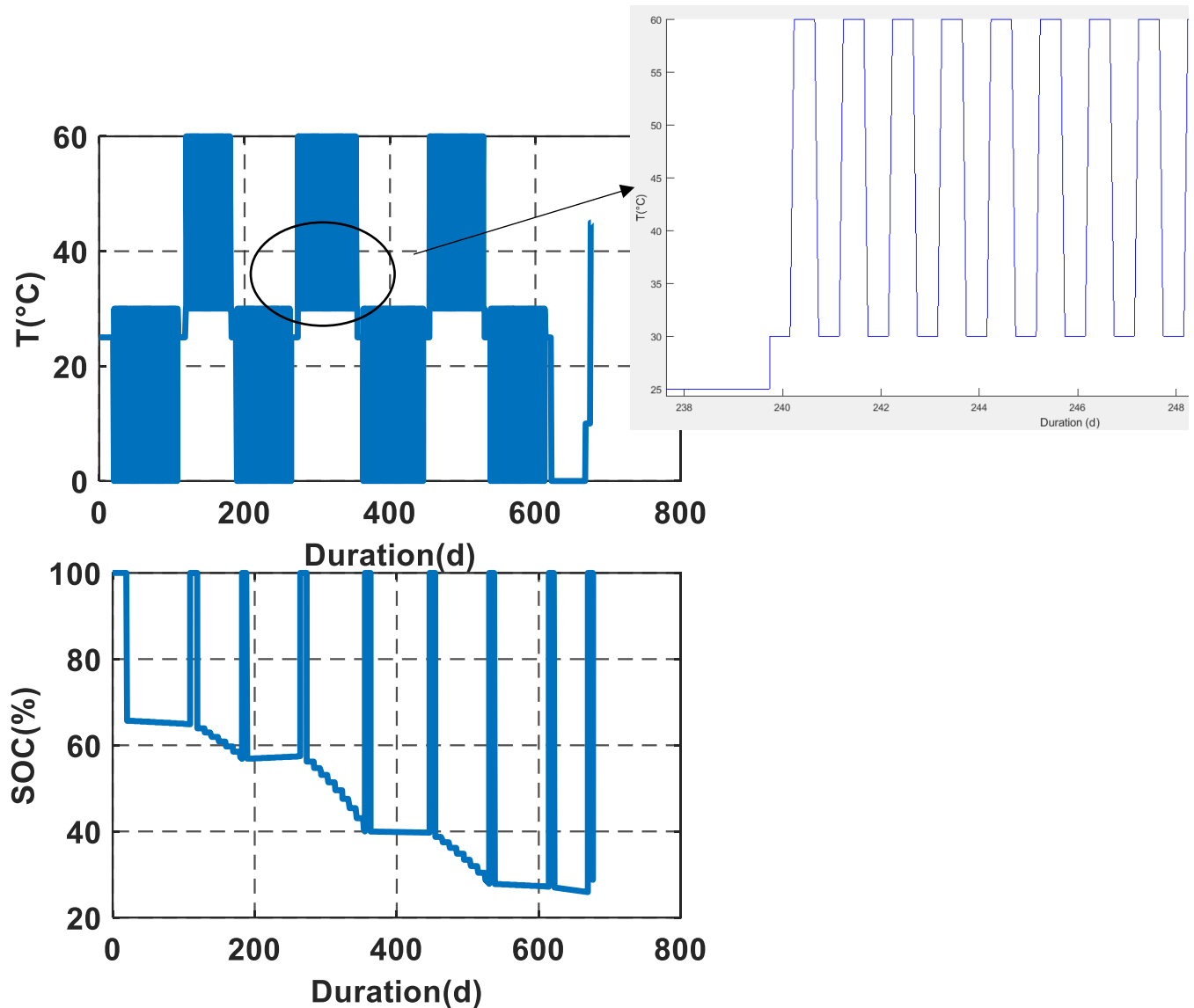


FIGURE II- 7: TEMPERATURE AND SOC USAGE PROFILE FOR THERMAL CYCLING AT SOC 65%.

FIGURE II- 8 shows the evolution of the cell SOH during these thermal cycling aging tests. Analyzing the usage profile in FIGURE II- 7 and the experimental results on the cell SOH in FIGURE II- 8, we can notice that the thermal cycling between [30°C-60°C] is more damaging than cycling between [0°C-30°C]. This result highlights the influence of higher temperature storage on the acceleration of the cell SOH fading. For the SOC dependence on thermal cycling, the degradation rate is overall more important at 65% of SOC compared to the SOC 100% as illustrated in FIGURE II- 8.

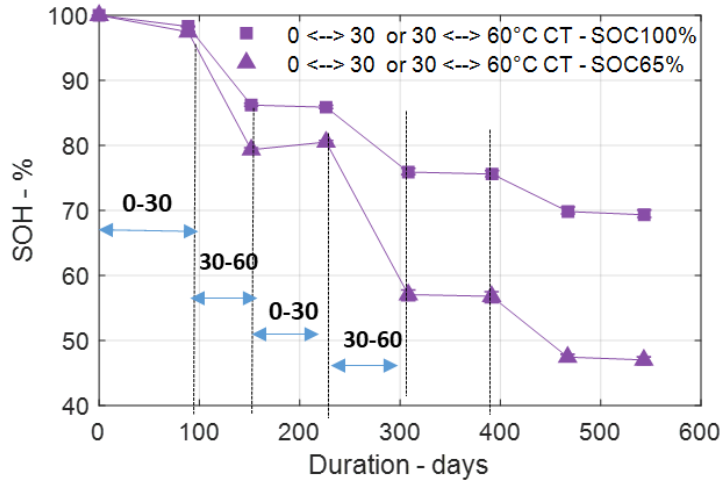


FIGURE II- 8: SOH DEGRADATION IN THERMAL CYCLING AGING (SOH 65% AND 100%).

### II.3.1.3. Variable SOC, fixed temperature

For vehicle usage, the battery SOC during the parking period will vary depending on the charge and drive phase sequences. Hence, specific aging tests have been performed to represent this usage. It consists of performing a calendar tests at a fixed temperature of 45°C meanwhile, the SOC is set for 2 months alternatively at two levels: 30% and 80%. Due to low expected degradation at SOC 30%, only one check-up is made after the 2 months of storage. However, this frequency has been increased to 1 month during storage at SOC 80%. FIGURE II- 9 shows recombined SOC evolution during this aging test. Periods at SOC 100% are representative of the check-up phase.

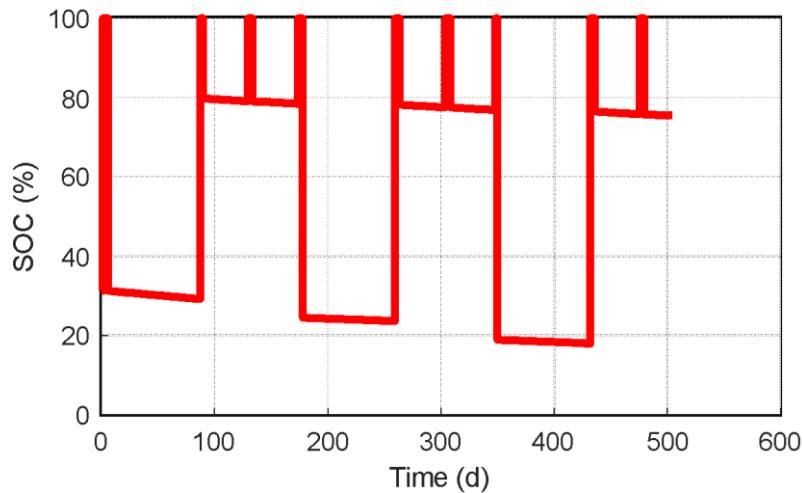
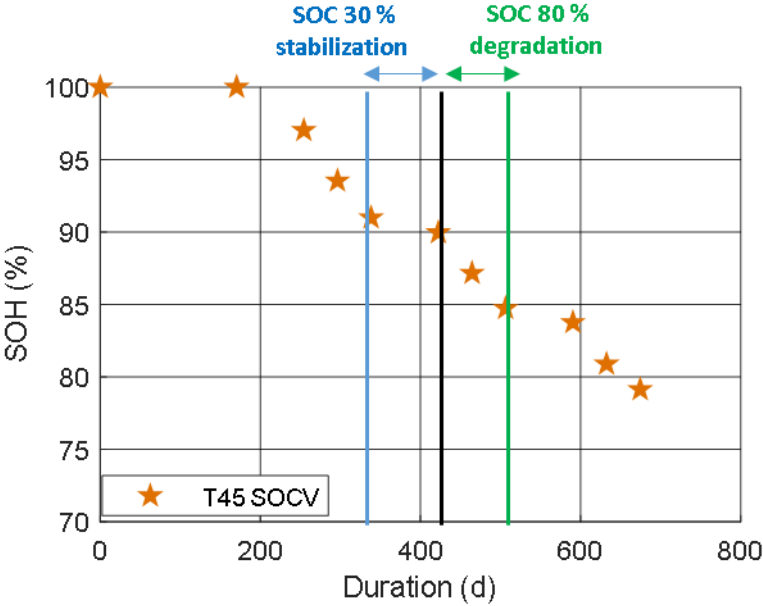


FIGURE II- 9: USAGE PROFILE FOR VARIABLE SOC AGING.

We can also notice a SOC drift in FIGURE II- 9 since the SOC update before storage is carried out with an Ah criterion proportional to the nominal capacity which decades with aging due to the battery self-discharge.

The periodical measurement of the capacity shows that the variation of the SOC from 30% to 80% also affects the cell SOH. As shown in **FIGURE II- 10**, lower SOC (SOC 30%) decrease the battery SOH fading but higher resting SOC (SOC 80%) lead to an important decrease of the cell SOH.



**FIGURE II- 10: SOH DEGRADATION DUE TO VARIABLE SOC AGING.**

**II.3.2. Experimental measurements of the cell voltage at C-10**

The galvanostatic charge and discharge voltages, measured on one cell at C/10, at different aging states are shown in **Figure II- 11**. The two calendar aging conditions illustrated in **Figure II-2** are the thermal cycling conditions at SOC 65% and 100%. The voltage gap between the charge and discharge signals increases along with aging due to the hysteresis effect.

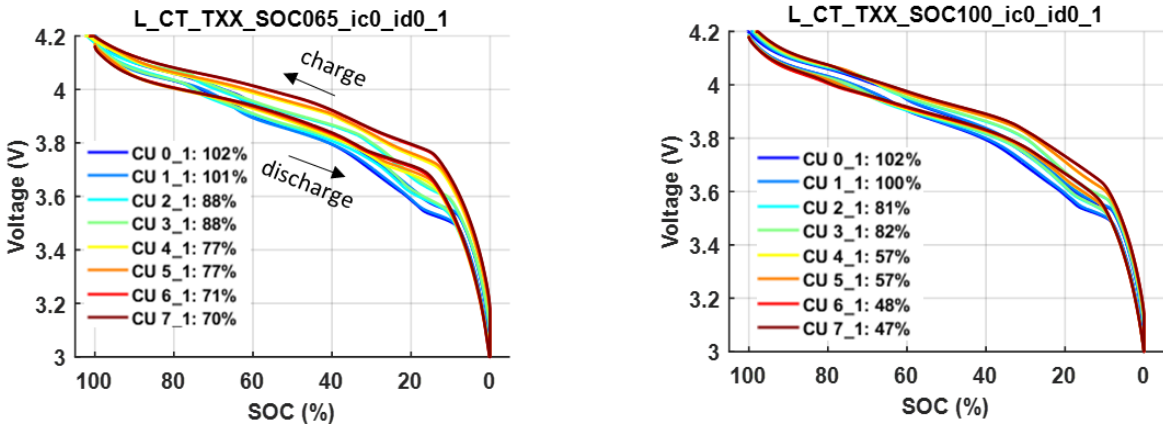


**FIGURE II- 11: GALVANOSTATIC CHARGE AND DISCHARGE MEASUREMENTS OF THE CELL VOLTAGE AT C/10**

CHAPTER 3: ONE-TANK AGING MODEL

## Introduction

This chapter gives on the one hand, a description of the semi-empirical aging models built during the MOBICUS project and, on the other hand, addresses the development of the one tank model aging proposed in this thesis work. Both aging model results are compared to the calendar experimental aging campaign presented in the previous chapter (§. II.3).

The semi-empirical aging model developed during the MOBICUS project for the prognosis of the production graphite-NMC/LMO capacity is detailed in the first section of this chapter.

The second part addresses the development of another semi-empirical aging model, the one-tank aging model. The one-tank and MOBICUS aging models have the same aging laws, and the study is performed only on calendar aging. However, the accelerating factors of the one-tank aging law consider the coupling effect between SOC and temperature along with aging.

In the third part of this chapter, a comparison is made between the MOBICUS and the one-tank aging models to analyze the precision of the prognosis.

### III.1. MOBICUS aging model

#### III.1.1. MOBICUS aging laws

The MOBICUS aging model, initially developed during the project by CEA team<sup>1</sup>, is a semi-empirical aging model based on the evolution of the cell capacity. The model allows following the degradation rate of the capacity loss depending on the usage profile on calendar aging (temperature, state-of-charge). This approach based on Broussely et al. [40] and fully detailed by PILIPILI Matadi et al. [71] expressed the capacity loss by:

$$\frac{dQ_{loss}}{dt} = J_{cal}(T, SOC) * f_{deg}(Q_{loss}) \quad (3.1)$$

Where  $J_{cal}(T, SOC)$  is the degradation rate that depicts the influence of the temperature and state-of-charge on the cell aging and  $f_{deg}(Q_{loss})$ , the degradation loss function.

##### III.1.1.1. Degradation rate $J_{cal}$

$J_{cal}(T, SOC)$  considers the temperature and SOC accelerating factors:

$$J_{cal}(T, SOC) = J_{cal_{ref}} * Fa_{SOC}(SOC) * Fa_T(T) \quad (3.2)$$

$J_{cal_{ref}}$  being a proportional constant corresponding to the degradation rate at reference temperature and SOC ( $T_{ref}, SOC_{ref}$ ).  $Fa_{SOC}(SOC)$  is the SOC accelerating factor which depends only on the SOC while  $Fa_T(T)$  is the temperature accelerating factor which depends exclusively on the temperature.

---

<sup>1</sup> K. Mergo-Mbeya, M. Montaru

### III.1.1.1.1 SOC accelerating factor

$Fa_{SOC}$ , the SOC accelerating factor is expressed as the polynomial function:

$$Fa_{soc}(SOC) = \frac{a_{cal.0} + a_{1.cal} \cdot \left(\frac{SOC}{SOC_{ref}}\right) + a_{2.cal} \cdot \left(\frac{SOC}{SOC_{ref}}\right)^2 - a_{cal.3} \cdot \exp\left(a_{cal.4} \cdot \frac{SOC}{SOC_{ref}}\right)}{a_{cal.0} + a_{cal.1} + a_{cal.2} - a_{cal.3} \cdot \exp(a_{cal.4})} \quad (3.3)$$

Where ( $a_{cal.0} \dots, a_{cal.4}$ ) are some constant parameters,  $SOC$  the state of charge (in %) and  $SOC_{ref}$  the reference SOC (in %).

### III.1.1.1.2 Temperature accelerating factor

$Fa_T$ , the temperature accelerating factor is based on an Arrhenius function:

$$Fa_T(T) = \exp\left(-\frac{E_{a.cal}(T)}{R} \cdot \left(\frac{1}{T + T_0} - \frac{1}{T_{ref} + T_0}\right)\right) \quad (3.4)$$

Where  $T$  is the temperature during storage in kelvin (K),  $T_0$  equal to 273.15 K,  $T_{ref}$  the reference temperature,  $R$  the universal gas constant and  $E_{a.cal}(T)$  the activation energy, which is considered as an affine function of the temperature:

$$E_{cal.a}(T) = \alpha_{cal} \cdot (T - T_{ref}) + E_{aref\_cal} \quad (3.5)$$

where,  $\alpha_{cal}$  and  $E_{aref\_cal}$  are some constant parameters.

### III.1.1.2. Degradation loss function $f_{deg}$

$f_{deg}(Q_{loss})$  is a degradation function based on broussely et al. [72] approach:

$$f_{deg}(Q_{loss}) = \frac{1}{1 + A * Q_{loss}} \quad (3.6)$$

Where  $A$  is a constant parameter and  $Q_{loss}$  the cell capacity loss.

## III.1.2. Identification of the parameters of the MOBICUS aging model

### III.1.2.1. Identification method and results

During the MOBICUS project, all the calendar conditions listed in chapter 2 (TABLE II-2), except the calendar condition at temperature 60°C and SOC 65% & 100%, were used from the MOBICUS aging model development. These two conditions were not forecasted initially and were started 2 years after the beginning of the rest of the tests campaign. In this section, all the calendar aging conditions included the temperature 60°C and SOC 65% & 100% are used for the identification process.

The identification process consists of identifying  $J_{cal}(T, SOC)$ , which depends on  $J_{cal_{ref}}$  and the acceleration factors ( $Fa_T, Fa_{SOC}$ ). The parameter  $A$  in equation (3.6) is also identified. To do so, an optimization method is carried out via MATLAB/Simulink software using the function 'lsqcurvefit' to find the optimal solution for  $J_{cal}(T, SOC)$  and  $A$ . This optimal solution is found by minimizing the root mean square error (RMSE) between the simulated cell capacity from the MOBICUS aging model and experimental capacity data (in chapter 2).

The SOC accelerating factor  $Fa_{SOC}$  is identified via ( $a_{cal.0} \dots a_{cal.4}$ ) at four different breakpoints of SOC namely 0%, 30%, 65%, 80%. The reference condition, where the SOC accelerating factor  $Fa_{SOC}$  is equal to 1, corresponds to SOC breakpoint  $SOC_{ref} = 100\%$ . To identify the  $Fa_{SOC}$  between these five SOC breakpoints, the analytic expression of  $Fa_{SOC}$  described in Eq. (3.3) is used.

The temperature accelerating factor is identified via  $\alpha_{cal}$  and  $E_{aref\_cal}$  at four breakpoints of temperature namely 0°C, 25°C, 45°C, and 60°C. The reference condition, where the T accelerating factor  $Fa_T$  is equal to 1, corresponds to  $T = T_{ref} = 45^\circ C$ . To obtain the accelerating factor  $Fa_T$  between the breakpoints of T, the analytical equation of  $Fa_T$  described in Eq. (3.4) is used.

The results of the optimization process are given in TABLE III- 1 below:

Parameters		Unit
$J_{cal_{ref}}$	0.12	Ah/days
$\alpha_{cal}$	868	J/(mol.K)
$E_{aref\_cal}$	87	KJ/mol
$a_{cal.0}$	1.73	w.u.
$a_{cal.1}$	0.34	w.u.
$a_{cal.2}$	0.02	w.u.
$a_{cal.3}$	1.73	w.u.
$a_{cal.4}$	0.19	w.u.
A	0.80	$Ah^{-1}$

TABLE III- 1: IDENTIFICATION OF THE MOBICUS AGING MODEL PARAMETERS.

Using the values from TABLE III- 1, the evolution of temperature and SOC accelerating factors ( $Fa_{SOC}(SOC)$  and  $Fa_T(T)$ ) are represented in FIGURE III- 1. As shown in FIGURE III- 1, the degradation rate of cell capacity is higher at SOC 65%. The calendar aging at high temperatures impacts the most the cell SOH, especially at 60°C.

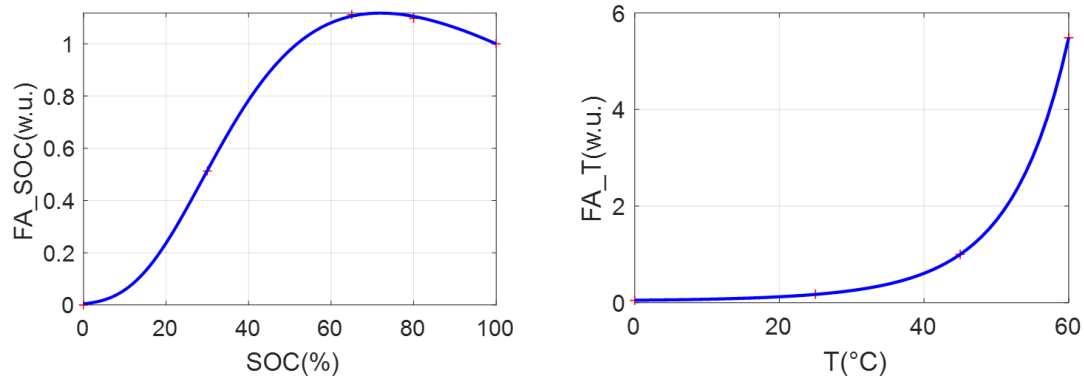


FIGURE III- 1: SOC AND TEMPERATURE ACCELERATING FACTORS.

### III.1.2.2. Experimental and simulated cell SOH from the MOBICUS aging model

The results from the identification process allow us to superimpose the experimental cell SOH data (in chapter 2, §. II.3) and the simulated cell SOH from the MOBICUS aging model as illustrated in [FIGURE III- 2](#).

At temperature 0°C, the MOBICUS aging model overestimates the cell aging at SOC 30% and 100% but fits well the experimental data at temperature 0°C and SOC 80%. The model is accurate as well at a temperature of 25°C and 80% of SOC.

At temperature 45°C and SOC 0%&30%, the MOBICUS aging model still overestimates the cell aging. At temperature 45°C and 65% of SOC, the estimation is acceptable except after 600 days of calendar aging where the model is unable to predict the break of SOH slope. Nevertheless, the SOH prognosis is good at temperature 45°C and high SOC 80%&100 where the model success to match closely the experimental data.

At temperature 60°C, the MOBICUS aging model gives a good estimation of the cell SOH at SOC 80% and 100% but fails to correctly predict the cell capacity evolution at SOC 65%. The model developed during the MOBICUS project may be inefficient to model the phenomenon responsible for the capacity fading for this calendar condition at SOC 65%.

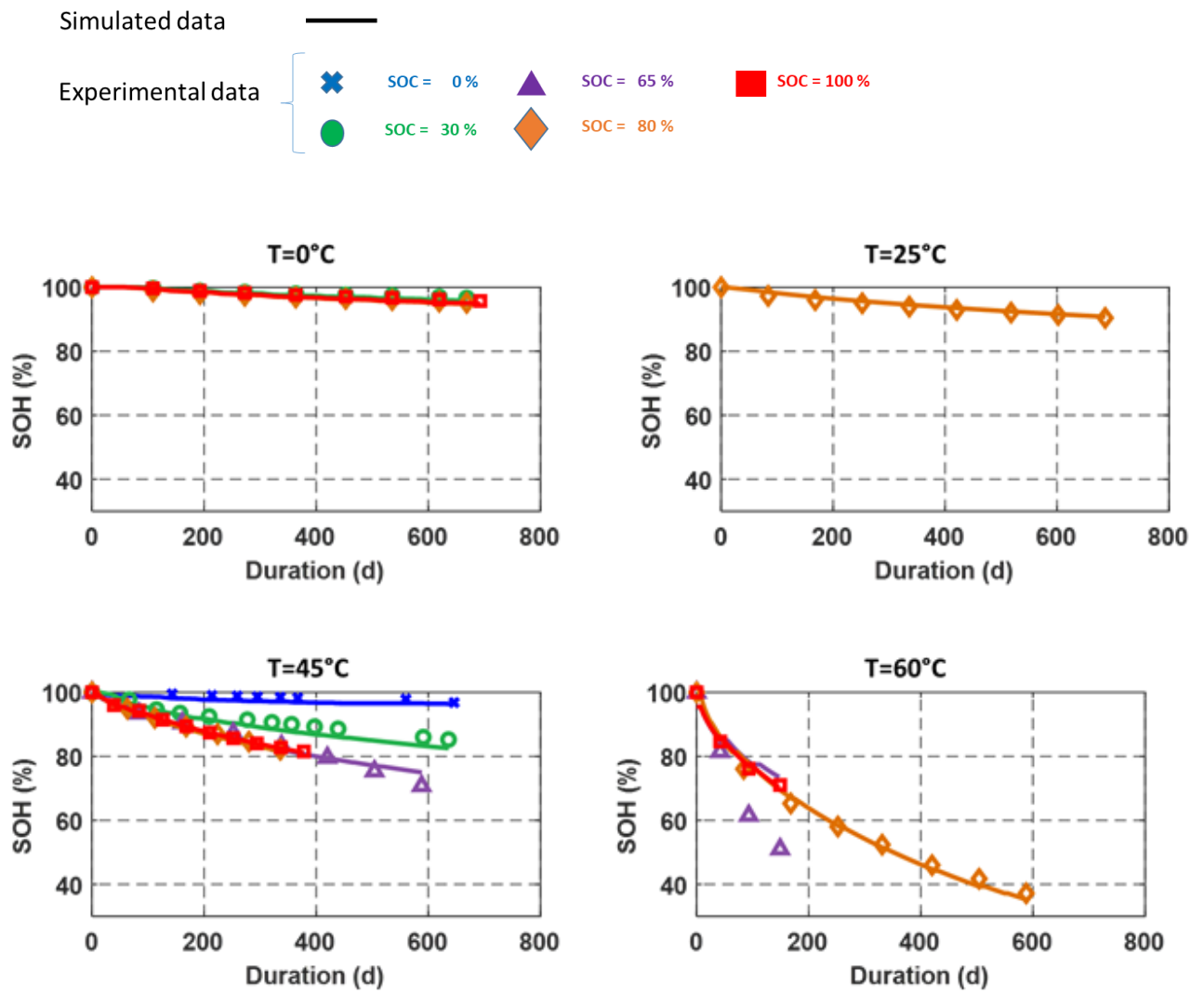


FIGURE III- 2: COMPARISON BETWEEN EXPERIMENTAL AND SIMULATED SOH FROM THE MOBICUS AGING MODEL

### III.1.2.3. MOBICUS aging model error

The error (Root mean square error calculation) between the experimental and simulated cell SOH from the MOBICUS aging model is illustrated in **FIGURE III- 3**.

At 0°C and 25°C, there is a very good correspondence between the model and the experimental data, the error is less than 1.7%.

The prediction of the cell SOH aging is also good at 45°C for all SOC with a maximum error reaching 4% for the calendar condition at 30% of SOC. The prediction is very good at SOC 100% with a maximum error below 0.5%.

Furthermore, there is a good correspondence between the experimental data and the model at 60°C for 80% and 100% of SOC. However, the error is high at SOC 65%, reaching 20%, which is the only condition where the MOBICUS aging model struggles to predict the cell SOH aging.

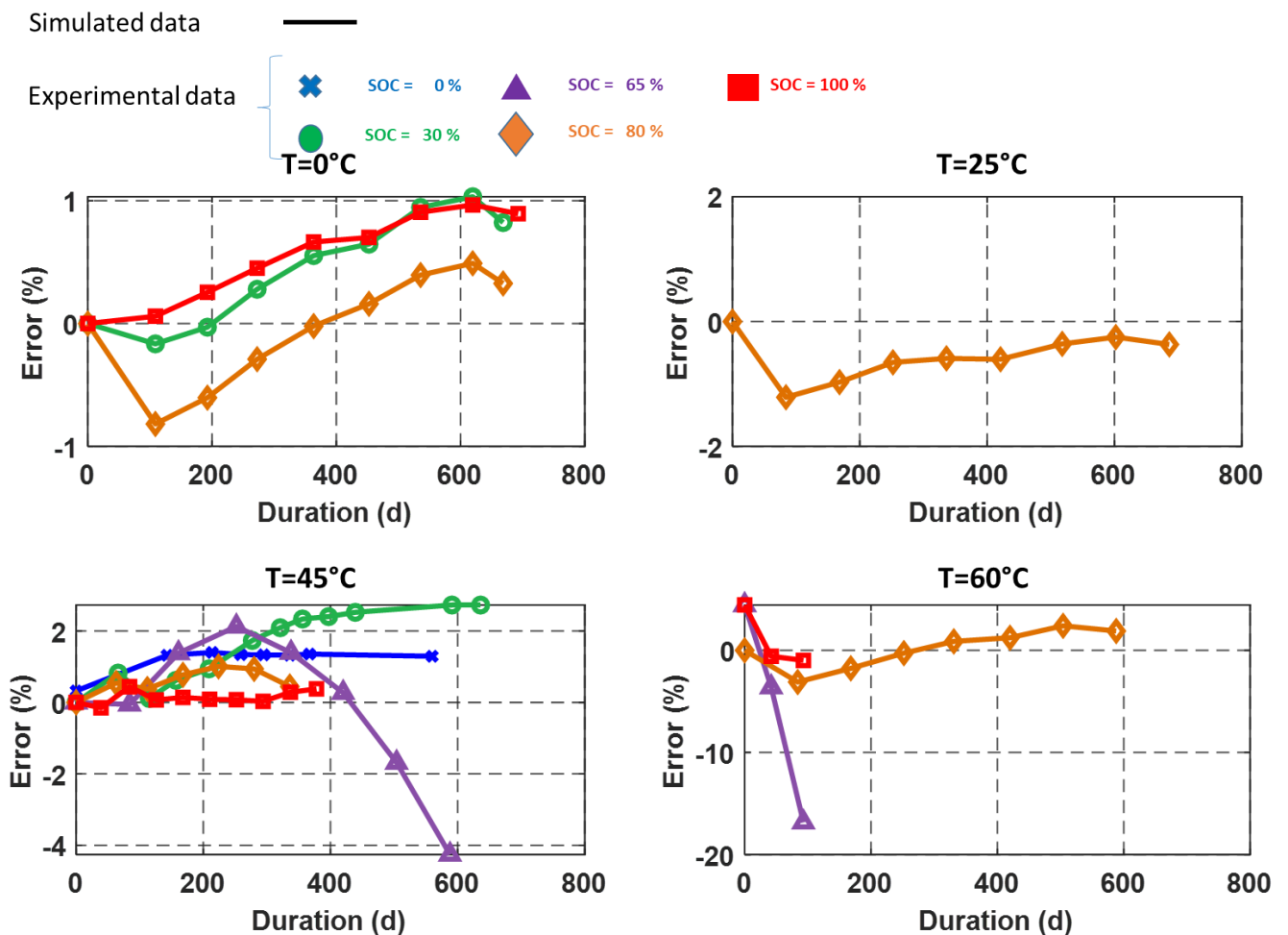


**FIGURE III- 3: ERROR BETWEEN EXPERIMENTAL AND SIMULATED CELL SOH FROM THE MOBICUS AGING MODEL**

### III.1.3. Model validation

To validate the MOBICUS aging model, three aging conditions mentioned in chapter 2 are simulated by using the values in TABLE II-2. Those are the calendar condition at 45°C and variable SOC (between SOC 30%-80%) and the two-thermal cycling (between 0°C-30°C and 30°C-60°C) conditions at SOC 65% and 100%. FIGURE III-4 compares the simulated cell capacity from the MOBICUS project and the experimental data as well as the error between them.

The prediction of the cell SOH with the MOBICUS aging model is very satisfactory for the calendar condition at temperature 45°C when varying the SOC from 30% to 80% of SOC. The maximum error reached is below 2.5%.

It is worth reminding for the thermal cycling conditions at 65% and 100% of SOC that the flat plateaus in FIGURE III-4 correspond to the thermal cycling between 0°C-30°C. The rapid break of slope in cell SOH is related to the cycling between 30°C-60°C. The temperature profile for the thermal cycling condition is illustrated in FIGURE II-7 in chapter 2. Concerning the thermal cycling at SOC 100%, the MOBICUS aging model can forecast the SOH with a maximum error below 4%. However, for the thermal cycling at 65% of SOC, the simulated cell SOH from the MOBICUS aging model is very far from the cell SOH measured during aging. The model seems insufficient to consider the fast cell degradation at SOC 65% when cycling between 30°C-60°C.

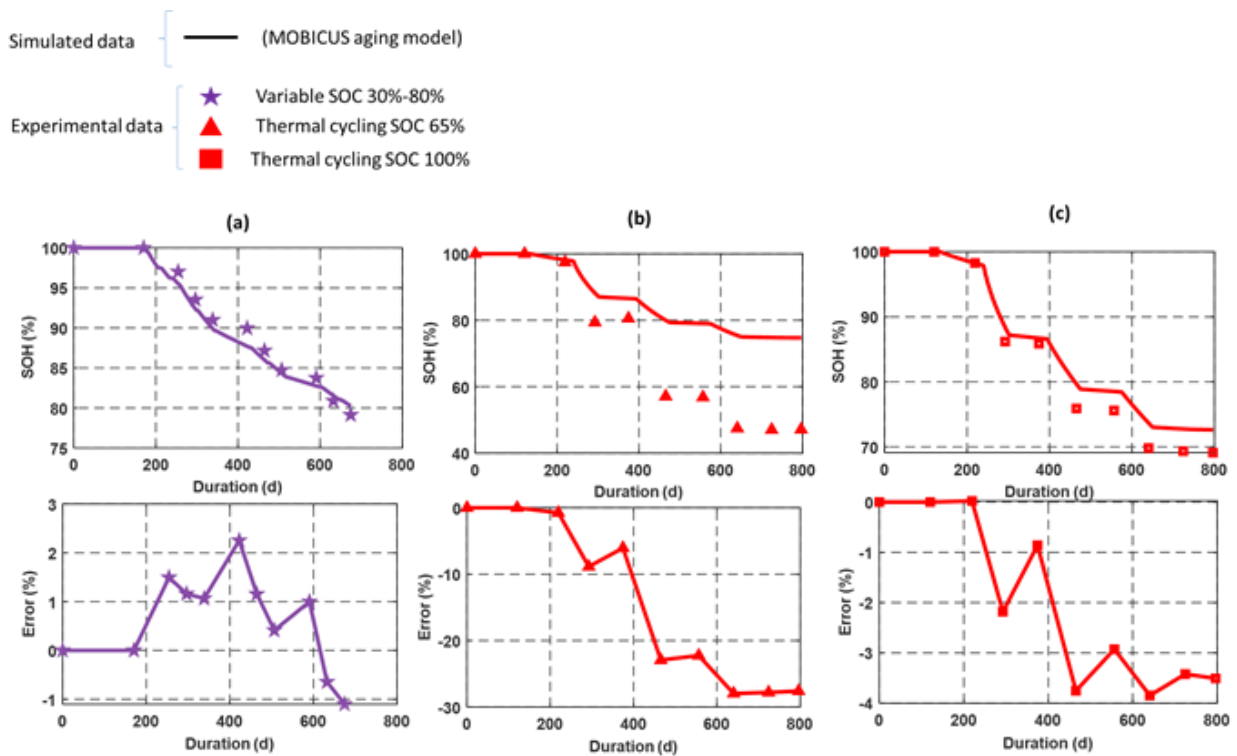


FIGURE III-4: VALIDATION AND ERROR FROM THE MOBICUS AGING MODEL FOR THE VARIABLE SOC (A), THERMAL CYCLING AT 65% OF SOC (B) AND 100% OF SOC (C).

## III.2. One-tank aging model

In the following section, an improvement to consider the SOC influence on the MOBICUS aging model is proposed. Another aging model, the one-tank aging model, is built to consider the coupling effect of the temperature and SOC. Regarding the previous observations during the identification (at temperature 60°C, SOC 65%) and validation process (thermal cycling at SOC 65%) it appears the SOC accelerating factor  $Fa_{SOC}$  is not sufficient to express the SOC influence on aging.

### III.2.1. One-tank aging model laws

The capacity loss is expressed the same way as the MOBICUS aging law described by equation (3.1) and depending on the degradation  $J_{cal}(T, SOC)$  and the degradation function  $f_{deg}$ .

#### III.2.1.1. Degradation rate $J_{cal}$

$J_{cal}(T, SOC)$  considers the temperature and SOC accelerating factor:

$$J_{cal}(T, SOC) = J_{cal_{ref}} * Fa_{SOC} * Fa_{T, SOC} \quad (3.7)$$

Where  $J_{cal_{ref}}$  is a constant parameter corresponding to the degradation rate at the reference temperature and SOC ( $T_{ref}, SOC_{ref}$ ). As in the previous model,  $Fa_{SOC}(SOC)$  is the SOC accelerating factor which depends only on the SOC while  $Fa_{T, SOC}(T, SOC)$  is the temperature accelerating factor which depends on both the temperature and SOC.

#### III.2.1.1.1 State-of-charge accelerating factor

$Fa_{SOC}$ , illustrated in FIGURE III- 5(a), is the state-of-charge accelerating factor. It is a vector, which is a function of a vector of SOC:

If we consider a SOC vector with a dimension n:

$$SOC = [SOC_1 \dots \dots SOC_n] \quad (3.8)$$

Thus, the state-of-charge accelerating factor can be expressed by n constants:

$$Fa_{soc} = [Fa_{soc_1} \dots \dots Fa_{soc_n}] \quad (3.9)$$

#### III.2.1.1.2 Temperature accelerating factor

The effect of the temperature is usually expressed with an Arrhenius law [34] by introducing the activation energy  $E_a$  parameter [73], [74]. Moreover, to traduce correctly empirical aging behavior, the activation energy is assumed different below and above the reference temperature  $T_{ref}$  fixed at 45°C. For the sake of accounting for a coupling effect between temperature and state-of-charge on aging behavior, the activation energy is also considered dependent on state-of-charge. The Arrhenius activation energy,  $E_{a_{T < T_{ref}}}(SOC)$  and  $E_{a_{T \geq T_{ref}}}(SOC)$  are vectors function of SOC illustrated FIGURE III- 5(b).

The stress factor, depending on the temperature, is then expressed by:

$$\exp \left( -\frac{E_{a_{T < T_{ref}}}(SOC)}{R} \left( \frac{1}{T} - \frac{1}{T_{ref}} \right) \right) \text{ if } T < T_{ref} \quad (3.10)$$

$$\exp \left( -\frac{E_{a_{T \geq T_{ref}}}(SOC)}{R} \left( \frac{1}{T} - \frac{1}{T_{ref}} \right) \right) \text{ if } T \geq T_{ref} \quad (3.11)$$

Where  $T$  is the temperature during storage,  $T_{ref}$  the reference temperature,  $R$  the universal gas constant,  $E_{a_{T < T_{ref}}}$  and  $E_{a_{T \geq T_{ref}}}$  the activation energy for temperature below and above the reference temperature.

### III.2.1.2. Degradation loss function $f_{deg}$

As in the previous model,  $f_{deg}(Q_{loss})$  is a degradation function based on broussely et al. [72] approach and described by Eq. (3.6).

### III.2.2. One-tank aging model parameters identification

#### III.2.2.1. Identification method and results

The identification process consists of identifying  $J_{cal}(T, SOC)$  which depends on  $J_{cal_{ref}}$ , the acceleration factors ( $Fa_T, Fa_{T, SOC}$ ) and the parameter  $A$ . In this section, the parameter  $A$  is fixed at the same value identified for the MOBICUS aging model to only analyze the influence on the change of  $J_{cal}(T, SOC)$  expression.

The accelerating factor  $Fa_{SOC}$  is identified at four breakpoints of SOC namely 0%, 30%, 65%, 80%.  $SOC_{ref} = 100\%$ ,  $Fa_{SOC}$  is considered equal to 1. The accelerating factor  $Fa_{SOC}$ , between the breakpoints of SOC, is calculated using linear interpolation.

Looking at the matrix of fixed calendar conditions (in chapter 2), we can notice that the parameter  $E_{a_T}(SOC)$  cannot be identified at all temperature for all SOC breakpoints due to a lack of data:

- For  $T < T_{ref}$  at SOC 0% and SOC 65%
- For  $T \geq T_{ref}$  at SOC 0%.

Note that there is a SOC deviation on the calendar condition at  $T=60^\circ\text{C}$  and SOC =65% where the SOC 30% is reached after 200 days of storage (illustrated in chapter 2, §. II.3) The activation energy  $E_{a_{T \geq T_{ref}}}(SOC)$  can then be identified at SOC 30%.

For this reason, we have chosen the following assumptions:

- $E_{a_{T < T_{ref}}}(SOC = 0\%) = E_{a_{T < T_{ref}}}(SOC = 30\%)$

- $E_{a_{T < T_{ref}}}(SOC = 65\%)$  is calculated using a linear interpolation of  $E_{a_{T < T_{ref}}}(SOC)$  between SOC 30% and 80%
- $E_{a_{T \geq T_{ref}}}(SOC = 0\%) = E_{a_{T \geq T_{ref}}}(SOC = 30\%)$

The activation energy  $E_{a_T}(SOC)$  at any temperature is then identified as followed:

- $E_{a_{T < T_{ref}}}(SOC)$  for  $T < T_{ref}$ : with 4 breakpoints of temperature namely 0°C, 25°C, 45°C, and 60°C, and three different breakpoints of SOC namely 30%, 80%, and 100%.
- $E_{a_{T \geq T_{ref}}}(SOC)$  for  $T \geq T_{ref}$ : with 4 breakpoints of temperature namely 0°C, 25°C, 45°C, and 60°C, and four different breakpoints of SOC namely 30%, 65%, 80%, and 100%.

This method is summed-up in TABLE III- 2 below:

SOC breakpoints (%)	0	30	65	80	100
$E_{a_{T < T_{ref}}}(SOC)$	$= E_{a_{T < T_{ref}}}(30\%)$	identified	interpolation	identified	identified
$E_{a_{T \geq T_{ref}}}(SOC)$	$= E_{a_{T \geq T_{ref}}}(30\%)$	identified	identified	identified	identified

TABLE III- 2: IDENTIFICATION AND ASSUMPTION ON THE ACTIVATION ENERGY (ONE-TANK AGING MODEL)

Finally, the activation energies ( $E_{a_{T < T_{ref}}}(SOC)$ ,  $E_{a_{T \geq T_{ref}}}(SOC)$ ), between the breakpoints of SOC, are calculated using linear interpolation. The temperature accelerating factor  $F_{a_{T,SOC}}(T, SOC)$  is then deducted using its analytic expression at any value of  $T$  from 0°C to 60°C.

The identification results are given in TABLE III- 3 below:

	Unit	Cell parameters
$J_{cal_{ref}}$	Ah/days	0.1
$E_{a_{T < T_{ref}}}(SOC = 30\%)$	$\text{kJ} \cdot \text{mol}^{-1}$	109
$E_{a_{T < T_{ref}}}(SOC = 80\%)$	$\text{kJ} \cdot \text{mol}^{-1}$	60
$E_{a_{T < T_{ref}}}(SOC = 100\%)$	$\text{kJ} \cdot \text{mol}^{-1}$	82
$E_{a_{T \geq T_{ref}}}(SOC = 30\%)$	$\text{kJ} \cdot \text{mol}^{-1}$	287
$E_{a_{T \geq T_{ref}}}(SOC = 65\%)$		75
$E_{a_{T \geq T_{ref}}}(SOC = 80\%)$	$\text{kJ} \cdot \text{mol}^{-1}$	128
$E_{a_{T \geq T_{ref}}}(SOC = 100\%)$	$\text{kJ} \cdot \text{mol}^{-1}$	110
$F_{a_{SOC}}(SOC = 0\%)$	w.u.	$2 \cdot e^{-14}$
$F_{a_{SOC}}(SOC = 30\%)$	w.u.	0.47
$F_{a_{SOC}}(SOC = 65\%)$	w.u.	1.21
$F_{a_{SOC}}(SOC = 80\%)$	w.u.	0.96
$F_{a_{SOC}}(SOC = 100\%)$	w.u.	1

TABLE III- 3: IDENTIFICATION OF THE ONE-TANK AGING MODEL PARAMETERS

FIGURE III- 5(a) and FIGURE III- 5(c) represent the temperature and SOC accelerating factors. The degradation rate of the cell capacity is more important at SOC 65% with an accelerating factor of  $Fa_{SOC}(SOC = 65\%)$  equal to 1.21.

For  $T < 45^{\circ}C$ , the activation energy  $Ea_{T < T_{ref}}(SOC)$  is the lowest at SOC 80% as shown in FIGURE III- 5(b). This explains why the degradation rate of  $Fa_{T,SOC}$  is higher at SOC 80% compared to the SOC 0% to 65%. It is worth reminding that the activation energy at SOC 65% when  $T < T_{ref}$  is obtained by linear interpolation between SOC 30% and 80% due to lack of data measurements. This could potentially favor a less accurate cell SOH estimation at SOC 65%. The dependency of the temperature follows an exponential law (Arrhenius law) which is even more accentuated at high temperature when  $\geq 45^{\circ}C$ . At temperature  $60^{\circ}C$  and SOC 30%,  $Fa_{T,SOC}$  is very high due to the energy activation, which is equal to 287.66 KJ/mol shown in FIGURE III- 5(b).

In both cases ( $T < 45^{\circ}C$  or  $T \geq 45^{\circ}C$ ) the activation energy at SOC 0% is kept constant to value at 30% of SOC, as illustrated in FIGURE III- 5(b), according to our hypothesis.

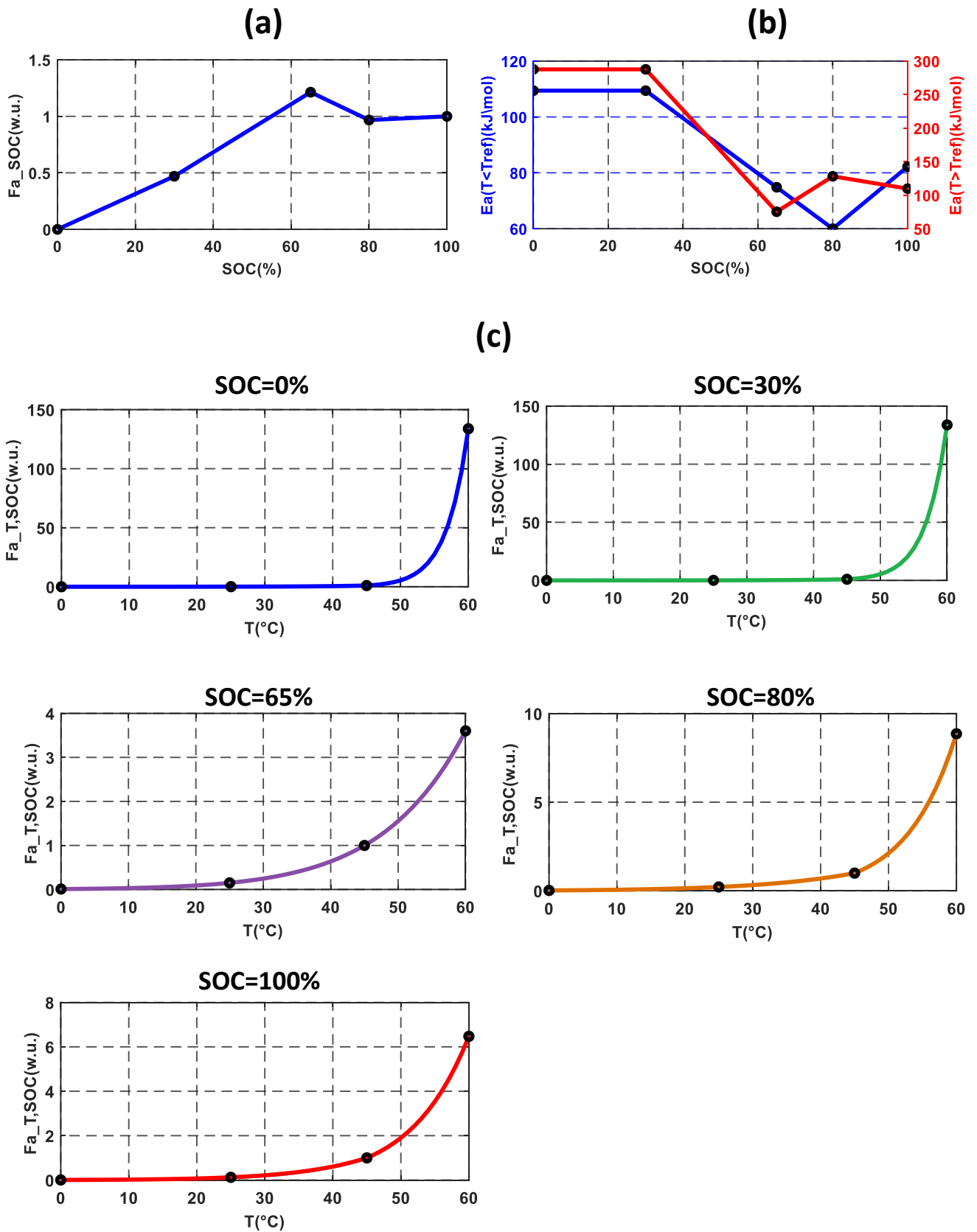


FIGURE III- 5: IDENTIFICATION OF TEMPERATURE (A), SOC ACCELERATING (B) FACTORS AND ACTIVATION ENERGY (C)

### III.2.2.2. Experimental and simulated cell SOH from the one-tank aging model

Using these parameters previously identified, the cell capacity for all calendar aging conditions is simulated. The results are shown in FIGURE III- 6, which compares the experimental cell SOH (detailed in chapter 2) with the simulated cell SOH from the one-tank aging model.

At  $T=0^{\circ}\text{C}$  and  $T=25^{\circ}\text{C}$ , the one-tank aging model gives a good agreement compared to the experimental SOH data for all SOC. There is a slight difference at SOC 100% after 400 days of storage, but the difference is very small.

At  $45^{\circ}\text{C}$  and SOC 0%, simulation results do not agree very well with experimental data. Nevertheless, the SOH fading is very small. For the other SOCs at this temperature (30% to 100%), the fitting is very good except after 500 days (>1.3 years) of storage at SOC 65%.

At  $60^{\circ}\text{C}$ , the one-tank aging model gives also a very good agreement compared to the experimental cell SOH data. At 65% of SOC, the agreement is nevertheless less good than the other conditions.

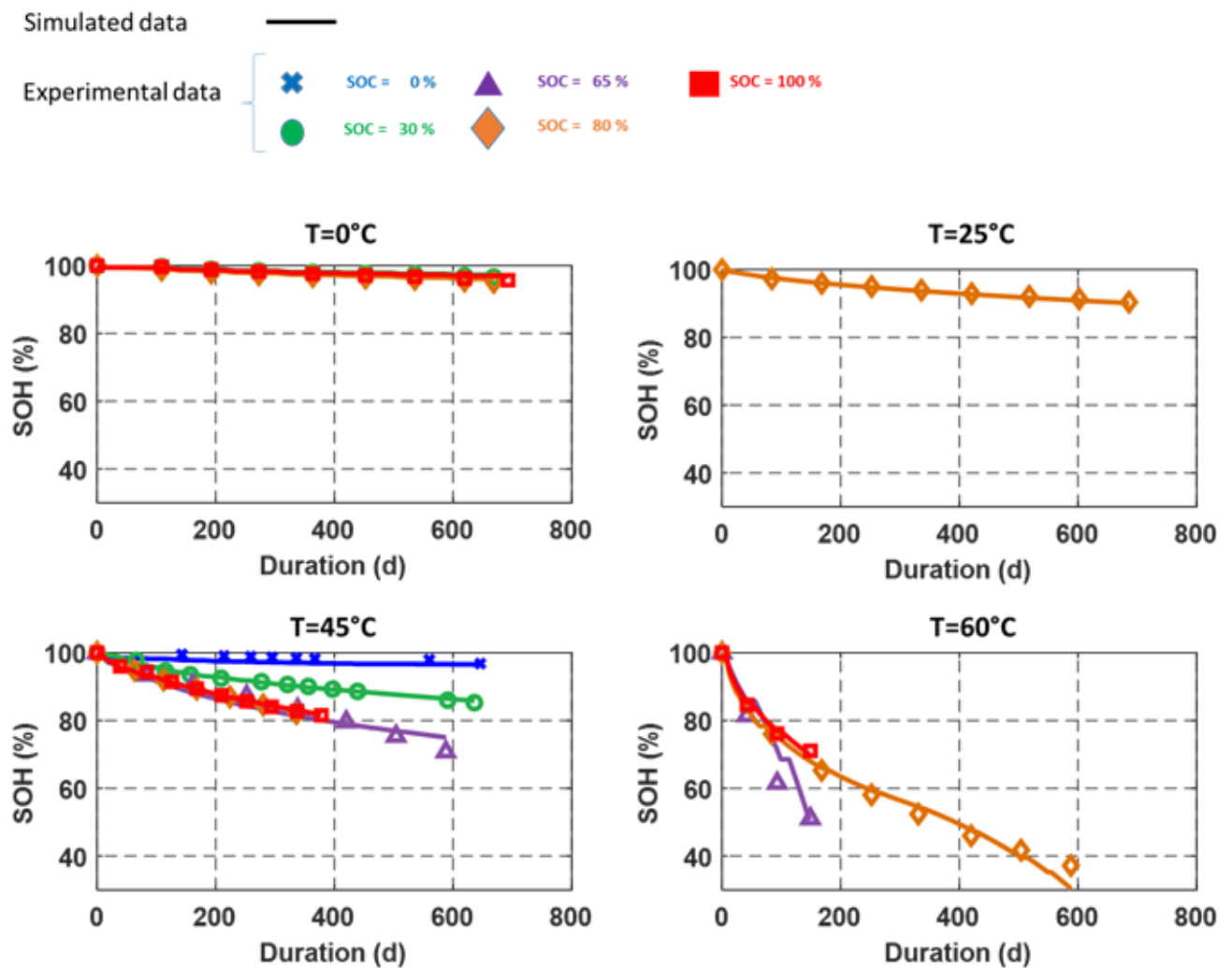


FIGURE III- 6: COMPARISON BETWEEN EXPERIMENTAL CELL SOH AND SIMULATED SOH FROM THE ONE-TANK AGING MODEL

### III.2.2.3. One-tank aging model error

The error between the cell SOH simulated from the one-tank aging model and experimental data is illustrated in FIGURE III- 7. At BOL, the error is not zero as the FIGURE III- 6 represents the SOH evolution starting from the first periodical check-up when the cell capacity has slightly decreased. It is important to notice that the one-tank aging model gives some very good results in terms of cell SOH prediction. The cell aging is slightly underestimated at low temperature (0°C), but the model reaches a maximum error of 1.2% after almost 800 days (2.1 years) of storage for the calendar condition at SOC 100%.

At ambient temperature, 25°C, the results are also very good with an error of less than 0.5%. The results are very satisfactory at 45°C with the maximum error of 2% except for the calendar condition at 65% where the cell aging is overestimated at the cell EOD (error less than 5%).

At 60°C the model gives a low error especially at SOC 80% and 100% however, at SOC 65%, the model underestimates the cell SOH aging with a maximum error of 10%.

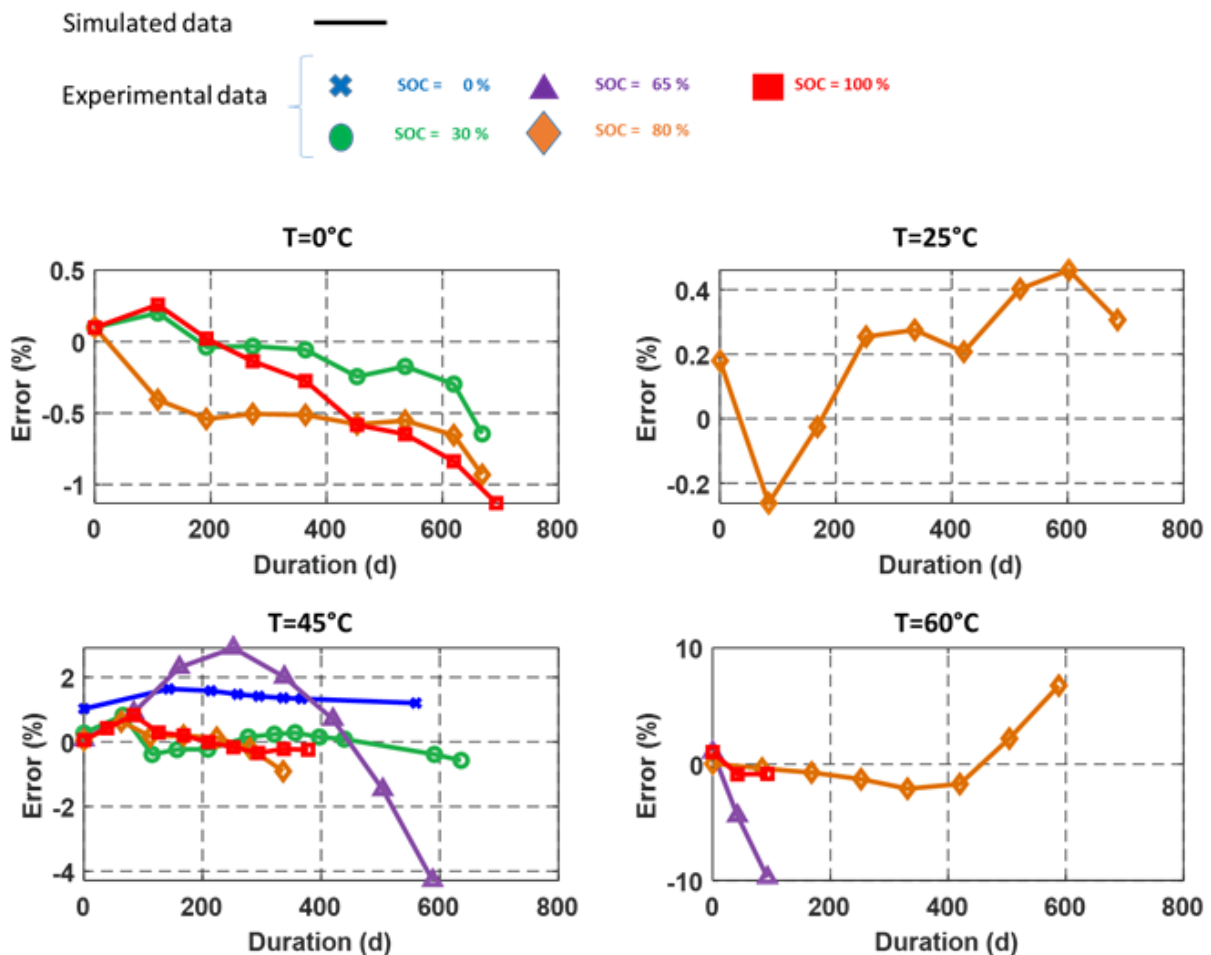


FIGURE III- 7: ERROR BETWEEN EXPERIMENTAL AND SIMULATED CELL SOH FROM THE ONE-TANK AGING MODEL

### III.2.3. Validation of the one-tank aging model

To validate the model aging, we used the same calendar conditions mentioned in the section for the MOBICUS aging model validation: the calendar condition at 45°C and variable SOC (between SOC 30%-80%) and the two thermal cycling conditions at SOC 65% and 100%. The comparison between the simulated cell capacity from the one-tank aging model and the experimental data is illustrated in **FIGURE III- 8**.

The one-tank aging model gives a good correspondence with the experimental data for the variable SOC condition at 45°C. After 600 days, the model slightly underestimates the cell SOH aging. The error between experimental and simulated values is less than 4%.

For the cycling thermal condition at SOC 65%, the model matches the experimental values of the cell SOH at the cell BOL (before 200 days) and EOL (after 600 days) as shown in **FIGURE III- 8**. The model can identify the activation energy at those state-of-charges, which explains why we have a good agreement between the simulated and experimental data at 60°C and 30% of SOC. Between 200 days and 600 days (1.6 years), there is an improvement of the cell SOH prediction with a maximum error reached of 15%. The thermal cycling condition at 100% of SOC is also well predicted by the model with, the error reached on the cell SOH estimation below 4%.

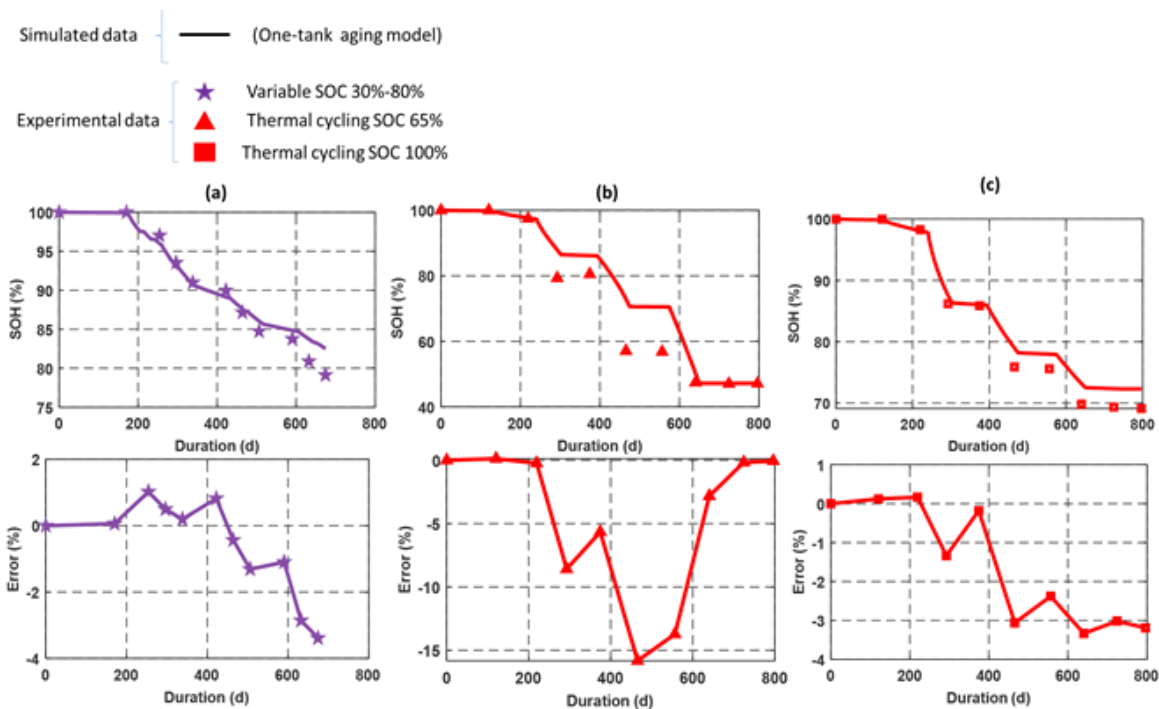


**FIGURE III- 8: VALIDATION OF THE ONE-TANK AGING MODEL FOR (A) THE VARIABLE SOC AT 45°C, (B) THERMAL CYCLING AT 65% OF SOC AND (C) 100% OF SOC.**

### III.3. Comparison of the MOBICUS aging model prediction versus One- tank aging model

As described previously, the identification process of the MOBICUS and the one-tank aging model parameters predict the simulated cell SOH with low error values at the temperatures below 60°C and above 60°C for SOC 80% and 100%. At high temperatures (at 45°C and 60°C), it is suspected that the resting SOC is an important factor responsible for cell degradation. The one-tank aging model adds a new feature from the MOBICUS aging model by coupling the temperature and state-of-charge effect to try to improve the aging prediction. The one-tank aging model seems slightly more accurate than the MOBICUS aging model however, the main difference between the two models is at 60°C and SOC 65% when the model is not able to give a satisfactory result. The maximum error for the MOBICUS and one-tank aging model at this condition are respectively 20% and 10%.

The validation process, which simulates the cell SOH for the thermal cycling at 100% of SOC, is good and similar for both models but at SOC 65%, the MOBICUS aging model is farther from the experimental data compared to the one-tank aging model. The maximum error found for the MOBICUS aging model and one-tank aging model are respectively 30% and 15%.

In this chapter, a comparison between the MOBICUS and one-tank aging model at 60°C and 65% of SOC (identification process) and thermal cycling condition at SOC 65% of SOC (validation process) is done to analyze how the influence of the SOC is improved.

#### III.3.1. Identification process at 60°C and 65% of SOC

The comparison of the experimental cell SOH at 60°C and 65% of SOC versus the simulated cell SOH respectively from the MOBICUS aging model and the one-tank aging model are illustrated in [FIGURE III- 9\(a\)](#) and [FIGURE III- 9\(b\)](#).

The MOBICUS aging model is not able to predict the cell SOH until the cell EOL, as illustrated in [FIGURE III- 9\(a\)](#). The correspondence with the experimental data stopped at SOH <70% when using the MOBICUS aging model. For this calendar condition, the temperature is fixed at 45°C but there is a SOC deviation on the SOC profile used (illustrated in chapter 2, §. II.3). This deviation goes from 65% at the BOL to 30% at the cell EOL. The MOBICUS aging model does not simulate the SOH fading when the SOC<50% on the SOC profile. At 60°C, the degradation rate  $J_{cal}(T, SOC)$  of the MOBICUS aging model is mostly dependent on  $J_{cal_{ref}}$  (0.122Ah/days), the SOC accelerating factor  $Fa_{SOC}$  (varying from 0 to 1) and the temperature accelerating factor  $Fa_T$  (depending on the activation energy). If the activation is fixed for this temperature 60°C (thus  $Fa_T$  fixed) only  $Fa_{SOC}$  is able to take into account, the SOC variation on the degradation rate. As the MOBICUS aging model does not simulate the SOH<70%, it means that the factor  $Fa_{SOC}$  is not enough to correctly adjust the capacity degradation rate at 60°C.

The fact that the one-tank aging model can couple the influence of the SOC on the activation energy allows to improve the slope of the cell SOH degradation at high temperature as shown in [FIGURE III- 9\(b\)](#).. As the activation energy  $E_{a_{T \geq T_{ref}}}(SOC)$  is identified at 65% and 30% at 60°C,

the one-tank aging model simulate more accurately the cell SOH evolution when the resting SOC is between 30 and 65%.

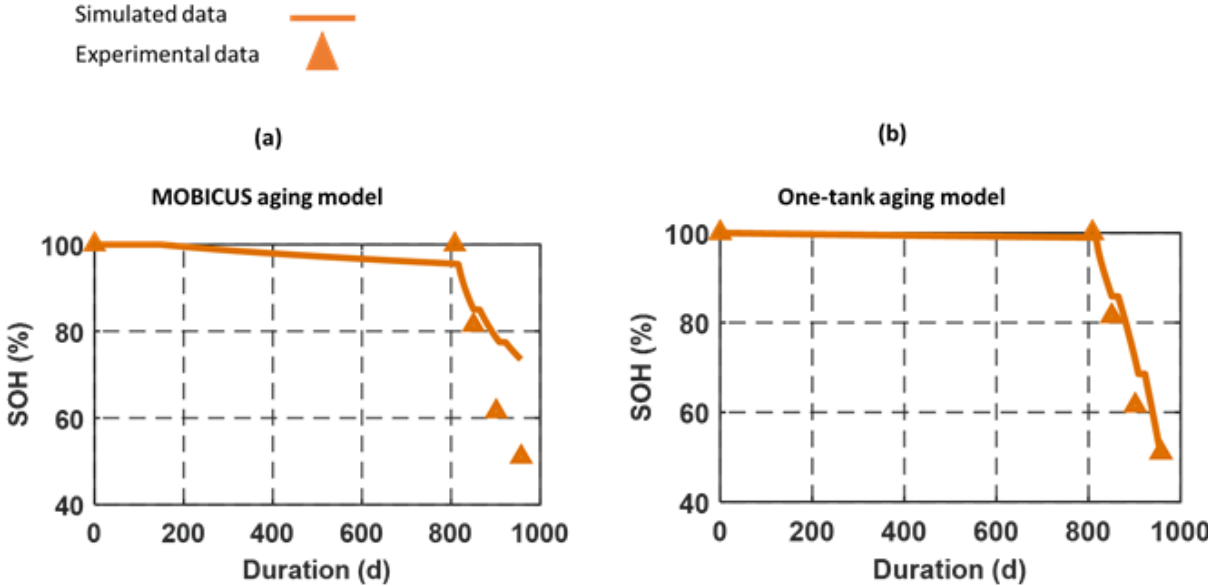


FIGURE III- 9: IDENTIFICATION AT T=60°C, SOC=65% BETWEEN EXPERIMENTAL AND SIMULATED CELL SOH WITH THE MOBICUS(A) AND ONE-TANK(B) AGING MODEL

III.3.2. Validation process for the thermal cycling condition at SOC 65%

The thermal cycling at 65% of SOC is used for the validation of the MOBICUS and one-tank aging model. The comparison of the simulated cell SOH versus the experimental data is illustrated in FIGURE III- 10(a) using the MOBICUS aging model and FIGURE III- 10(b) the one-tank aging model. The three phases in FIGURE III- 10(b) correspond to the range where the one-tank aging model correctly predicts the cell SOH (phase 1 and 3) and when the simulation is less accurate (phase 2). Those three phases are reported in the same range in FIGURE III- 10 (a) for the MOBICUS aging model.

As seen with the simulation in FIGURE III- 10 (a), the MOBICUS aging model is not able to reach the first experimental data of phases 2 and 3 when the cycling between 30°C- 60°C. This lack of precision may be related to the identification process of the MOBICUS aging model, which shows that the results are not satisfactory at 60°C and 65% of SOC. It has been noticed, during the identification process described previously in FIGURE III- 9(a), a SOC drift through aging for the SOC profile at 60°C and 65% of SOC. The same observation is made for the SOC profile of the thermal cycling at SOC 65% indicating that the battery reaches the SOC 30% at the cell EOL (illustrated in chapter 2, §. II.3.1.2). Because the MOBICUS aging model is not able to predict correctly the cell aging at 60°C for SOC below 50% during the identification process, the cell SOH is underestimated for the aging model validation.

Unlike the MOBICUS aging model, the one-tank aging model predicts very well the cell aging at the cell BOL during phase 1 and 3 as illustrated in FIGURE III- 10 (b):

During the whole phase 1 and 3, the cell is stored respectively at 65% and 30%. The cycling is performed between 0°C- 30°C. As the identification process using the one-tank aging model correctly optimize the activation energy  $E_{aT}(SOC)$  at these two SOC levels for  $< T_{ref}$ , the simulation can predict cell aging.

The beginning and end of phase 2 correspond to a calendar condition at 60°C and SOC respectively at 65% and 30%. The identification process optimizes the  $E_{aT}(SOC)$  at these two SOC levels for  $> T_{ref}$ , the simulation is then able to predict the cell aging at the beginning and end of phase 2. However, during phase 2, the one-tank model does not fully estimate the right amount of capacity degradation when the cycling between 30°C-60°C. The cell is stored at SOC between 30%-65% during phase 2. Note that the calculation of the activation energy when  $T < T_{ref}$  is done using a linear interpolation method due to lack of experimental data when  $T < T_{ref}$  and SOC 65%. This interpolation could possibly increase the error as the activation energy during phase 2 when the cycling is performed between 30°C-60°C.

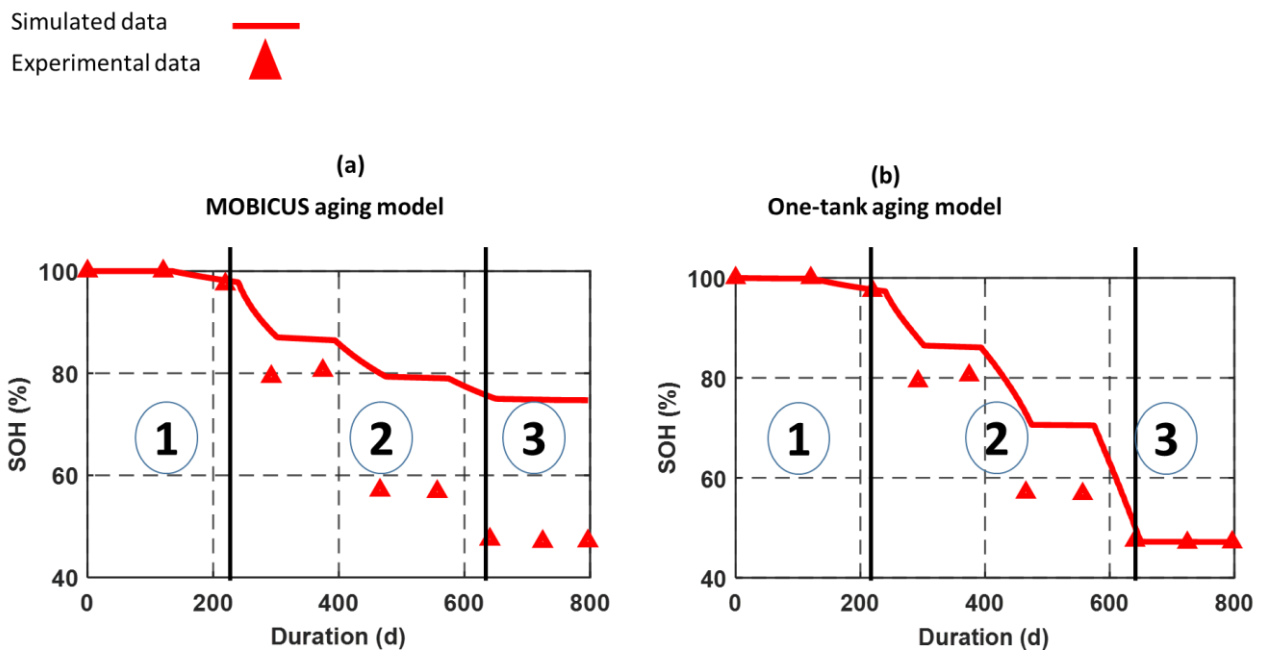


FIGURE III- 10: VALIDATION OF THE THERMAL CYCLING AT SOC=65%, BETWEEN EXPERIMENTAL AND SIMULATED CELL SOH, WITH THE MOBICUS(A) AND ONE-TANK(B) AGING MODEL

## Conclusion

The one-tank aging model developed in this chapter was compared to the MOBICUS aging model. The difference between the two aging models is the capability of the one-tank aging model to consider the coupling effect between SOC and temperature. In fact, this coupling effect was not noticed during the MOBICUS project due to the lack of experimental SOH measurements at temperature 60°C, SOC (65% and 100%).

The identification and validation of the two aging models showed some close results except for the aging conditions at temperature 60°C, SOC 65% (used for the identification process) and variable temperature, SOC 65% (used for the validation process). Due to lack of experimental data, the MOBICUS aging was not able to estimate the cell capacity at high temperature for the SOCs below 50%, inevitably leading to poorer results compared to the one-tank aging model. In addition, at a temperature below 45°C the activation energy was calculated by interpolation method at 65% of SOC. This interpolation method could underestimate the temperature accelerating factor of the aging laws. This could explain why the validation process was not completely satisfactory for either MOBICUS or one-tank aging models when cycling between 30°C-60°C.

## CHAPTER 4: STUDY OF A COUPLING BETWEEN A DUAL-TANK OCV MODEL AND CALENDAR EMPIRICAL AGING MODEL

## Introduction

The one-tank aging model presented in the previous chapter was used for the prognosis of the cell capacity (SOH). With this kind of model, the update of the Open-Circuit Voltage (OCV) curve shape along with aging is performed by horizontally shrinking the OCV or using a look-up table function of the SOC and SOH. Nevertheless, a single semi-empirical aging model, giving one value of cell SOH, is not enough to correctly update the cell (OCV) curve using these methods. The dual-tank OCV model, considering the degradation path of the battery, offers the possibility to account for different internal states of health for both the electrodes of the battery cell. By tracking these internal states of health with aging, it gives the opportunity to correctly modify the cell OCV function of the capacity, which may evolve in various ways. Therefore, using a dual-tank OCV model may be more relevant for the prognosis of the cell capacity. In this chapter, the dual-tank model approach is firstly detailed in §.1. Secondly, the coupling of a semi-empirical aging model with a dual-tank OCV model is studied in §.2. Then, complete model simulations are performed in specific cases to evaluate the potentialities of the dual-tank aging model approach in §.3.

### IV.1. Dual-tank OCV model

#### IV.1.1. Model presentation

Electrochemical tests are performed on coin cells made via harvested electrode by applying a galvanostatic charge and discharge current at C/10 rate. These tests allow characterizing the galvanostatic signals of the positive and negative electrode potentials ( $V_{pos\theta}$ ,  $V_{neg\theta}$ ) versus the reachable lithium content ( $\theta_{pos}$ ,  $\theta_{neg}$ ) of each electrode ranging, by definition, from 0 to 1. The Open-Circuit Potential (OCP) signal of each electrode is then achieved by averaging the charge and discharge galvanostatic signals measured from the coin cells as presented in chapter 2 of this thesis report (FIGURE II- 2). The averaged signals of the positive and negative electrodes versus lithium content are shown in FIGURE IV- 1(a). By considering the electrodes capacities ( $C_{pos}$ ,  $C_{neg}$ ), it is possible to scale up the electrode potential signals at the cell level ( $V_{posAh}$ ,  $V_{negAh}$ ) as illustrated in FIGURE IV- 1(b).

To build the open-circuit voltage signal, we can then introduce the offset parameter ( $OFS$ ) which shifts the negative electrode potential signal  $V_{negAh}$  to the left, which is now represented by  $V_{negAh-OFS}$ , as shown in FIGURE IV- 1(c). These electrodes potential signals ( $V_{posAh}$ ,  $V_{negAh-OFS}$ ) are superimposed versus the cumulative capacity to calculate the open-circuit voltage by subtracting the positive to the negative electrode potential signals.

Setting the voltage limits ( $U_{min}$ ,  $U_{max}$ ) allows calculating the useable open-circuit voltage signal ( $OCV$ ) and capacity ( $Q_{OCV}$ ) as well as the minimum and maximum electrodes potential limit ( $V_{pos_{min}}$ ,  $V_{pos_{max}}$ ,  $V_{neg_{min}}$ ,  $V_{neg_{max}}$ ) shown in FIGURE IV- 1(c). The voltages ( $U_{min}$ ,  $U_{max}$ ) are the charge and discharge nominal voltages indicated by the cell manufacturer. The OCV is defined such as:

$$U_{min} \leq OCV \leq U_{max} \quad 4.1$$

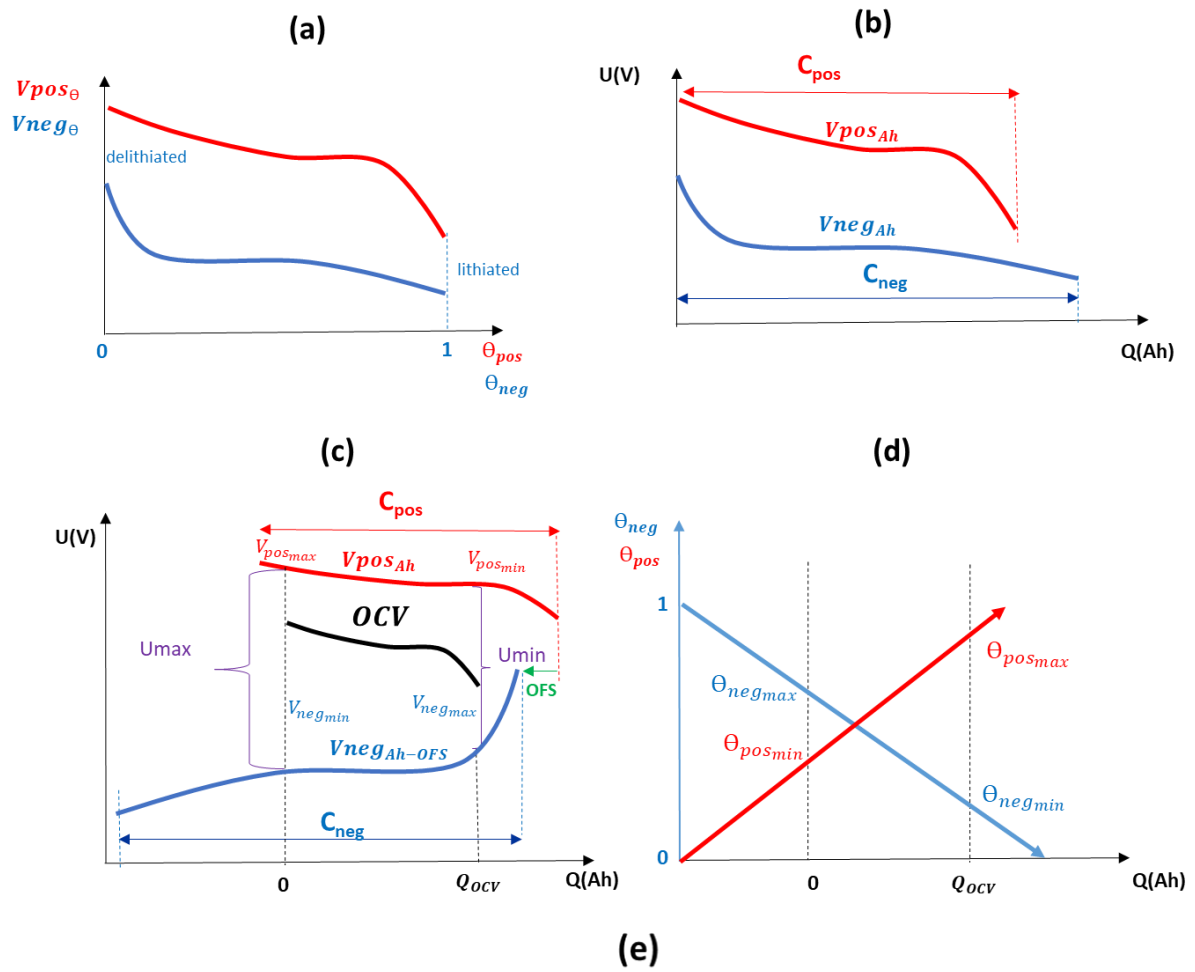


FIGURE IV- 1 SIMULATION OF CELL CAPACITY WITH THE DUAL-TANK OCV MODEL: (A) OCP'S VERSUS LITHIUM CONTENT, (B) OCP'S VERSUS CAPACITY, (C) CELL OCV VERSUS CAPACITY, (D) MINIMUM AND MAXIMUM ELECTRODES LITHIUM CONTENT, (E) DUAL-TANK OCV MODEL.

The dual-tank OCV model enables also to determine the reachable lithium content of each electrode at 0% and 100% of cell state-of-charge (minimum and maximum values of the OCV). At SOC 100%, the positive electrode reaches its minimum lithium content value  $\theta_{pos\_min}$  while the negative electrode reaches its maximum lithium content value  $\theta_{neg\_max}$  which are shown in FIGURE IV- 1(d). At this state, the electrode potential signals are linked by the maximum cell limit:

$$U_{max} = V_{pos_{Ah}}(\theta_{pos\_min}) - V_{neg_{Ah-OFS}}(\theta_{neg\_max}) \quad 4.2$$

At 0% of SOC when the cell is fully discharged, the positive electrode reaches its maximum value  $\theta_{pos\_max}$  while the negative electrode reaches its minimum value  $\theta_{neg\_min}$  (FIGURE IV- 1(d)). The minimum voltage threshold links both electrodes potential at this state:

$$U_{min} = V_{pos_{Ah}}(\theta_{pos\_max}) - V_{neg_{Ah-OFS}}(\theta_{neg\_min}) \quad 4.3$$

For sake of simplicity, the positive and negative electrode signal ( $V_{pos_{Ah}}, V_{neg_{Ah-OFS}}$ ) in FIGURE IV- 1(c) are noted ( $V_{pos}, V_{neg}$ ) above. To sum up, using the electrode potential signals characterized from coin cells and voltage limits of a li-ion cell, the dual tank OCV model is able to simulate the OCV and cell capacity as well as the maximum and minimum electrodes lithium content with three inputs parameters: ( $C_{pos}, C_{neg}, OFS$ ), as illustrated in FIGURE IV- 1(e). The  $OFS$  parameter increases when the negative potential curve shifts to the left while ( $C_{pos}, C_{neg}$ ) when the battery aged.

#### IV.1.2. Parameter's identification of the dual-tank model

##### IV.1.2.1. Identification method

The three dual-tank OCV model parameters,  $C_{pos}, C_{neg}$  and  $OFS$ , are identified at each check-up during aging tests. To do so, an optimization method is applied to find the optimal set of parameters. This optimal solution is found by minimizing the root mean square error (RMSE) between the simulated cell voltage signal and experimental open-circuit voltage signal. The voltage threshold ( $U_{min}, U_{max}$ ) correspond to the maximum and minimum experimental open-circuit voltage. The open-circuit voltage signal (OCV) corresponds to the average of the charge and discharge voltage signals measured on the cell at a C/10 rate. In this way, we will not consider the cell polarization resistance.

An example of optimization results, obtained for each aging state during the calendar condition test (T=45°C, SOC = 65%), is shown FIGURE IV- 2. The optimization results of the cell OCV signal simulated by the dual-tank OCV model are represented in solid line and the experimental OCV signals for each check-up are represented in dashed line.

This method is applied for all aging conditions to analyze the evolution of the dual-tank OCV model parameters with cell SOH.

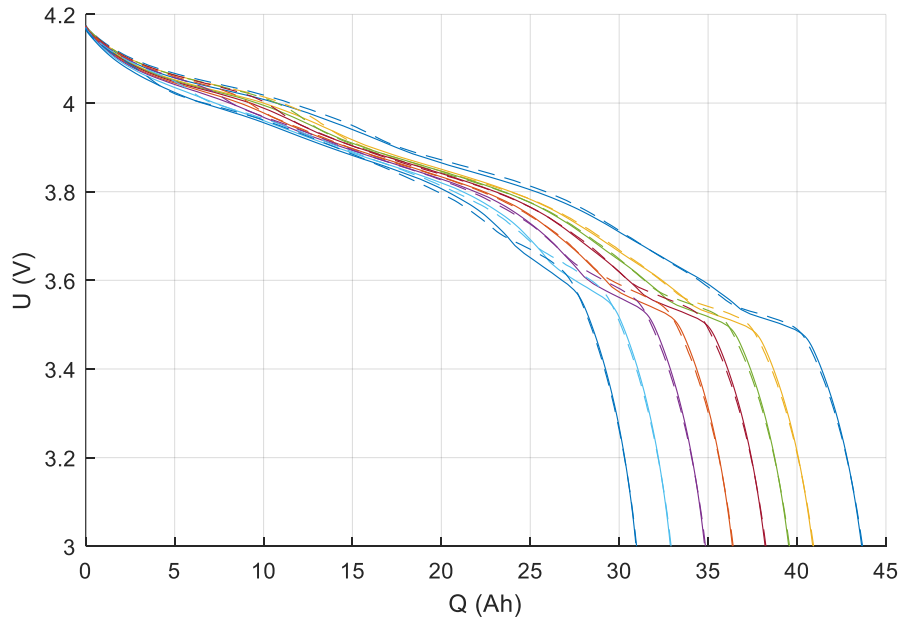


FIGURE IV- 2: COMPARISON BETWEEN SIMULATED AND EXPERIMENTAL CELL VOLTAGE AT  $T=45^{\circ}\text{C}$  AND  $\text{SOC}=65\%$ .

#### IV.1.2.2. Dual-tank parameters evolution with aging

In this part, the evolution of the three parameters  $C_{pos}$ ,  $C_{neg}$ ,  $OFS$ , identified during the cell aging are illustrated. Each point corresponds to the periodical characterization of the full cell. All the parameters are represented at four temperatures, namely  $0^{\circ}\text{C}$ ,  $25^{\circ}\text{C}$ ,  $45^{\circ}\text{C}$ , and  $60^{\circ}\text{C}$ , and five state-of-charges, namely 0%, 30%, 65%, 80%, and 100%.

##### IV.1.2.2.1 Positive electrode

The evolution of the positive electrode capacity during aging is illustrated in [FIGURE IV- 3](#):

- At  $0^{\circ}\text{C}$ , the overall degradation is barely noticeable compared to warmer temperature results, with the highest degradation associated to SOC 80% where the positive capacity decreases from 48 Ah to  $\sim 46.5$  Ah within 700 days. At this temperature, the active mass loss at the positive electrode can be neglected.
- At  $25^{\circ}\text{C}$ , the active mass loss at the positive electrode is slightly more important. For the corresponding 80% of SOC, the positive capacity reaches  $\sim 44.5$  Ah within 700 days, which corresponds to a loss of 7% of the initial positive electrode capacity.
- The degradation rate of the positive electrode capacity is higher at  $45^{\circ}\text{C}$ . The identification is made for five state-of-charge namely 0%, 30%, 65%, 80% and 100%. The most important degradation is attributed to SOC 65% condition with almost 20% of capacity loss within 700 days. Comparing to SOC 100% condition, the active mass loss is more important at SOC 65% and 80%.
- At  $60^{\circ}\text{C}$ , the active mass loss at the positive electrode is more noticeable at SOC 65% comparing to SOC 80% and 100% as observed at  $45^{\circ}\text{C}$ . In fact, the positive electrode capacity loses almost 35% of its capacity at SOC 65% in less than 200 days.

To sum up, the degradation of the positive electrode is barely noticeable at low temperatures ( $0^{\circ}\text{C}$  and  $25^{\circ}\text{C}$ ). At high temperatures ( $45^{\circ}\text{C}$  and  $60^{\circ}\text{C}$ ), the positive electrode capacity falls rapidly, especially at SOC 65%.

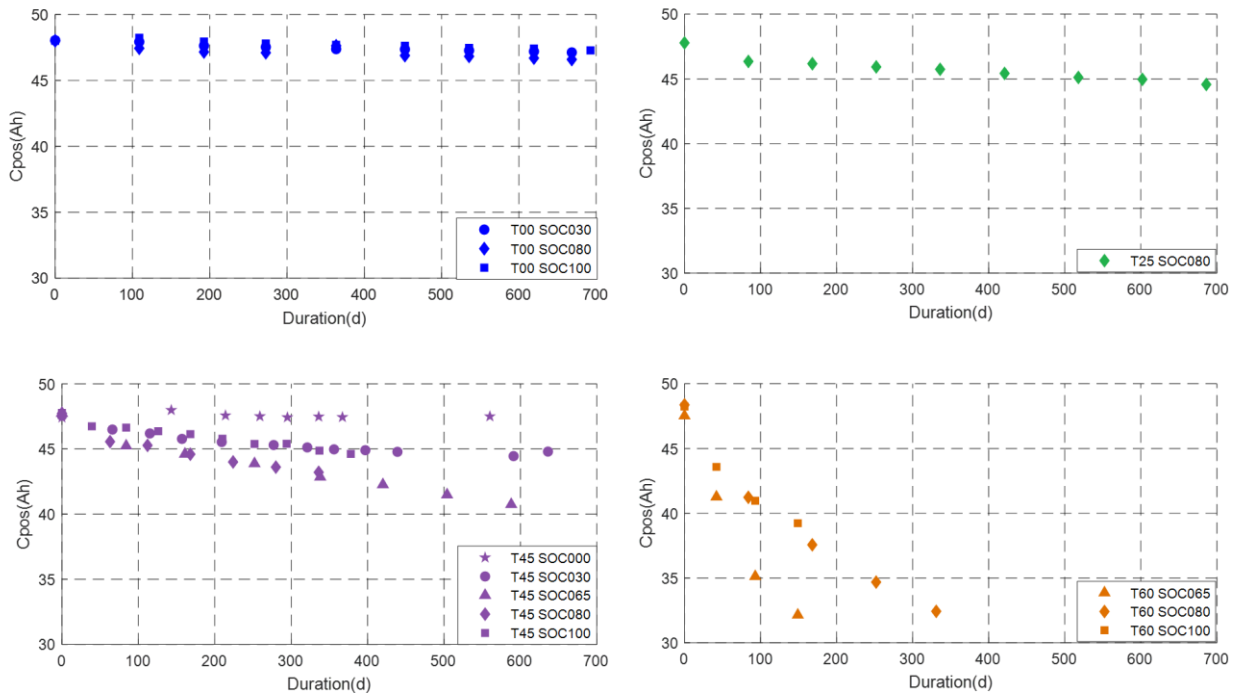


FIGURE IV- 3: ELECTRODE POSITIVE CAPACITY IDENTIFIED AFTER 700 DAYS OF CELL AGING.

#### IV.1.2.2.2 Negative electrode

The evolution of the negative electrode capacity during aging is illustrated in **FIGURE IV- 4**:

- At 0°C, the negative electrode capacity fade is very low. A resting SOC at 100% seems to have more influence than 30% and 80% of SOC. At SOC 100%, the negative electrode capacity decreases from 49 Ah to approximately 47.3h (3.4% of loss).
- A resting temperature of 25°C does not really affect the negative electrode capacity at 80% of SOC, which reaches 47.5 Ah within 700 days corresponding to an active mass loss of 3% of its initial value.
- It is noticed previously that the positive electrode capacity is more affected at 65% of SOC at temperature 45°C. For the negative electrode capacity, the SOC 100% condition seems to be the most degradative. The negative electrode capacity decreases from 48.5 Ah to almost 45.5 Ah within 400 days, corresponding to a total loss of 6%. This active mass loss at the negative electrode is a bit higher than the positive electrode at 45°C.
- The influence of high temperature is highlighted at 60°C especially at 65% compared to the SOC 80% and 100%. The negative electrode encounters a total loss of approximately 8% within 200 days.

To sum up, the degradation of the negative electrode capacity degradation is low at low temperatures (0°C and 25°C). The most damaging calendar condition is at temperature 60°C and SOC 65%, which is the case as well for the positive electrode. However, at 45°C, the negative electrode loses more capacity at SOC 100% (unlike the positive electrode which is at SOC 65%).

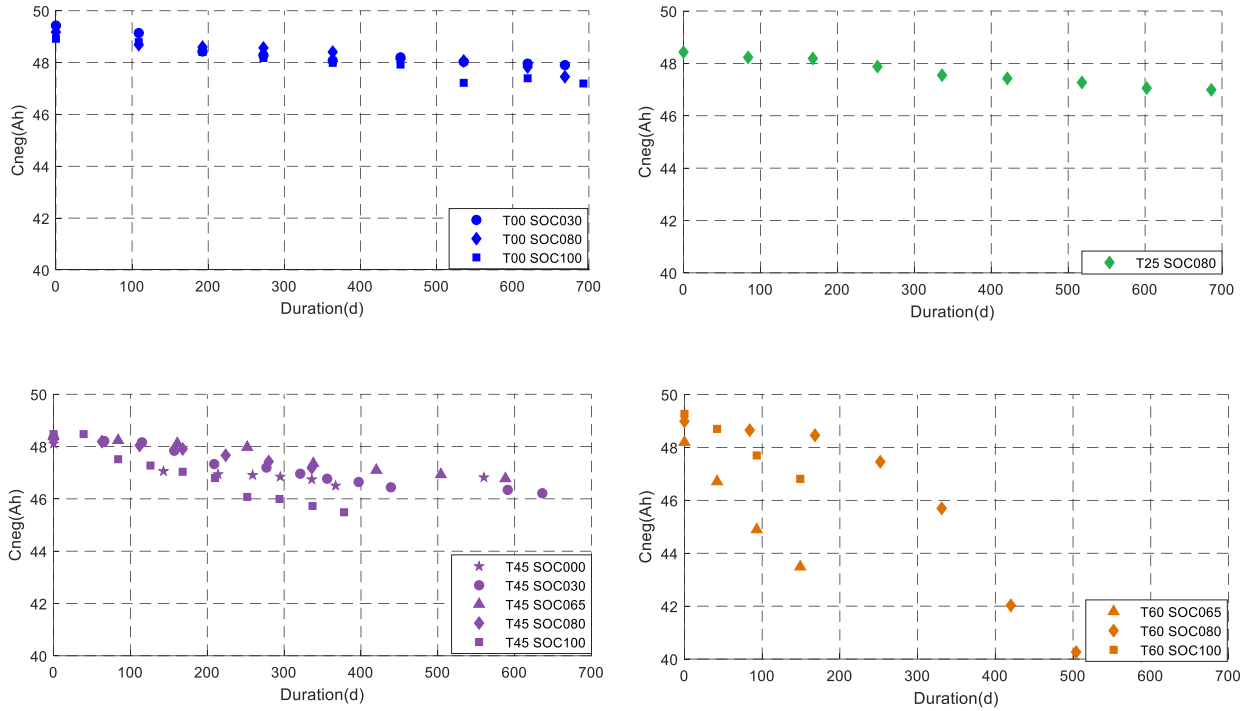


FIGURE IV- 4: NEGATIVE ELECTRODE CAPACITY IDENTIFIED AFTER 700 DAYS OF CELL AGING.

#### IV.1.2.2.3 Offset

The evolution of the offset parameter identified for different calendar aging conditions is illustrated in FIGURE IV- 5:

- At 0°C, the offset evolves slightly more rapidly at SOC 100% compared to the SOC 80% and 30%.
- At 25°C, the ambient temperature at 80% SOC leads to a small evolution of the offset parameter of  $\approx 2\text{Ah}$  (almost 50% of gain) within 750 days.
- The acceleration at 45°C is clearly more important compared to 0°C and 25°C. During The identification results from the positive and negative electrode capacities (FIGURE IV- 3 and FIGURE IV- 4), we have noticed that there is not a continuous evolution of those parameters with SOC. However, for the offset parameter, we can notice that there is a monotonic effect of SOC. The higher the resting SOC is, the faster the acceleration rate of the offset parameter will be.
- At 60°C, the offset parameter follows the same trend as the positive and negative capacities with a rapid evolution at SOC 65% and 100%. At 100% of SOC, the aging model predicts the offset to reach  $\approx 9.5\text{Ah}$  (almost 70% of offset gain) within 150 days.

To sum up, the offset barely increases at temperature 0°C and 25°C. At 45°C, the offset acceleration rate is fastest at SOC 100% as observed for the negative electrode capacity. The offset has a monotonous evolution with the increase of storage SOC. At 60°C, it can be noticed that the most damaging condition is at SOC 65%, just like the positive and negative electrode.

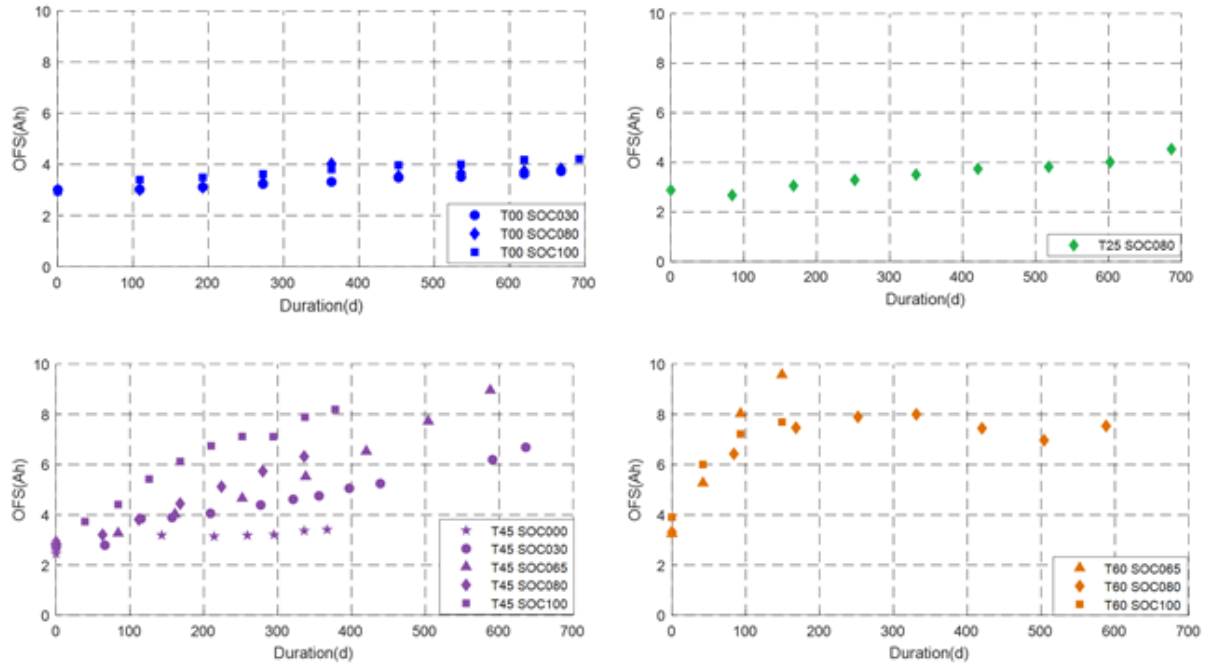


FIGURE IV- 5: OFFSET IDENTIFIED AFTER 700 DAYS OF CALENDAR AGING.

#### IV.1.2.3. Validation from the literature

##### IV.1.2.3.1 Influence of the SOC

As mentioned in the literature review (chapter 1, §. I.3.2.1), part of the offset aging is influenced by the lithium loss inventory (LLI). High SOC's accelerate the SEI growth at the interface between the negative electrode and the electrolyte, leading to an increase of lithium loss inventory [75]. Therefore, this acceleration of *OFFS* parameter at high SOC is consistent with what we observed in the literature because of LLI.

The §. 1.2.2 shows that the electrode capacities aging, associated with active mass loss in chapter 1 (§. I.3.2.1) is increased at high SOC. In the literature, some studies show that gas formation in the electrode surface leads to active mass loss. Gas can be generated at high potential ( $CO_2$ ,  $O_2$ ) on the positive electrode ([2]-[3]) due to oxidation of the electrolyte at the positive electrode. However, according to Barbara Michalak et al. [78], the gas formation can appear at both electrodes when considering graphite or LMO materials. Gaseous species, associated with decomposition of the electrolyte on the negative electrode, are often generated during the first charge cycles of cell formation but also, to a lesser extent, due to cell aging [9]. Pillipili Matadi et al. [71] identified the influence of polymerization of biphenyl (an additive contained in the electrolyte) which leads to gas formation at 45°C and 60°C for 100% of SOC. Dry areas due to a gas formation may appear at high SOC, and high temperature, advantaging proportional ( $C_{pos}$ ,  $C_{neg}$ ) decrease. Another hypothesis evoked in the literature might be the dissolution of the manganese when working with LMO material [16], which can contaminate the negative electrode. This could explain the fast degradation of the positive electrode possibly accentuated at SOC 65%.

#### IV.1.2.3.2 Influence of the temperature

According to Broussely et al. [79], the expansion of SEI in calendar aging leads to more consumption of Li-ions at the high temperature inside the cell thus increase of *OFS* during aging.

Z. Mao et al. [80], who studies the calendar aging on a 15 Ah Graphite/NMC-LMO pouch cell, observes the deterioration of electrode materials and attributed it to electrode dry-out due to gas formation. The authors identify nearly 30% of electrode active material losses due to gas formation. This observation is especially noticeable at high temperatures, which accelerate the degradation of  $C_{pos}$  and  $C_{neg}$  as shown in §. 1.2.2.

#### IV.1.2.4. Influence of the degradation path

To analyze the influence of the degradation path on the dual-tank OCV model parameters, the evolutions of  $C_{pos}$ ,  $C_{neg}$ , *OFS* versus the cell SOH are illustrated in **FIGURE IV-6**.

First, the three parameters evolve with a different amplitude:

- The positive capacity follows the same degradation path at temperature 0°C, 25°C and 60°C. At temperature 45°C and SOC 100%, the positive electrode capacity slightly gets away from the overall degradation path.
- The capacity of the negative electrode evolves differently depending on the calendar condition. The degradation path is strictly different for all calendar aging conditions. This is especially noticeable at 45°C and above all at 60°C.
- The offset has also a degradation path with a wide amplitude.

Those phenomena on the negative electrode and the offset might be related to the fact that aging mechanisms are more complex at 60°C, leading to various ways of aging.

The second aspect that is pointed out in **FIGURE IV-6**, is the complexity to define the cell SOH. Using a one-tank model allows to quantify the cell SOH by a unique criterion with is the cell capacity. Using a dual-tank model helps to correlate the cell SOH by a triplet of three parameters ( $C_{pos}$ ,  $C_{neg}$ , *OFS*) which evolve differently depending on the calendar condition.

For this reason, the choice to build an aging model for each parameter of the dual-tank OCV model may be useful to describe more precisely an aging state and, probably, predict more precisely the cell SOH.

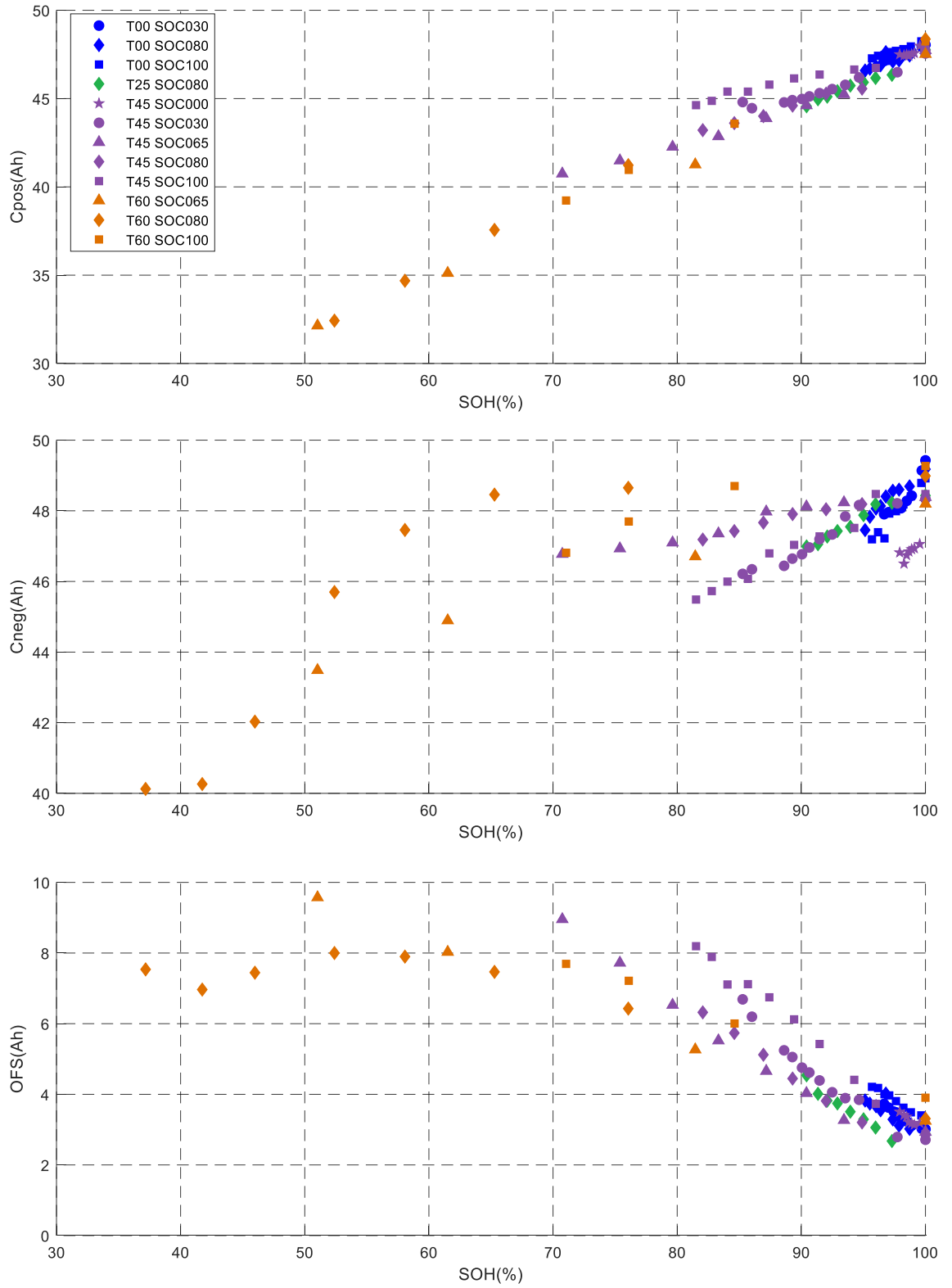


FIGURE IV- 6: EVOLUTION OF THE DUAL-TANK OCV MODEL PARAMETERS VERSUS CELL SOH.

## IV.2. Dual-tank aging model

This section aims to traduce mathematically the evolution of the dual-tank model parameters ( $C_{pos}$ ,  $C_{neg}$ ,  $OFS$ ) with aging. Hence, by definition, they will be considered as variables in the following section.

### IV.2.1. Dual-tank aging model equations

The same exact equations of the one-tank aging model (see chapter 3, §. III.2.1) are used to define the dual-tank OCV model.

The dual-tank aging laws are displayed below:

$$\frac{dOFS}{dt} = \frac{J_{cal_{OFS}}(T, SOC)}{1 + A_{OFS}OFS} \quad 4.4$$

$$\frac{dC_{pos}}{dt} = \frac{J_{cal_{C_{pos}}}(T, SOC)}{1 + A_{C_{pos}}C_{pos}} \quad 4.5$$

$$\frac{dC_{neg}}{dt} = \frac{J_{cal_{C_{neg}}}(T, SOC)}{1 + A_{C_{neg}}C_{neg}} \quad 4.6$$

Where  $J_{cal_{C_{pos}}}$ ,  $J_{cal_{C_{neg}}}$  and  $J_{cal_{OFS}}$  refer to the degradation rates of the positive and negative electrodes during calendar aging. The degradation rate equations, which are dependent on the temperature and SOC accelerating factors, are also detailed in chapter 3 (§. III.2.1).

### IV.2.2. Parameters identification

The identification process consists of identifying  $J_{cal}$  for each dual-tank aging model.  $J_{cal}$  depends on the acceleration factors ( $Fa_T$ ,  $Fa_{SOC}$ ) and the parameter  $J_{cal_{ref}}$ . For all conditions, we also identify the nominal parameter ( $C_{pos_{init}}$ ,  $C_{neg_{init}}$ ,  $OFS_{init}$ ). The method detailed in chapter 3 (§. III.2.2.1) is strictly the same (optimization process to find the dual-tank aging model parameters). The parameter A is also optimized. All the results are presented [TABLE IV- 1](#). The temperature and SOC accelerating are illustrated later (in [FIGURE IV- 8](#), [FIGURE IV- 10](#) and [FIGURE IV- 12](#)). The degradation rate  $J_{cal}$  for each dual-tank aging, model is illustrated in Annex 1.

	Unit	$C_{pos}$	$C_{neg}$	$OFS$
Initial value	Ah	48.50	49.53	2.4
$J_{cal_{ref}}$	Ah/days	0.107	0.105	0.17
$Ea_{T < T_{ref}}(SOC = 30\%)$	kJ.mol <sup>-1</sup>	58.9	57.5	43.6
$Ea_{T < T_{ref}}(SOC = 80\%)$	kJ.mol <sup>-1</sup>	48.7	26.2	82.5
$Ea_{T < T_{ref}}(SOC = 100\%)$	kJ.mol <sup>-1</sup>	71.8	34.8	75.1
$Ea_{T \geq T_{ref}}(SOC = 30\%)$	kJ.mol <sup>-1</sup>	282.3	205.4	251.4
$Ea_{T \geq T_{ref}}(SOC = 65\%)$	kJ.mol <sup>-1</sup>	118.2	140.1	10
$Ea_{T \geq T_{ref}}(SOC = 80\%)$	kJ.mol <sup>-1</sup>	115.3	104.4	82.4
$Ea_{T \geq T_{ref}}(SOC = 100\%)$	kJ.mol <sup>-1</sup>	158.7	228.5	48.8
$Fa_{SOC}(SOC = 0\%)$	w.u.	2.7e-3	0.47	3e-14
$Fa_{SOC}(SOC = 30\%)$	w.u.	0.98	0.51	0.28
$Fa_{SOC}(SOC = 65\%)$	w.u.	2.55	0.33	0.39
$Fa_{SOC}(SOC = 80\%)$	w.u.	2.23	0.33	0.42
$Fa_{SOC}(SOC = 100\%)$	w.u.	1	1	1
A	w.u.	4.48	4.24	3.18

TABLE IV- 1: IDENTIFICATION RESULTS OF THE DUAL-TANK AGING MODEL PARAMETERS.

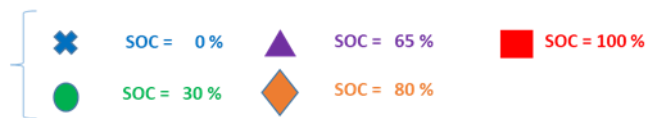
#### IV.2.2.1. $C_{pos}$ aging model parameters identification

The initial positive electrode capacity  $C_{pos_{init}}$  considered in the aging model is equal to 48.5Ah. FIGURE IV- 7 compares the evolution of the positive electrode capacity identified via the dual-tank OCV model with the positive electrode capacity computed via the  $C_{pos}$  aging model. At 0°C, 25°C, and 45°C, the model gives some good agreement with the positive electrode identified previously. The maximum model error is lower than 2% except for all conditions except at 60°C and SOC 65% where the error between simulated and identified values is more important.

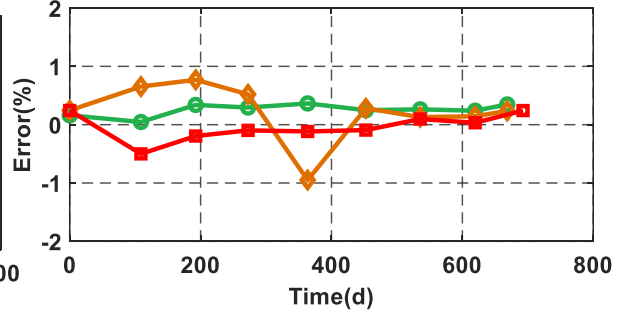
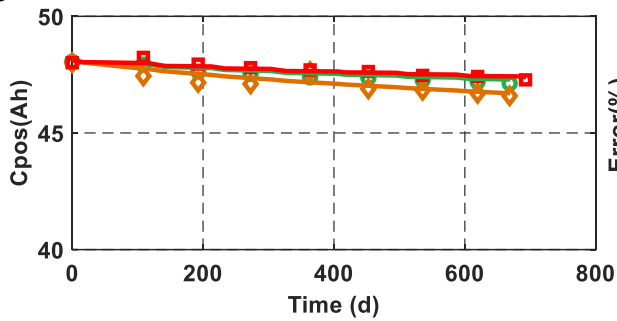
The degradation rate of the positive electrode capacity increases with temperature especially at 60°C where the positive electrode capacity fade is the most important. Concerning the influence of SOC, the simulated parameter  $C_{pos}$  from the aging model shows that the cells are more subjected to a higher active mass loss at the positive electrode at SOC 65%. This observation is consistent with FIGURE IV- 8, which shows the state-of-charge accelerating factor for all SOC breakpoints: the SOC accelerating factor is the highest for SOC 65%. The temperature accelerating factor is high at SOC 0% and SOC 30% at 60°C as shown in FIGURE IV- 8. This is due to the high value of activation energy  $Ea_{T > T_{ref}}$  identified at SOC 30% which enables tracking the trend of SOC 65% & 60°C condition. The SOC profile at 60°C and SOC 65% presented in chapter 2 (FIGURE II- 4) shows that the cell reached the SOC 30% after approximately 150 days of storage. The identified positive capacity is very low after 150 days of storage at 60°C and SOC 30%, thus the model identified a high value of activation energy  $Ea_{T > T_{ref}}$  at SOC 30% (high degradation rate).

Simulated data

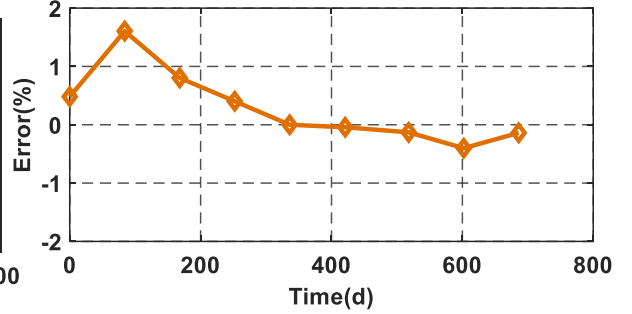
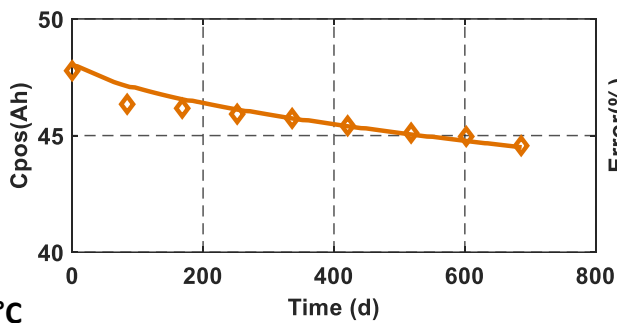
Identified data



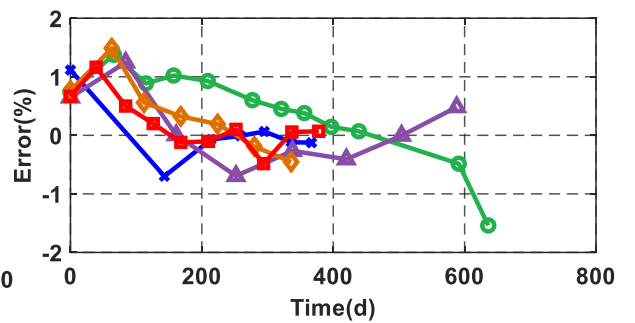
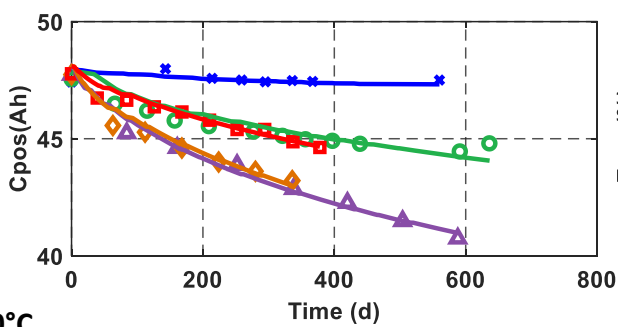
T = 0°C



T = 25°C



T = 45°C



T = 60°C

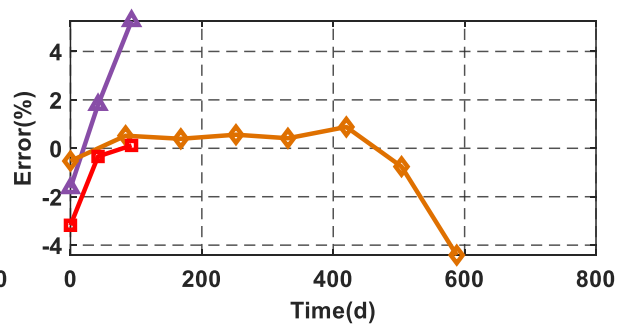
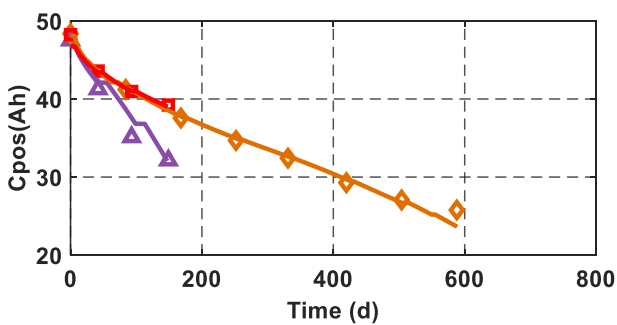


FIGURE IV- 7: CALENDAR AGING IDENTIFICATION OF POSITIVE ELECTRODE CAPACITY.

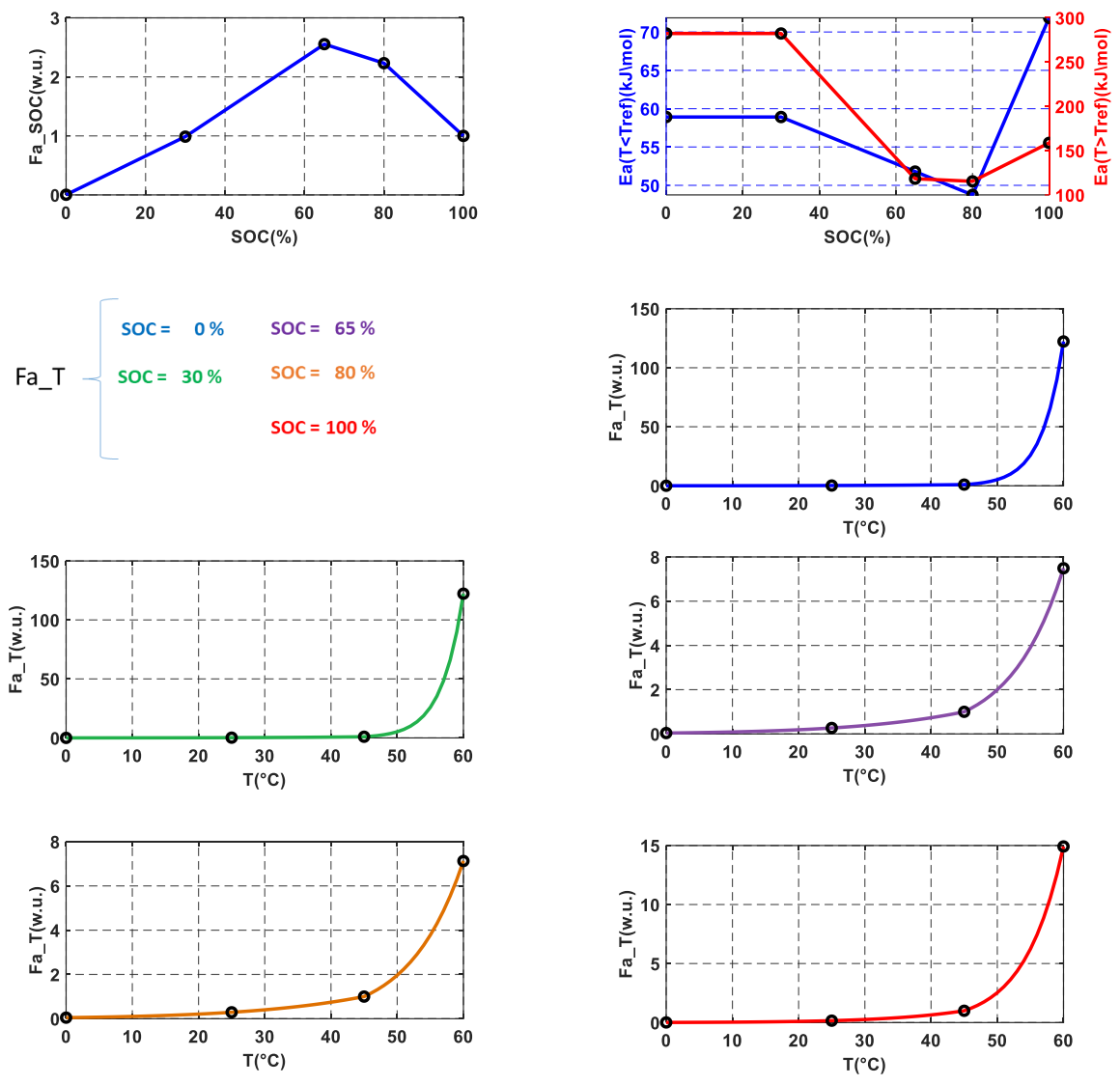


FIGURE IV- 8: IDENTIFICATION OF THE STATE-OF-CHARGE AND TEMPERATURE ACCELERATING FACTOR FROM  $C_{pos}$  AGING MODEL.

#### IV.2.2.2. $C_{neg}$ aging model parameters identification

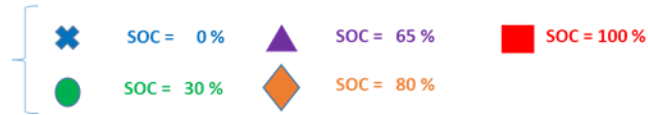
The initial negative electrode capacity  $C_{neg_{init}}$  has been identified using the aging model and is considered equal to 49.5 Ah. The simulated negative electrode capacity from the aging model compared to the identified values from the dual-tank OCV model at different check-ups are shown [FIGURE IV-9](#).

The aging model for the negative electrode is very accurate at temperatures 0°C, 25°C, and 45°C with a maximum error lower than 2%. At temperature 60°C, the identification process  $C_{neg}$  give us a peculiar trend at SOC 80%. The simulated  $C_{neg}$  from the aging model does not follow a  $\sqrt{t}$  trend of capacity loss. At temperature 60°C and SOC 100%, the aging model also tend to overestimate the negative capacity loss as shown in [FIGURE IV-9](#). Nonetheless, the results are still good for the calendar condition at 60°C and 65% of SOC with a maximum below 2%.

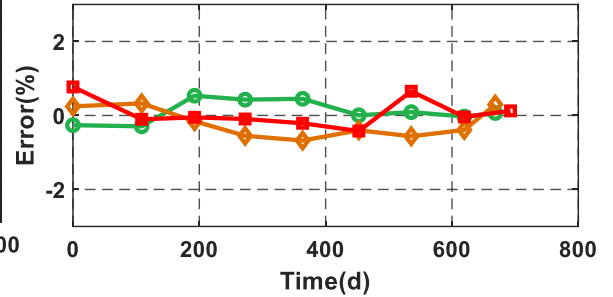
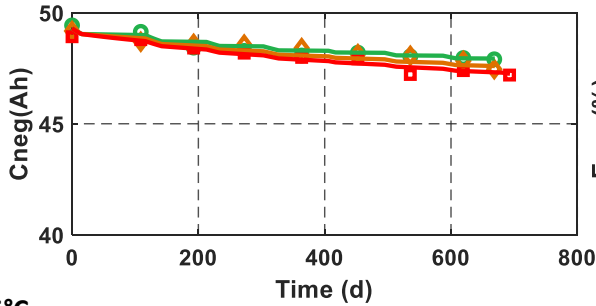
[FIGURE IV-10](#) illustrates the accelerating factor of temperature at SOC 100%, and state-of-charge identified from our aging model for negative electrode capacity. The effect of the temperature is less important on the negative electrode compared to the positive electrode: the temperature accelerating factor  $Fa_T$  for the negative electrode shown in [FIGURE IV-10](#) is smaller than the accelerating factor identified for the positive electrode at 60°C and SOC 30% illustrated in [FIGURE IV-8](#). This phenomenon is due to smaller activation energy  $Ea(SOC)$  identified for the negative electrode aging model. The SOC accelerating factor  $Fa_{SOC}$  has also a different behavior compared to those of the positive electrode capacity: the identification process shows that the degradation phenomena are clearly more important at SOC 100% for the negative electrode and 65% for the positive electrode.

Simulated data

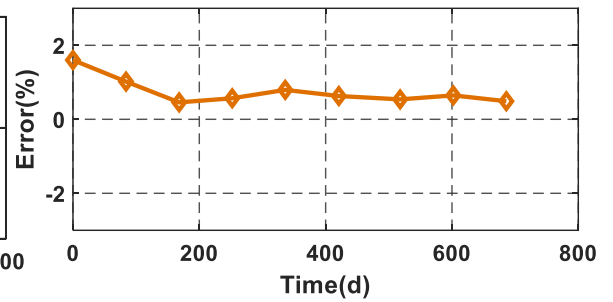
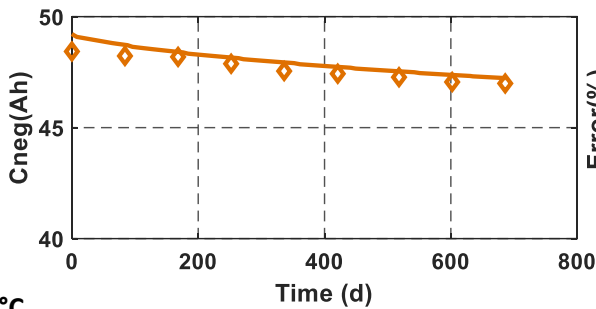
Identified data



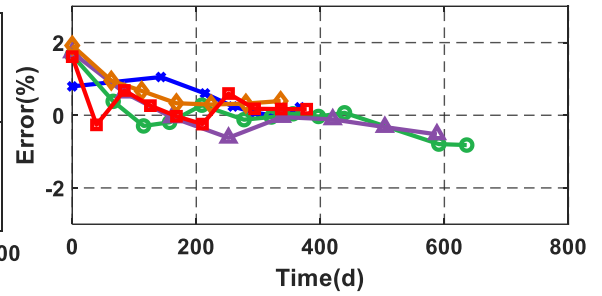
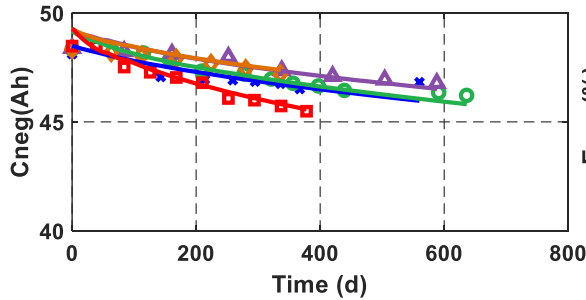
T = 0°C



T = 25°C



T = 45°C



T = 60°C

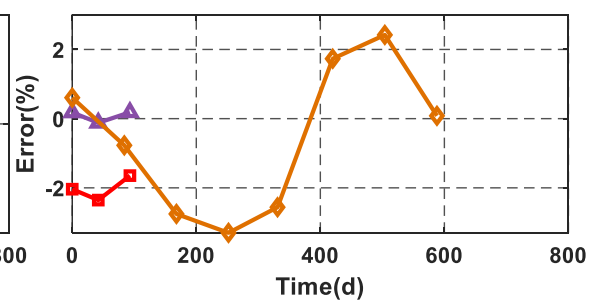
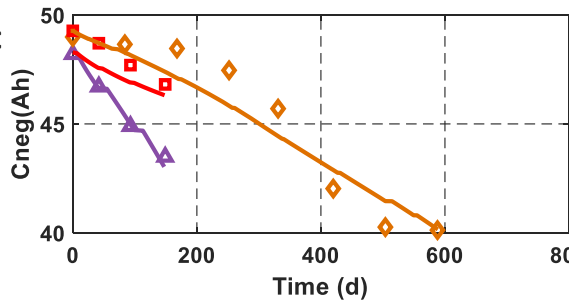


FIGURE IV- 9: CALENDAR AGING IDENTIFICATION OF NEGATIVE ELECTRODE CAPACITY.

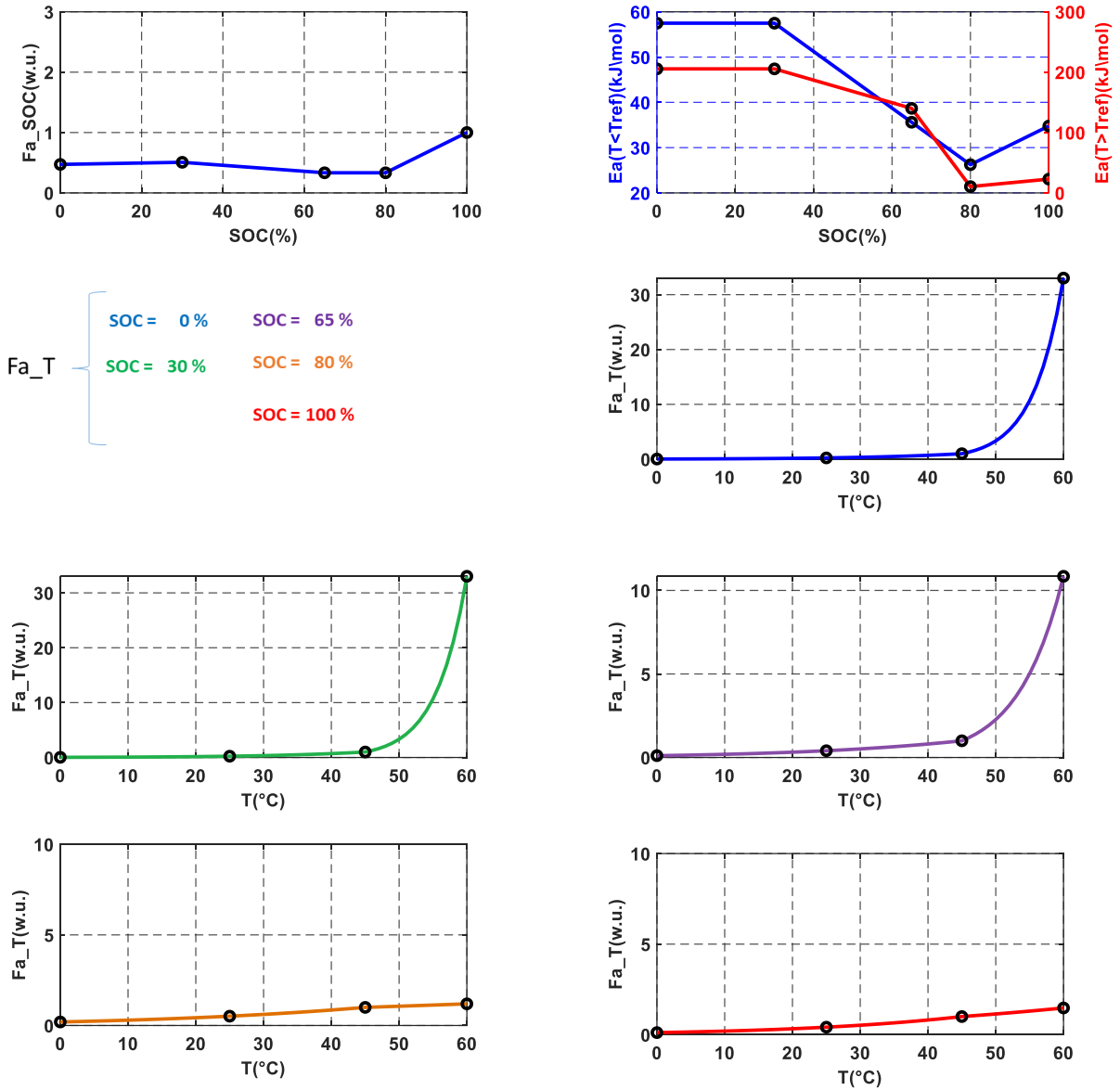


FIGURE IV- 10: IDENTIFICATION RESULTS OF THE STATE-OF-CHARGE AND TEMPERATURE ACCELERATING FACTOR FROM  $C_{neg}$  AGING MODEL.

#### IV.2.2.3. *OFS* aging model parameters identification

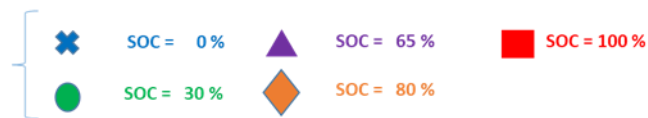
Concerning the offset parameter, we have identified an initial offset of 2.4 Ah. This initial decay between positive and negative potential signals is mainly due to the formation of SEI during cell formation and first cycles. Unlike the other variables, the *OFS* aging model shows low precision with maximum model error up to 20% without considering conditions at 60°C and SOC 65% where degradations are more important.

The identification of the *OFS* aging model parameters gives us fewer good results than the positive and negative electrode capacity aging model. The results are still acceptable for the calendar conditions at 0°C and 25°C. The aging model is still capable of predicting the evolution of the *OFS* parameter at 45°C except for the condition at SOC 65% as shown in [FIGURE IV- 11](#). At temperature 60°C and SOC (65%, 80%), the offset parameter has a peculiar evolution, as noticed in §. IV.1.2.2.3. The aging model still has some problems fitting the data. The physical phenomena at 60°C may be very different from those at 45°C which could explain that the aging model is not capable of fully predict the parameters aging.

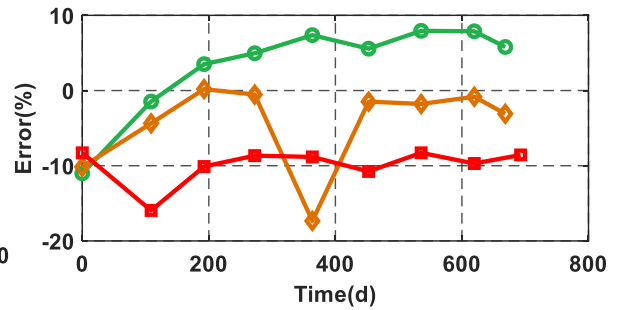
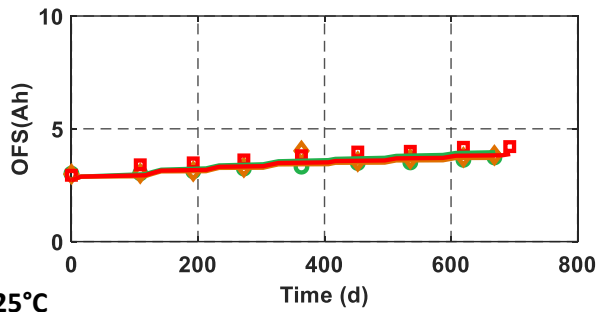
The evolution of the temperature and state-of-charge accelerating factor identified from the offset aging model is presented [FIGURE IV- 12](#). The offset parameter is strongly influenced by operational resting conditions at high temperature and high state-of-charge which is physically explained by the increase of SEI layer activated at those conditions. The accelerating factors have a monotonous effect with temperature and state-of-charge.

Simulated data

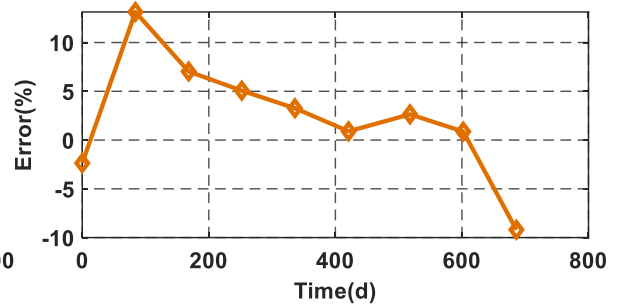
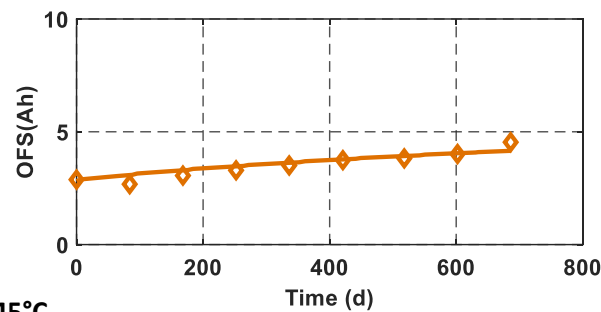
Identified data



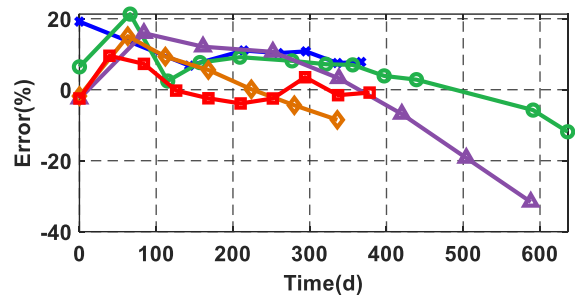
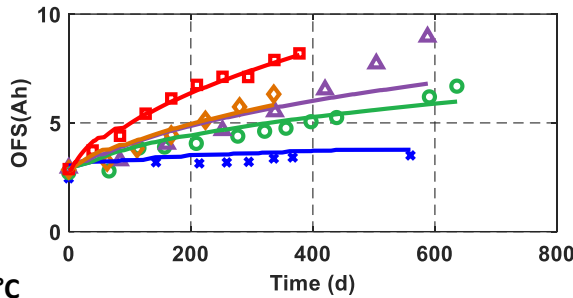
T = 0°C



T = 25°C



T = 45°C



T = 60°C

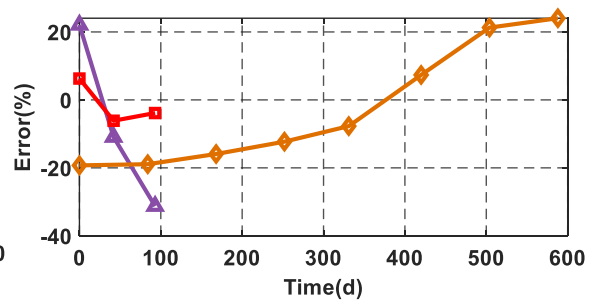
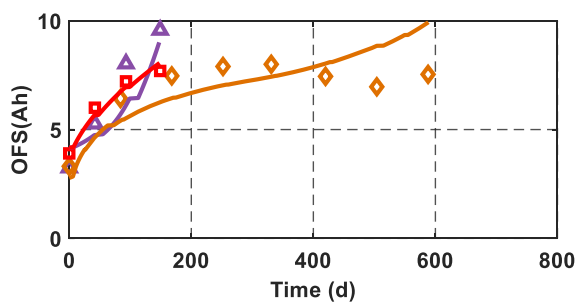


FIGURE IV- 11: CALENDAR AGING IDENTIFICATION OF *OFS*.

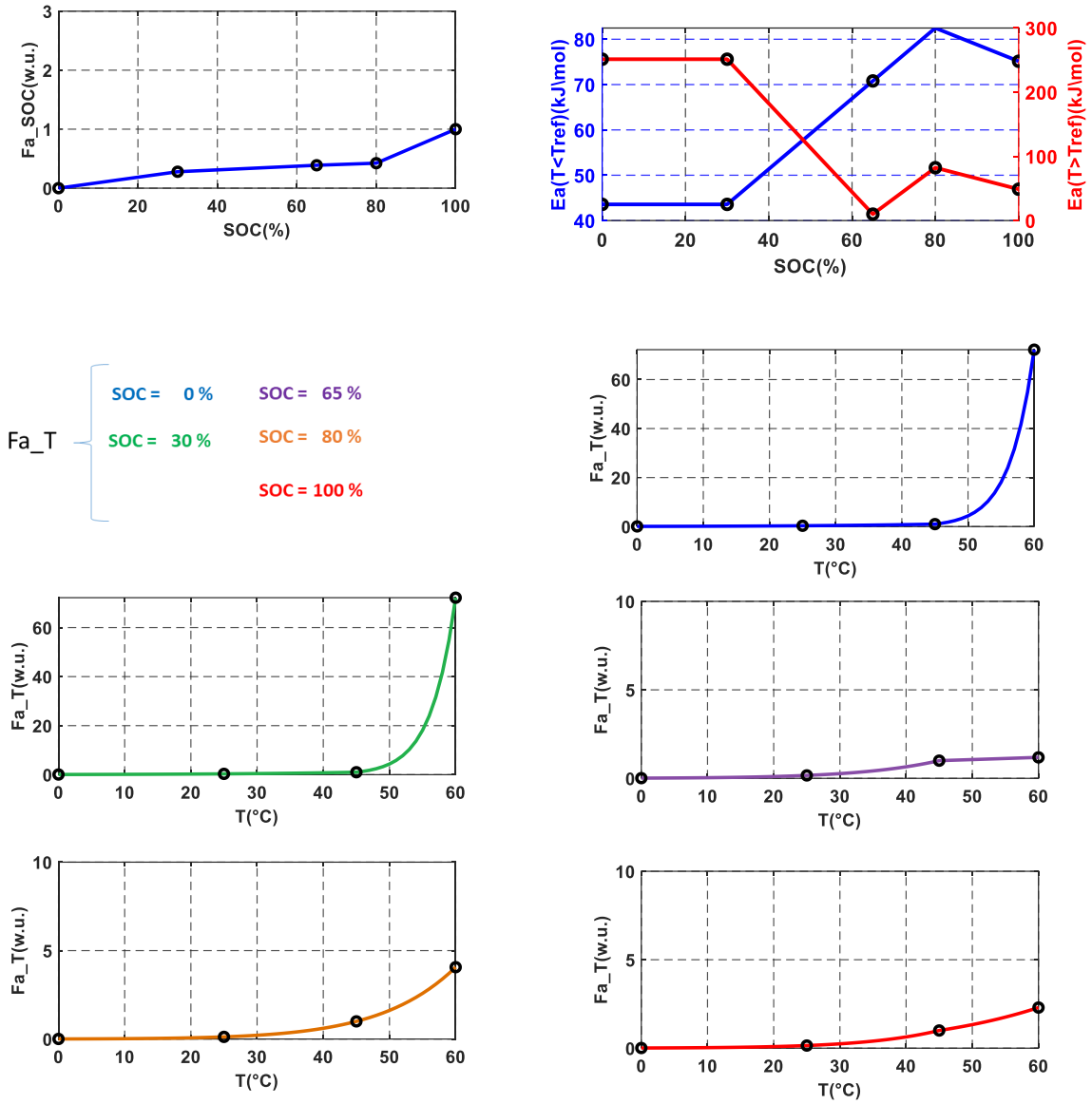


FIGURE IV- 12: IDENTIFICATION OF THE STATE-OF-CHARGE AND TEMPERATURE ACCELERATING FACTOR FROM *OFS* AGING MODEL.

### IV.2.3. Aging model validation

The simulation of the aging models for the positive and negative electrodes shows a good agreement with the parameters identified from the dual-tank OCV model. The overall trend follows a square root function of time. However, the selected model is not enough to predict the *OFS* evolution at 45°C-SOC 65% or at temperature 60°C. The *OFS* parameter has an exponential trend instead of a square root function of time

The final aim of having three different aging models for every three parameters of our dual-tank OCV model is to be able to predict the evolution of the full cell capacity over time when subjected to different calendar operational conditions (temperature and state-of-charge). To validate our aging models, two different conditions described in chapter 2 (§. II.3) are used: the thermal cycling condition at fixed SOC (65% and 100%) and the variable SOC condition at 45°C.

Note that those two conditions are not used for the identification of our three aging model parameters. Thus, they can be used to simulate the full cell capacity for the validation process in two steps. The method is illustrated **FIGURE IV- 13**:

- **Step 1**: we use the parameters identified in **TABLE IV- 1** to simulate  $C_{pos}$ ,  $C_{neg}$  and offset evolution with aging model.
- **Step 2**: we use the dual-tank OCV model to simulate the full cell capacity.

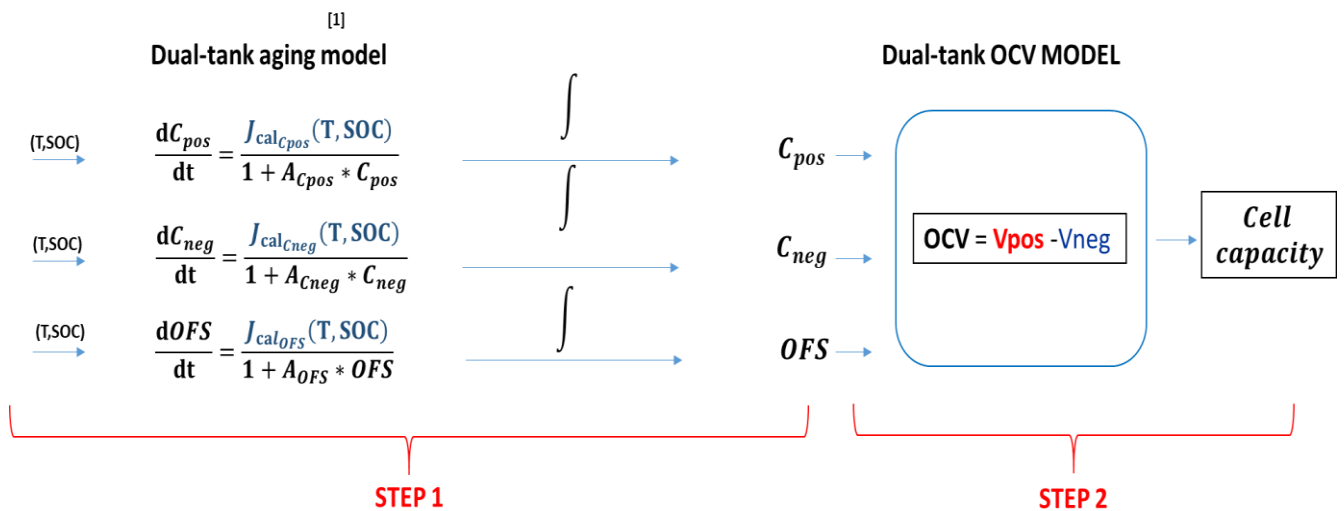


**FIGURE IV- 13: SIMULATION OF THE CELL CAPACITY FROM THE AGING MODEL.**

The aim is to compare the cell capacity prediction using either the one-tank aging model described in chapter 3 or the dual-tank aging model. Using the parameters identified for  $C_{pos}$ ,  $C_{neg}$ , *OFS* aging models (see **TABLE IV- 1**), the aging of the dual-tank OCV model parameters can be simulated (step 1 in **FIGURE IV- 13**). Following this step, the dual-tank OCV model is used to simulate the cell capacity (step 2 in **FIGURE IV- 13**).

The results are shown in **FIGURE IV- 14** which illustrates the cell SOH evolution from the one-tank aging model (dotted lines) and the dual-tank aging models (dashed lines). We can see that the two methods give approximatively the same results. From what we can see **FIGURE IV- 14**, the

dual-tank aging model gives better results for the variable SOC condition using the dual-tank aging model. There is a good agreement between the experimental cell SOH and the simulated cell SOH using the aging models. The thermal cycling condition at SOC 65% is still less well predicted with a maximum error of 15%. For the thermal cycling condition at SOC 100% the two models are slightly equivalent with a maximum error below 3%.

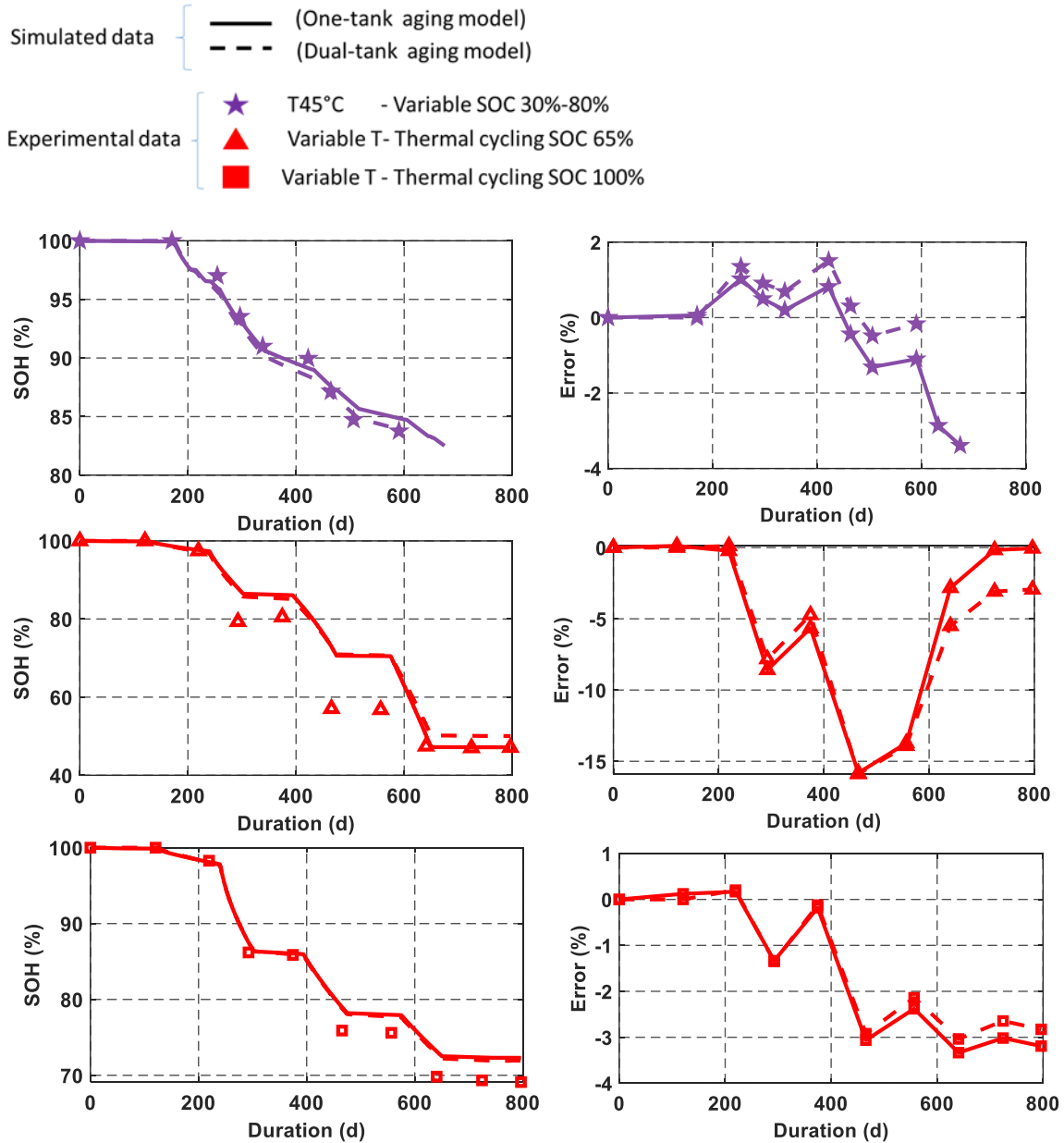


FIGURE IV- 14: COMPARISON BETWEEN ONE TANK AND DUAL-TANK AGING MODELS VALIDATION

The comparison between the one-tank aging model and the dual-tank aging model shows that the two methods are almost equivalent to predict the cell SOH. The two models give some good results.

In addition of giving a good SOH prediction, the dual-tank aging model allows defining the cell SOH with more parameters ( $C_{pos}$ ,  $C_{neg}$ ,  $OFS$ ). It may also be relevant to define more precisely the cell OCV signature depending on the degradation path of ( $C_{pos}$ ,  $C_{neg}$ ,  $OFS$ ).

### IV.3. Evolution of the dual-tank model parameters with aging

In this section, the complete model in **FIGURE IV-13** (dual-tank aging models coupled to the dual-tank OCV model) is used to simulate the evolution of different variables related to the electrodes and full cell. These variables gather the parameters of the dual-tank OCV model ( $C_{pos}$ ,  $C_{neg}$ ,  $OFS$ ) and the electrode potential signals ( $V_{pos}$ ,  $V_{neg}$ ). Setting the cell voltage threshold ( $U_{min}$ ,  $U_{max}$ ) allows following as well the evolution of the maximum and minimum lithium content in each electrode ( $\theta_{posmax}$ ,  $\theta_{negmax}$ ,  $\theta_{posmin}$ ,  $\theta_{negmin}$ ) along with aging for the determination of the evolution of the cell capacity ( $Q_{sim}$ ).

The aging profiles used for this approach is the fixed calendar condition at temperature 45°C and SOC 65%. The SOC and temperature are fixed during the whole simulation. The study is divided into two sections.

In this first section, the simulation is performed using the dual-tank aging parameters identified in **TABLE IV-1** (§. IV.2.2) to see how the variables mentioned above evolve with aging.

In the second and third sections, a sensitivity analysis is performed on the degradation rate at a reference condition  $J_{calref}$  (for each dual-tank aging law in §. IV.2.1) and the electrodes sizing ( $C_{posinit}$ ,  $C_{neginit}$ ). These values are detailed in §. IV.2.2 are changed to analyze their impacts on the electrode potential signals and the maximum/minimum lithium contents.

#### IV.3.1. Simulation of the calendar aging condition at T=45°C and SOC=65%: reference case

##### IV.3.1.1. Aging evolution of the dual-tank OCV parameters and full cell capacity.

The simulation of the cell capacity at a fixed temperature (45°C) and SOC (65%), illustrated in **FIGURE IV-15**, shows that the cell capacity loses almost 33% of its initial capacity within 700 days of cell storage (< 2 years). This degradation of the cell SOH is mainly due to the rapid acceleration of the offset parameter change from approximately 2.3 Ah to 7.5 Ah (> 200% of the increase). It is also related to the degradation of the positive electrode capacity (approximately 17% of initial capacity loss). The evolution of the negative electrode capacity slightly decreases during aging compared to the positive electrode (with 6% of capacity loss within 700 days or resting time).

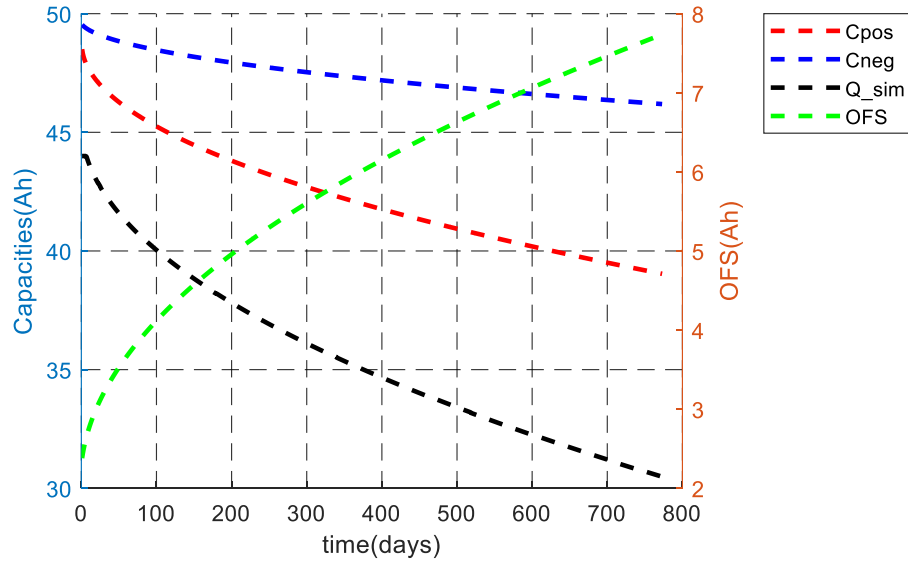


FIGURE IV- 15: SIMULATION OF THE CELL CAPACITY  $Q_{sim}$ ,  $C_{pos}$ ,  $C_{neg}$  AND  $OFS$  AT  $T=45^{\circ}C$  AND  $SOC=65\%$ .

#### IV.3.1.2. Evolution of the positive and negative electrode potential signals

The evolution of the electrode potential signals simulated from the beginning of life until 700 days of storage is shown in FIGURE IV- 16. The pink and black dashed lines correspond to the minimum and maximum limit of the full cell capacity set by the cell voltage threshold ( $U_{min}$  and  $U_{max}$  in FIGURE IV- 16). The evolutions of ( $C_{pos}$ ,  $C_{neg}$ ,  $OFS$ ) previously presented in FIGURE IV- 15 impact the position of the electrode potential signals relative to each other.

The offset set the relative position of the negative electrode at the fully delithiated ( $NEG_{de}$ ) state to the positive one at the fully lithiated state ( $POS_{li}$ ) on the capacity abscissa, as illustrated in FIGURE IV- 16. Due to the increase of the offset parameter along with aging, the distance between the negative electrode  $NEG_{de}$  and the positive electrode  $POS_{li}$  increases. This latter takes place along with the decrease of the length of the positive and negative electrode signal due to the degradation of the positive and negative electrode capacity.

It is worth noting in FIGURE IV-16 that the voltages of the electrodes limits ( $V_{pos_{max}}$ ,  $V_{neg_{max}}$ ,  $V_{pos_{min}}$ ,  $V_{neg_{min}}$ ) change along with cell aging because of the electrode capacity and  $OFS$  evolution. On the negative electrode, the maximum negative potential ( $V_{neg_{max}}$  in FIGURE IV- 16) slightly increases during the 700 days of storage while the minimum negative electrode potential ( $V_{neg_{min}}$ ) increases more rapidly. On the positive electrode, the maximum positive potential  $V_{pos_{max}}$  slightly increases as well through aging while the minimum potential  $V_{pos_{min}}$  increases at a higher rate.

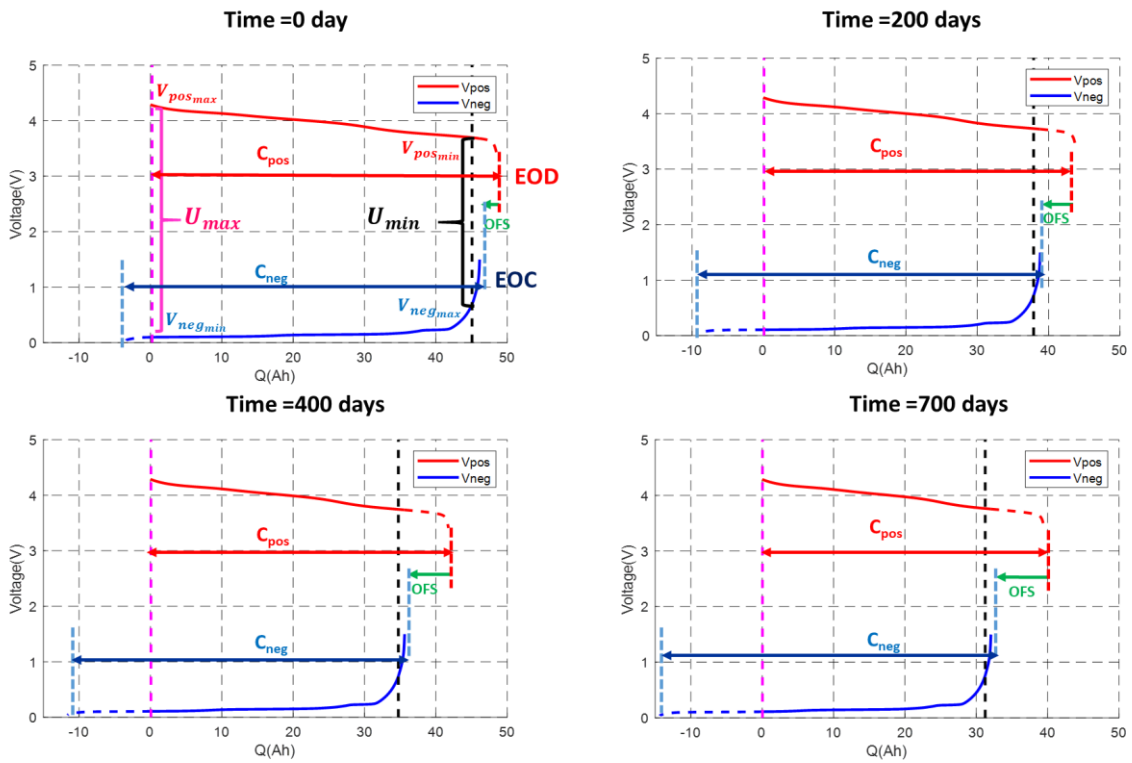


FIGURE IV- 16: EVOLUTION OF THE ELECTRODE POTENTIAL SIGNALS AFTER 700 DAYS OF CALENDAR AGING

#### IV.3.1.3. Evolution of the maximum and minimum lithium content

The evolution of the minimum and maximum lithium contents ( $\theta_{pos_{max}}$ ,  $\theta_{neg_{max}}$ ,  $\theta_{pos_{min}}$ ,  $\theta_{neg_{min}}$ ) illustrated in FIGURE IV- 17, shows that the four parameters decrease in the electrodes through aging. This evolution can be explained based upon the description of the electrode potential detailed in §.IV.3.1.2

- As noticed previously, the negative potential at the cell EOD ( $V_{neg_{max}}$ ) and the positive potential at the cell EOC ( $V_{pos_{max}}$ ) slightly increase after 700 days of storage. Therefore, the minimum lithium content at both electrodes barely decreases during aging.
- As the minimum electrode voltages  $V_{pos_{min}}$  and  $V_{neg_{min}}$  increases at a higher rate along with aging, the evolution of the maximum lithium content on both electrodes show that they decrease fast. From the beginning to the end of the simulation, the maximum positive  $\theta_{pos_{max}}$  lithium content decreases by approximately 10% while the maximum negative lithium  $\theta_{neg_{max}}$  content decreases by 27% of its initial value.

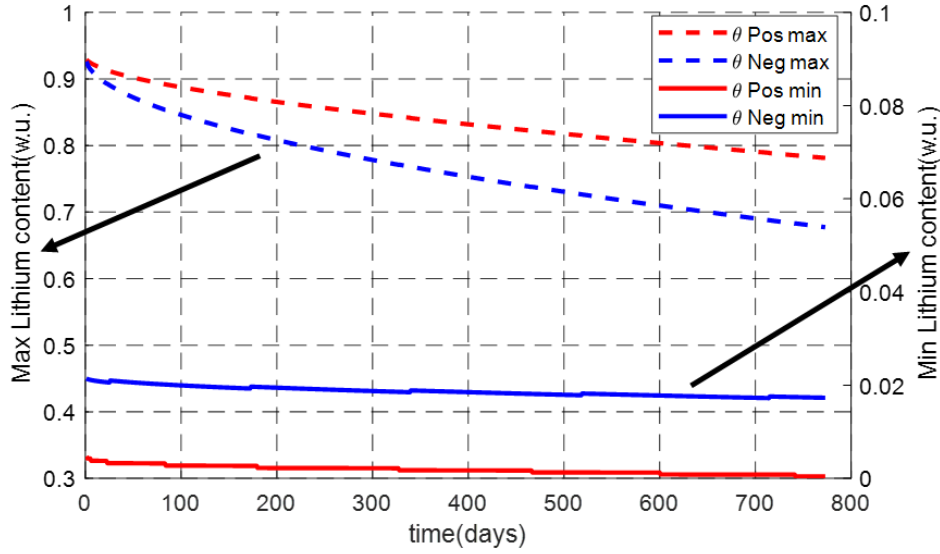


FIGURE IV- 17: SIMULATION OF THE MAXIMUM AND MINIMUM ELECTRODES LITHIUM CONTENT AT T=45°C AND SOC =65%.

### IV.3.2. Influence of the degradation rate on the electrode lithium contents

In this section, the sensitivity analysis of the degradation rate at a reference condition  $J_{cal_{ref}}$  for each dual-tank aging, model is performed by multiplying it by a factor equal to 5. The evolutions of the electrode potential signals in this section are compared after 700 days of calendar storage. The aim is to analyze how accelerating the degradation rate of the dual-tank aging models affects the electrode potential signals and maximum/minimum lithium contents of the electrodes.

#### IV.3.2.1. Acceleration of the positive electrode capacity $C_{pos}$ aging parameter

The evolution of the electrode potential signals and maximum/minimum lithium contents are illustrated in FIGURE IV- 18 after 700 days of storage when accelerating the positive electrode capacity  $C_{pos}$  aging parameter.

On the positive electrode signal in FIGURE IV- 18(b), the maximum voltages  $V_{pos_{max}}$  barely increases while the minimum positive voltage  $V_{pos_{min}}$  increases a lot at end of the simulation compared to the reference (initial) case shown in FIGURE IV- 18(a). Therefore, the minimum lithium content  $\theta_{pos_{min}}$  slowly decreases while the maximum lithium content  $\theta_{pos_{max}}$  decreases at a higher rate along with aging in FIGURE IV- 18(d) compared to FIGURE IV- 18(c).

On the negative electrode signal, the acceleration of the positive degradation mostly affect the minimum voltage  $V_{neg_{min}}$ , which increases more rapidly in FIGURE IV- 18(b) than in the reference case in FIGURE IV- 18(a). Therefore, the maximum lithium content  $\theta_{neg_{max}}$  decreases faster as well in FIGURE IV- 18(d) compared to FIGURE IV- 18(c). The maximum voltage  $V_{neg_{max}}$  barely increases along with aging consequently in FIGURE IV- 18(b) compared to FIGURE IV- 18(a). Thus,  $\theta_{neg_{min}}$  slowly decreases as shown in FIGURE IV- 18(d).

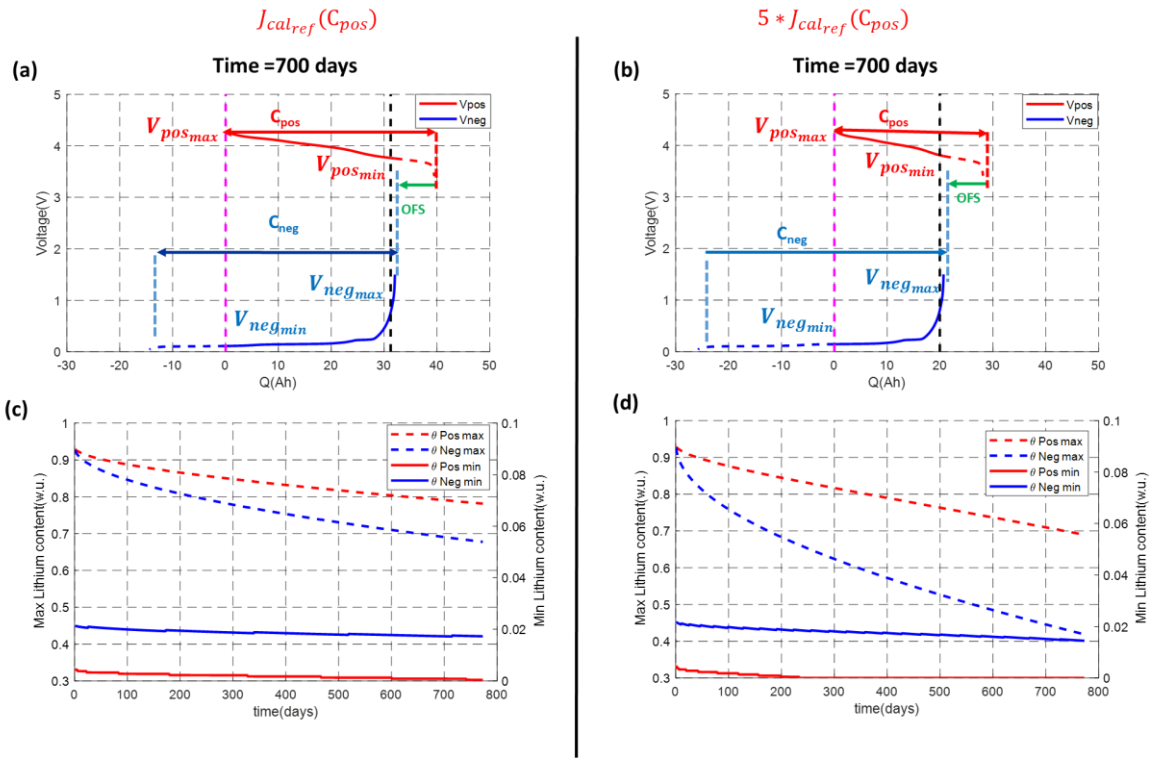


FIGURE IV- 18: EVOLUTION OF THE ELECTRODE POTENTIAL SIGNALS AT 700 DAYS (A, B) AND MINIMUM/MAXIMUM LITHIUM CONTENT (C, D) WHEN CHANGING  $J_{cal\_ref}$  OF THE POSITIVE ELECTRODE AGING MODEL.

IV.3.2.2. Acceleration of the electrode capacity  $C_{neg}$  aging parameter

The evolution of the electrode potential signals are illustrated in FIGURE IV- 19(a, b) after 700 days of storage when accelerating the degradation rate of  $C_{neg}$  aging parameter.

On the negative electrode, the maximum voltage  $V_{neg\_max}$  slightly decreases during the simulation shown in FIGURE IV- 19(b) compared to the reference case shown in FIGURE IV- 19(a). Therefore, the minimum lithium content  $\theta_{neg\_min}$  in FIGURE IV- 19(d) slightly increases compared to FIGURE IV- 19(c). The minimum voltage  $V_{neg\_min}$  decreases along with aging due to the reduction of the negative electrode capacity. Consequently, the maximum lithium content  $\theta_{neg\_max}$  in FIGURE IV- 19(d) increases through the simulation compared to the case in FIGURE IV- 19(c).

On the positive electrode, the maximum positive voltage  $V_{pos\_max}$  slightly decreases therefore the minimum lithium content  $\theta_{pos\_min}$  in FIGURE IV- 19(d) slightly increases compared to the initial case shown in FIGURE IV- 19(c).

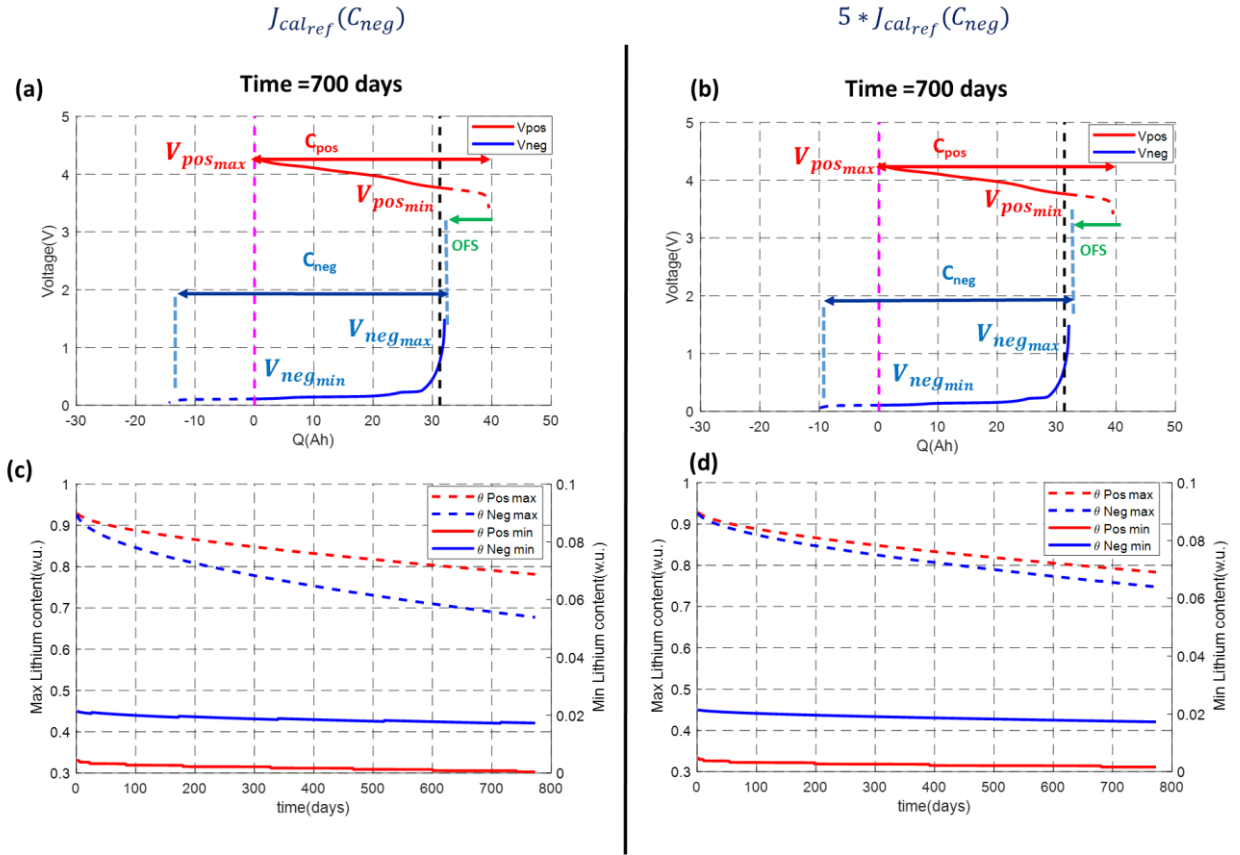


FIGURE IV- 19: EVOLUTION OF THE ELECTRODE POTENTIAL SIGNALS AT 700 DAYS (A, B) AND MINIMUM/MAXIMUM LITHIUM CONTENT (C, D) WHEN CHANGING  $J_{cal\_ref}$  OF THE NEGATIVE ELECTRODE AGING MODEL.

#### IV.3.2.3. Acceleration of OFS aging

The evolution of the electrode potential signals is illustrated in FIGURE IV- 20(a, b) after 700 days of storage. When accelerating the degradation rate  $J_{cal\_ref}$  of the offset aging model, the negative electrode potential signal shifts more and more rapidly to the left. This shift is due to fact that fewer lithium-ions are accessible in the system and therefore, the lithium content of the negative electrode decreases.

As shown in FIGURE IV- 20, the offset parameter mostly impacts the minimum voltages  $V_{pos\_min}$  and  $V_{neg\_min}$  which both increasing in FIGURE IV- 20(b) during the simulation compared to the trend in the reference case shown in FIGURE IV- 20(a). The increase of the minimum voltages is associated with a lower maximum lithium content for both electrode  $\theta_{pos\_max}$  and  $\theta_{neg\_max}$  as presented in FIGURE IV- 20(d) compared to FIGURE IV- 20(c).

As the maximum voltages  $V_{pos\_max}$  and  $V_{neg\_max}$  slightly increase in FIGURE IV- 20(a) after 700 days of storage due to the acceleration of offset aging parameter, Thus, the minimum lithium contents  $\theta_{pos\_min}$  and  $\theta_{neg\_min}$  slightly decrease in FIGURE IV- 20(d) compared to the results in the reference case (FIGURE IV- 20(c)).

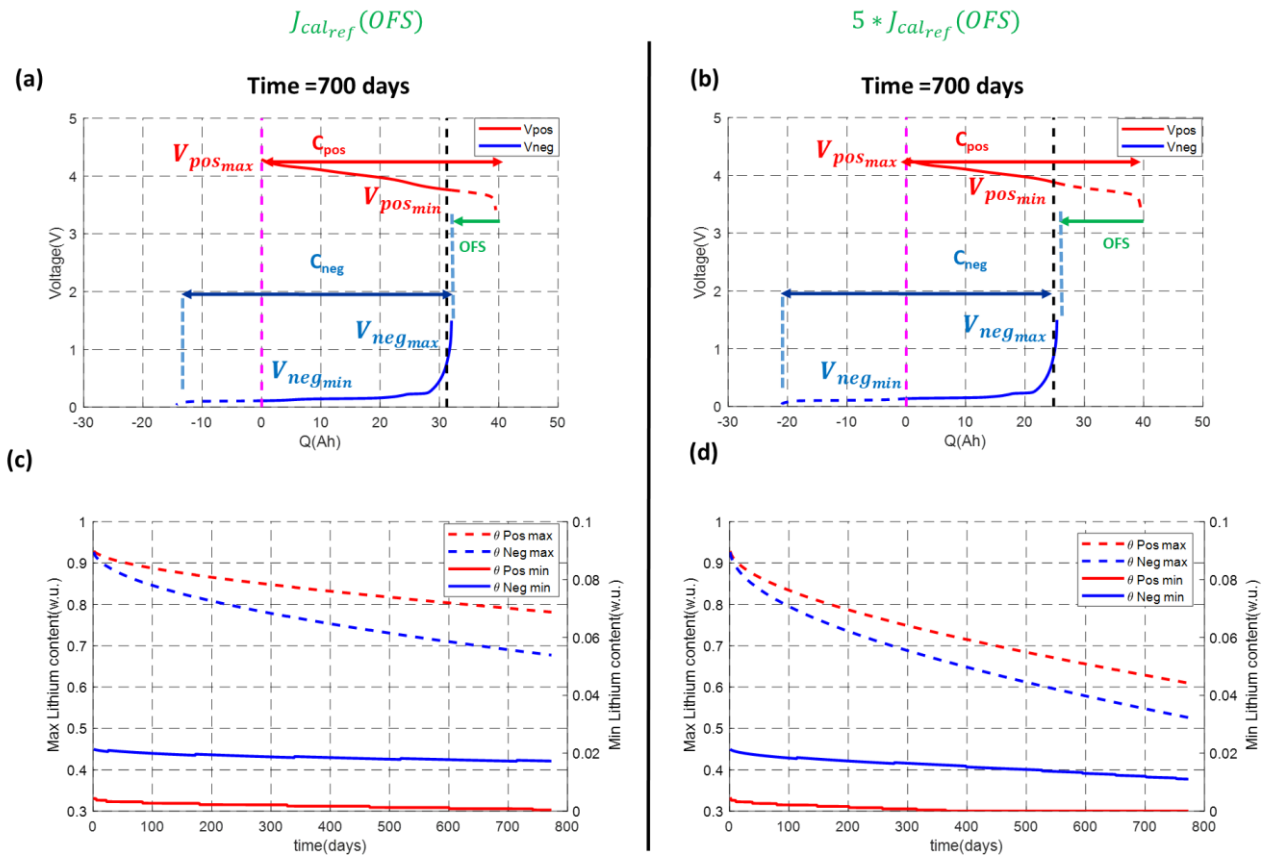


FIGURE IV- 20: EVOLUTION OF THE ELECTRODE POTENTIAL SIGNALS AT 700 DAYS (A, B) AND MINIMUM/MAXIMUM LITHIUM CONTENT (C, D) WHEN CHANGING  $J_{cal_{ref}}$  OF THE OFFSET AGING MODEL.

### IV.3.3. Influence of the electrodes sizing on the electrode potential signals and lithium content

In this section, three studied cases are considered where the sizing of the electrodes (electrode capacities) are changed to analyze their influence on the electrode potential signals as well as the minimum and maximum lithium contents along with aging. The initial positive and negative electrode capacity estimated by the aging models are respectively 48.5 Ah and 49.5 Ah (see TABLE IV- 1). The other parameters identified in TABLE IV- 1 are kept constant for the simulation of the complete model. All the results are compared to the initial case studied in §3.1.

In §3.3.1 and §3.3.2, the positive electrode is respectively undersized (40 Ah) and oversized (60 Ah) compared to the negative electrode.

#### IV.3.3.1. Positive electrode undersized

The evolution of the electrode potential signals is depicted in FIGURE IV- 21(a, b) at BOL. The full cell capacity at BOL will be lower compared to the initial case studied in §3.1.1 due to the reduction of the sizing of the positive electrode.

Reducing the size of the positive electrode mainly affects the value of the minimum voltage of the negative one  $V_{neg_{min}}$ .

When setting the cell voltage threshold, the value  $V_{neg_{min}}$  at BOL, shown in FIGURE IV- 21(b), is higher compared to the initial case (FIGURE IV- 21(a)). Thus, the value of  $\theta_{neg_{max}}$  at BOL is lower in FIGURE IV- 21(d) than in the reference case. Consequently, the simulation illustrated in FIGURE IV- 21(d) shows that the maximum lithium content on the negative electrode  $\theta_{neg_{max}}$  falls with a lower initial value compared to the reference case presented in FIGURE IV- 21(c). The trend of the maximum and minimum lithium contents in FIGURE IV- 21(d) is the same compared to FIGURE IV- 21(c).

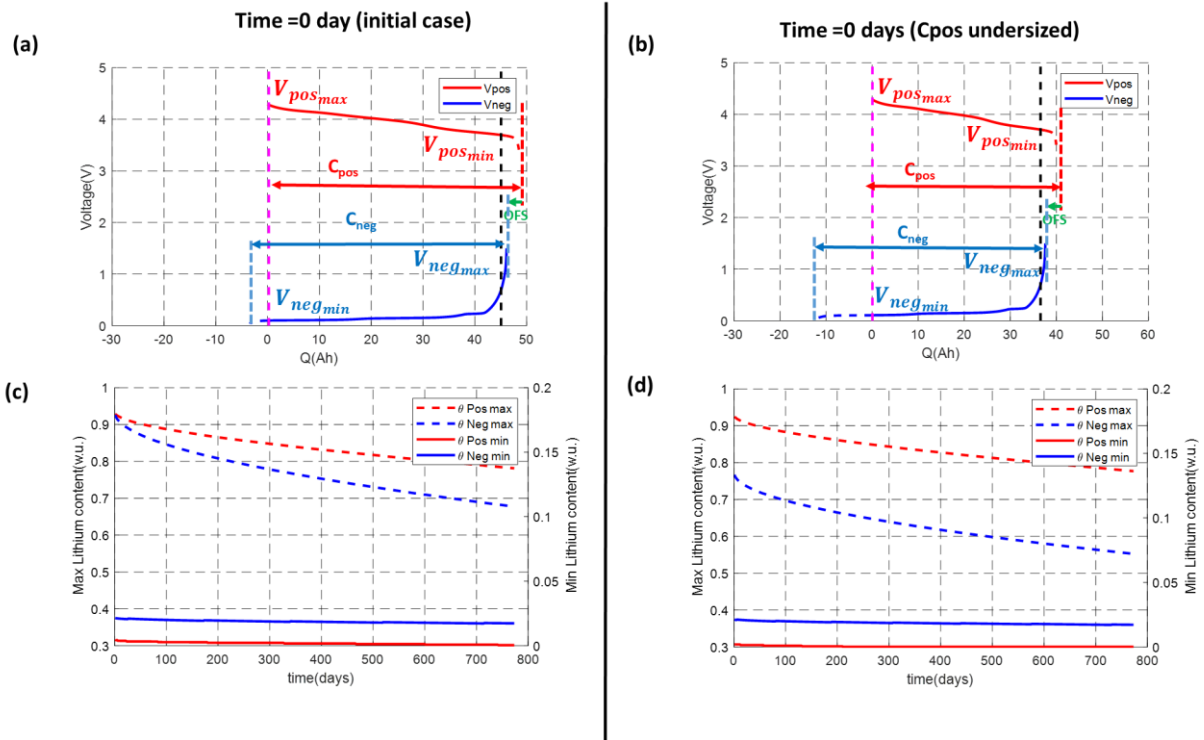


FIGURE IV- 21: POSITIVE ELECTRODE UNDERSIZED: EVOLUTION OF THE ELECTRODES SIGNALS (A, B) AT BOL AND AFTER 700 DAYS OF STORAGE, EVOLUTION OF THE MINIMUM AND MAXIMUM LITHIUM CONTENT (C, D).

#### IV.3.3.2. Positive electrode oversized

FIGURE IV- 22 illustrates the evolution of the electrode potential signals at BOL (a, b) in the reference case and when the positive electrode is oversized. The value of  $V_{neg_{min}}$  and  $V_{pos_{max}}$  is lower at BOL as shown in FIGURE IV- 22(b) compared to the reference case in FIGURE IV- 22(a). Thus, the maximum lithium content  $\theta_{neg_{max}}$  and the minimum lithium content  $\theta_{pos_{min}}$  increases at BOL compared to the reference case.

The configuration of the electrode potential signals at BOL is very different in both cases. In FIGURE IV- 22(b), the negative electrode at the EOC and EOD delimits the cell capacity. The evolution of the minimum lithium content  $\theta_{pos_{min}}$  and maximum lithium content  $\theta_{neg_{max}}$  along with aging are not the same in both cases. As shown in FIGURE IV- 22(d), the maximum lithium content  $\theta_{neg_{max}} = 1$  until approximately 300 days of storage and then decreases along with aging. The minimum lithium content decreases along with aging starting from approximately  $\theta_{pos_{min}} = 0.15$ .

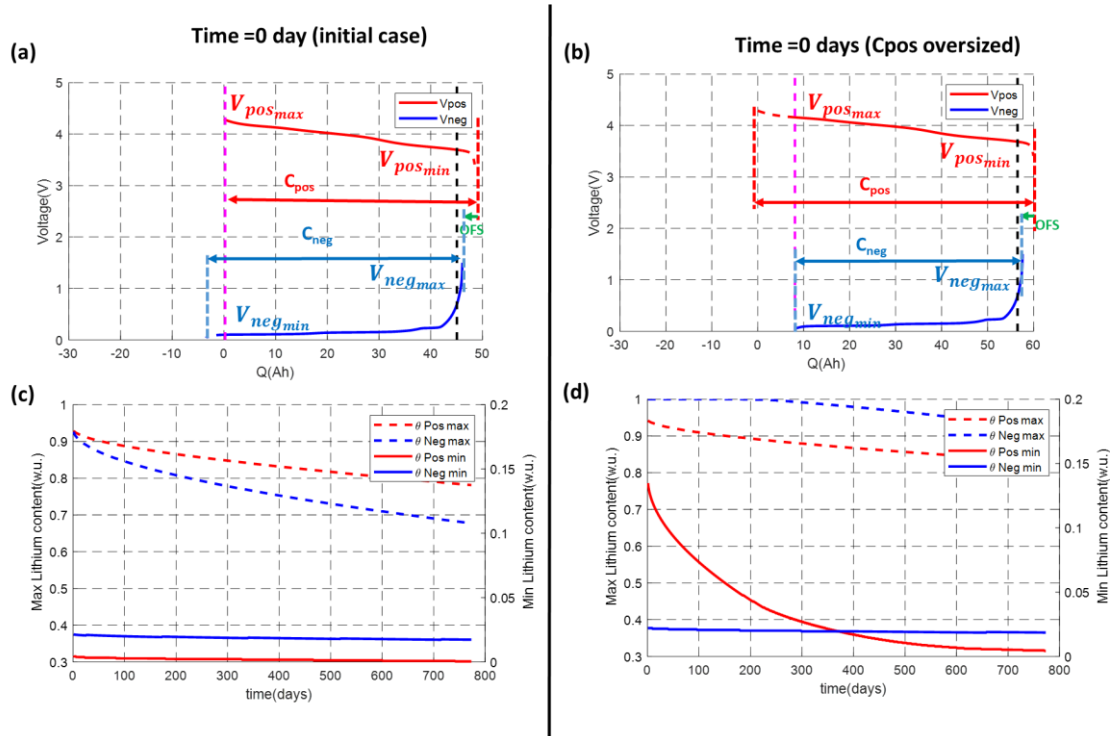


FIGURE IV- 22: POSITIVE ELECTRODE OVERSIZED: EVOLUTION OF THE ELECTRODES SIGNALS (A, B) AT BOL AND AFTER 700 DAYS OF STORAGE, EVOLUTION OF THE MINIMUM AND MAXIMUM LITHIUM CONTENT (C, D).

To explain the evolution of  $\theta_{neg,max}$  and  $\theta_{pos,min}$ , the evolution of the electrode potential signals at different aging states is illustrated in FIGURE IV- 23:

- Before 300 days of storage, the negative electrode delimits the cell capacity at the cell EOC. Thus, the minimum voltage  $V_{neg,min}$  does not evolve and correspond to a maximum lithium content  $\theta_{neg,max}$  equal to 1 as shown in FIGURE IV- 22. The maximum voltage  $V_{pos,max}$  increases between the BOL and 300 days of storage. Thus, the corresponding minimum lithium content  $\theta_{pos,min}$  decreases along with aging.
- After 300 days of storage, the positive electrode delimits the cell capacity at the cell EOC. The minimum voltage  $V_{neg,min}$  start to increase after 300 days of storage. Therefore, the maximum lithium content  $\theta_{neg,max}$  decreases after 300 days of storage. On the positive electrode, the maximum voltage  $V_{pos,max}$  still decreases over time corresponding to a minimum lithium content  $\theta_{pos,min}$  decreasing along with aging.

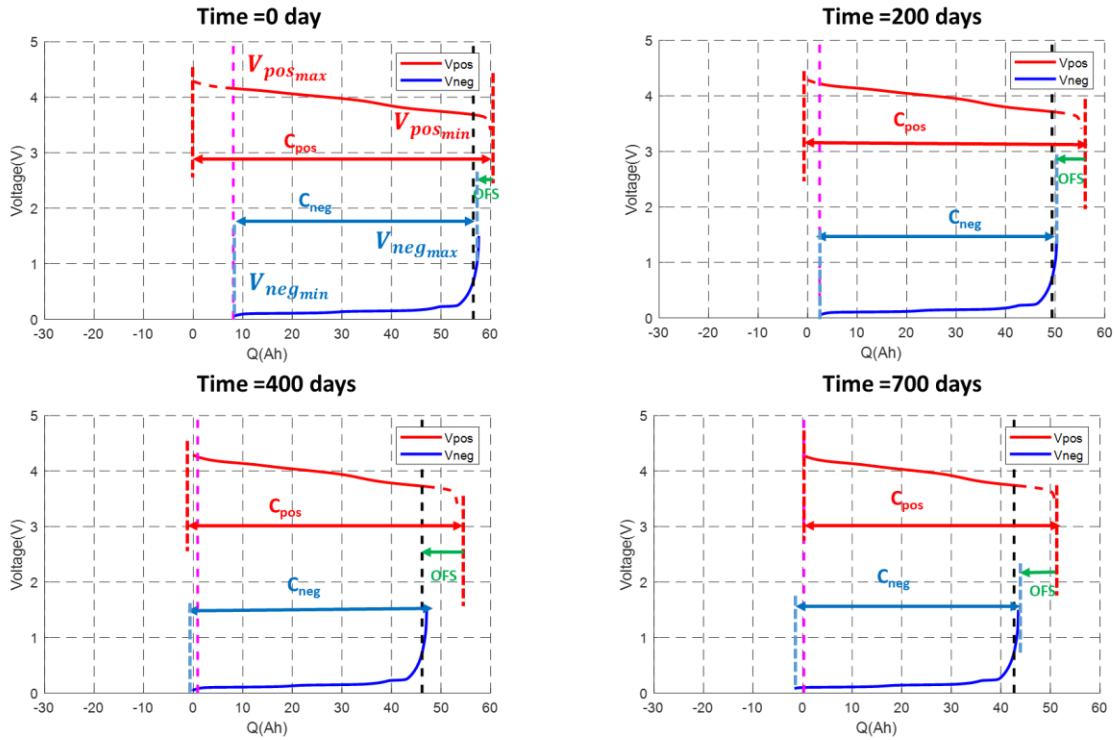


FIGURE IV- 23: EVOLUTION OF THE ELECTRODE POTENTIAL SIGNALS WHEN THE POSITIVE ELECTRODE IS OVERSIZED.

## Conclusion

Semi-empirical aging models coupled to a dual-tank OCV model were developed in this chapter. The dual-tank OCV model was able to simulate the Open-Circuit Voltage ( $OCV$ ) and cell capacity ( $Q_{sim}$ ) as well as the minimum/maximum lithium contents ( $\theta_{pos_{max}}$ ,  $\theta_{neg_{max}}$ ,  $\theta_{pos_{min}}$ ,  $\theta_{neg_{min}}$ ) on both electrodes at a given aging state using three parameters. Those three parameters were: the positive electrode capacity ( $C_{pos}$ ), the negative electrode capacity ( $C_{neg}$ ) and the offset between the electrode potential signals ( $OFS$ ).

The identification of the parameters of the dual-tank OCV model for different calendar aging conditions showed that the degradation of the positive electrode capacity was more important at SOC 65%. The aging of the negative electrode capacity and offset was more predominant at SOC 100%. The aging of the three parameters increased at high temperature, especially at 60°C.

The evolution of the three parameters showed that they aged with a different amplitude of degradation depending on the calendar aging condition. At a given aging state, the cell SOH was defined by ( $C_{pos}$ ,  $C_{neg}$ ,  $OFS$ ) parameters which allowed to define the SOH with more variables.

This aging model was developed to predict the evolution of ( $C_{pos}$ ,  $C_{neg}$ ,  $OFS$ ) and the cell capacity. The identification of this dual-tank aging model gave better results for the positive electrode ( $C_{pos}$ ) and the negative electrode ( $C_{neg}$ ) with a maximum error between 2% and 4%. The identification of the  $OFS$  aging model gave poorer results with a maximum error between 20% and 40%. Nevertheless, the validation of the dual-tank aging model gave some satisfactory results for the SOH prognosis. The maximum error between the experimental and

simulated cell SOH for the variable SOC and thermal cycling condition at SOC 100% were below 4%. However, the validation of the thermal cycling condition at SOC 65% was poorer with a maximum error reaching 15%. Finally, the comparison between the one-tank aging model developed in chapter 3 and the dual-tank aging model showed that results for the prognosis of the cell SOH are slightly equivalent.

To finish, the dual-tank aging model was used to analyze the evolution of its variables with aging. A focus was made on the minimum and maximum lithium contents ( $\theta_{posmax}$ ,  $\theta_{negmax}$ ,  $\theta_{posmin}$ ,  $\theta_{negmin}$ ) on the negative and positive electrodes. The simulations of the reference case, for the calendar aging condition at 45°C and SOC 65%, showed that the lithium contents decrease along with aging due to ( $C_{pos}$ ,  $C_{neg}$ ,  $OFS$ ) evolution. Moreover, the sensitivity analysis performed on the degradation rate  $J_{cal_{ref}}$  of the aging laws showed that the evolution of  $C_{pos}$ ,  $C_{neg}$  and  $OFS$  affect the lithium contents ( $\theta_{posmax}$ ,  $\theta_{negmax}$ ,  $\theta_{posmin}$ ,  $\theta_{negmin}$ ).

ANNEX 1

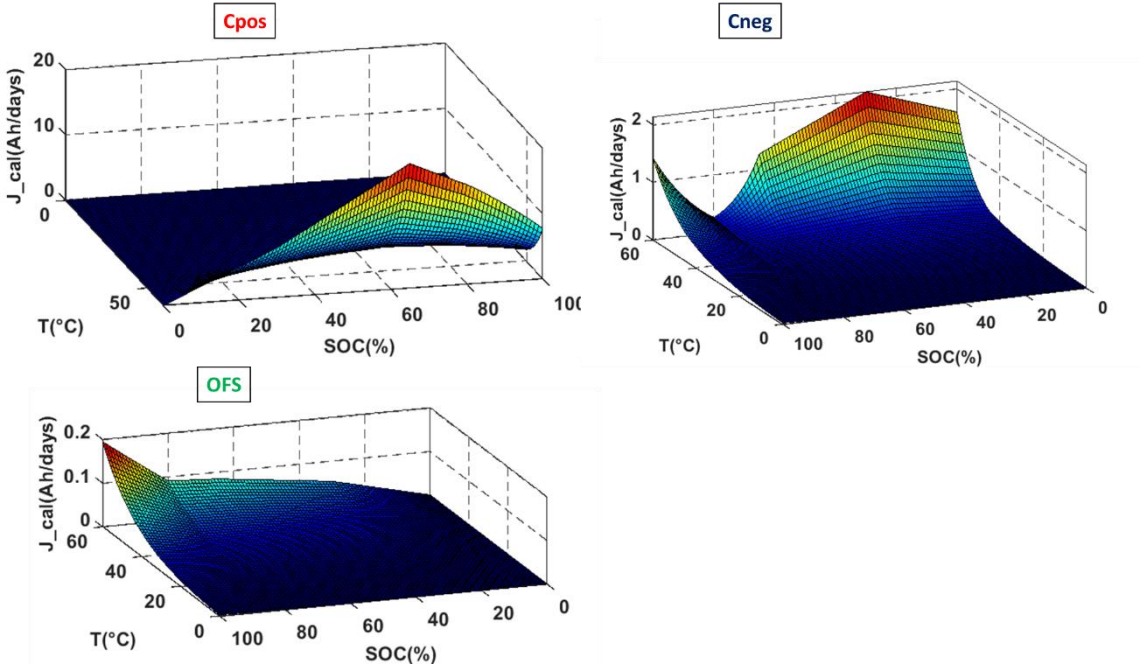


FIGURE IV- 24: DEGRADATION RATE ( $J_{cal}$ ) OF  $C_{pos}$ ,  $C_{neg}$  AND  $OFS$  AGING MODEL.

CHAPTER 5: DUAL-TANK PHYSIC BASED AGING MODEL

## Introduction

Chapter 4 presented the development of a dual-tank aging model for each parameter of the dual-tank OCV model ( $C_{pos}$ ,  $C_{neg}$ ,  $OFS$ ). This model can give a good estimation of the cell battery SOH. However, empirical models lack physical contributions to highlight the possible degradation mechanisms (SEI growth, binder decomposition...) responsible for the cell capacity fade. These degradation mechanisms lead to various degradation modes. As described in chapter 1, the degradation modes responsible for the battery SOH fading can be divided into three main groups: loss of lithium inventory ( $LLI$ ), loss of active mass at the positive electrode ( $LAM_{pos}$ ) and loss of active mass at the negative electrode ( $LAM_{neg}$ ). The  $LLI$  comes from the SEI formation and growth on the negative electrode [8] while the loss of active mass on both electrodes is linked to electrode capacity degradation [81].

As described in chapter 1, several physics-based aging models are developed in the literature to describe the SEI growth responsible for LLI ([41], [82]–[84]). However, there are few existing approaches modeling the loss of active mass on the electrodes [51]. The SEI models developed in the literature are very suitable for calendar aging as the SEI is an important cause of the battery capacity fading. In this chapter, the modeling of SEI growth on production Li-ion batteries is developed based on a physics-based model for the offset ( $OFS$ ) parameter.

The first section presents the mechanism and equations related to the SEI growth at the negative electrode interface for the SEI modeling. A focus is made on the modeling of a parasitic current and the reaction of lithium ions consumption at the SEI/graphite interface.

In the second section, a physics-based aging model for the offset parameter is developed. This model dissociates the impact of the parasitic current and the loss of active mass on both electrodes on the offset parameter.

In the third section, the identification process of the physics-based aging model for the  $OFS$  parameter is developed. This step allows analyzing the evolution of the SEI thickness growth on the production cell batteries as well as the contributions of the degradation modes previously mentioned on the offset parameter.

Finally, the fourth section is entitled to the validation of the physics-based aging model. The results are compared to the one-tank aging model developed in chapter 3 (§. III.2.3).

## V.1. SEI modeling

### V.1.1. Full cell representation

A representation of the full cell is given in **FIGURE V- 1**. In this chapter, the Solid Electrolyte Interphase (SEI) is represented as a porous layer on the negative electrode.

At the negative electrode, the principal reaction is the intercalation of the lithium-ions in the graphite electrode while the SEI growth is supposed to be related to side reaction at the interface graphite/SEI. Namely, the solvent (X) diffuses through the SEI and is reduced at the graphite/SEI interface with intercalated lithium and precipitates into a solid product.

At the graphite/SEI interface, the total current density  $i$  ( $A.m^{-2}$ ) is subdivided into the intercalation current density  $i_n$  and the parasitic current density  $i_p$ . The intercalation current  $i_n$  represents the charge transfer leading to Li intercalation in the graphite solid phase while the parasitic current  $i_p$  represents the charge transfer rate of the SEI reaction. This latter parasitic reaction leads to the growth of SEI (thickness  $\delta_{SEI}$ ).

In **FIGURE V- 1**, the local potentials of graphite (at  $x = 0$ ), SEI (at  $x = 0$ ) and electrolyte interface (at  $x = \delta_{SEI}$ ), are respectively  $\phi_{neg}$ ,  $\phi_{SEI}$  and  $\phi_e$ . The potential difference between the graphite/SEI interface and between the graphite and electrolyte is defined as  $U_{neg}$  and  $V_{neg}$ .

The potential difference  $U_{neg}$  is expressed by:

$$U_{neg} = \phi_{neg} - \phi_e \quad (5.1)$$

While the potential difference  $V_{neg}$  is defined as:

$$V_{neg} = \phi_{neg} - \phi_{sei} \quad (5.2)$$

With:

$$\phi_{sei} = \phi_e + \frac{\delta_{sei}}{\kappa_{SEI}} i \quad (5.3)$$

$\delta_{SEI}$  being the SEI thickness and  $\kappa_{SEI}$ , its ionic conductivity.

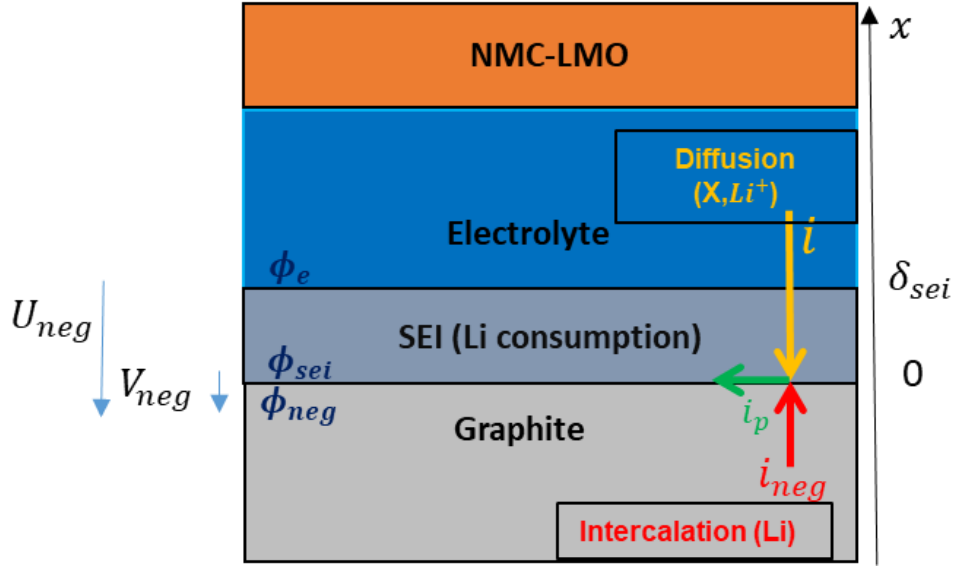


FIGURE V- 1: FULL CELL SCHEMATIC REPRESENTATION.

### V.1.2. SEI mechanisms and equations

There are three main mechanisms occurring inside the negative electrode of the battery. The principal mechanism is kinetic intercalation of the lithium-ion inside the graphite active material. The second and third mechanisms are the SEI growth resulting from the reduction of the solvent at the graphite/SEI interface and the parasitic consumption of the lithium-ions at the graphite/SEI surface.

#### V.1.2.1. Kinetic of intercalation of the lithium-ion :

The intercalation current  $i_{neg}$  is expressed using the Butler-Volmer equation [50]:

$$i_{neg} = i_o \left( \exp \left( \frac{\alpha F}{RT} \eta \right) - \exp \left( - \frac{(1 - \alpha) F}{RT} \eta \right) \right) \quad (5.4)$$

$i_o$  ( $A \cdot m^{-2}$ ) being the exchange current density,  $\alpha$  the symmetry factor associated with the intercalation reaction in the graphite,  $F$  ( $C \cdot mol^{-1}$ ) faradic constant,  $R$  ( $J \cdot K^{-1} \cdot mol^{-1}$ ) universal gas constant,  $T$  ( $K$ ) the temperature, and  $\eta$  ( $V$ ) the negative electrode overpotential.

This overpotential  $\eta$  (which is zero at equilibrium state) is defined as:

$$\eta = V_{neg} - E_{gr}^0 \quad (5.5)$$

where  $E_{gr}^0$  ( $V$ ) is the equilibrium potential of the graphite material.

Considering East. (5.1) -(5.3), the overpotential  $\eta$  can be rewritten as:

$$\eta = (\phi_{neg} - \phi_e) - \frac{\delta_{sei}}{\kappa_{SEI}} i - E_{gr}^0 = U_{neg} - \frac{\delta_{sei}}{\kappa_{SEI}} i - E_{gr}^0 \quad (5.6)$$

#### V.1.2.2. SEI growth model and the parasitic reaction of lithium-ions consumption

##### V.1.2.2.1 SEI growth model

The reduction of solvent at the interface graphite/SEI accelerates the growth of the SEI thickness, which is proportional to the flux density  $J$  ( $mol. m^{-2}. s^{-1}$ ) of component X, involved in a parasitic reaction, through the SEI surface:

$$\frac{\partial \delta_{SEI}}{\partial t} = n \frac{M_{sei}}{\rho_{sei}} J \quad (5.7)$$

Where  $n$  is the quantity of lithium consumed per mole of SEI formed,  $M_{SEI}$  the molar mass of SEI ( $g. mol^{-1}$ ) and  $\rho_{SEI}$  the density of SEI ( $kg. m^{-3}$ ).

A linear approximation is assumed for the solvent diffusion as no accumulation is supposed on the SEI layer [52]:

$$J = -\frac{D_x}{\delta_{SEI}} (C_x - C_x^0) \quad (5.8)$$

Where  $D_x$  ( $m^2. s^{-1}$ ) is the effective diffusion coefficient of X through the porous structure of the SEI,  $C_x$  ( $mol. m^{-3}$ ) the concentration of the solvent X at the interface graphite/SEI and  $C_x^0$  ( $mol. m^{-3}$ ) the concentration of X in the bulk of electrolyte.

##### V.1.2.2.2 Parasitic reaction of the Lithium-ion consumption

This reaction is supposed irreversible and the parasitic current density  $i_p$ , responsible for lithium-ions consumption, is modeled by Tafel's law [41] which depends on the concentration of the solvent X at the graphite/SEI interface:

$$i_p = F k_{sei} c_x \exp\left(-\frac{\alpha_c F}{RT} \eta_p\right) \quad (5.9)$$

The overpotential of the parasitic reaction  $\eta_p$  is given by:

$$\eta_p = V_{neg} - E_{SEI}^0 \quad (5.10)$$

Where  $E_{SEI}^0$  is the equilibrium potential associated with SEI formation.

By coupling Eq. (5.5) and Eq.(5.10), the overpotentials of the intercalation ( $\eta$ ) and parasitic ( $\eta_p$ ) reactions can then be linked by:

$$\eta_p = \eta + E_{gr}^0 - E_{sei}^0 \quad (5.11)$$

For the scope of this thesis, only the calendar aging of the cell battery is studied for which, the total electrical current  $I$  is equal to zero. Thus, the overpotential of the intercalation reaction  $\eta$  is also equal to zero as there is no intercalation of the lithium on the graphite. Using Eq. (5.11), the parasitic overpotential in calendar aging is defined by:

$$\eta_p = E_{gr}^0 - E_{sei}^0 \quad (5.12)$$

The parasitic current density  $i_p$  modeled by Tafel's law can be expressed by:

$$i_p = F k_{sei} C_x \exp \left( -\frac{\alpha_c F}{RT} (E_{gr}^0 - E_{sei}^0) \right) \quad (5.13)$$

The flux density  $J$ , representing the diffusion flux of the solvent through the SEI layer, can be related to the parasitic current ( $i_p$ ) density by:

$$J = \frac{i_p}{nF} \quad (5.14)$$

Considering the Fick diffusion of solvent Eq. (5.8), Eq. (5.14) becomes:

$$\frac{i_p}{nF} = -\frac{D_x}{\delta_{SEI}} (C_x - C_x^0) \quad (5.15)$$

$$i_p = -\frac{n F D_x}{\delta_{SEI}} (C_x - C_x^0) \quad (5.16)$$

The solvent concentration  $C_x$  is deduced from Eq.(5.16):

$$C_x = c_x^0 - \frac{\delta_{SEI}}{nFD_x} i_p \quad (5.17)$$

Combining Eqs. (5.13) and (5.17), the parasitic current  $i_p$  is given by:

$$i_p = \frac{F k_{sei} c_x^0 \exp \left( -\frac{\alpha_c F}{RT} (E_{gr}^0 - E_{sei}^0) \right)}{1 + \frac{k_{sei}}{n D_x} \exp \exp \left( -\frac{\alpha_c F}{RT} (E_{gr}^0 - E_{sei}^0) \right)} \delta_{SEI} \quad (5.18)$$

The parasitic electrical current flowing through S, the graphite surface considering during the parasitic reaction process, is linked to the parasitic current density by:

$$I_p = S * i_p \quad (5.19)$$

Therefore, the parasitic electrical current can be expressed by:

$$I_p = \frac{S F k_{sei} c_x^0 * \exp \left( -\frac{\alpha_c F}{RT} (E_{gr}^0 - E_{sei}^0) \right) ]}{1 + \frac{k_{sei}}{n D_x} \exp \left( -\frac{\alpha_c F}{RT} (E_{gr}^0 - E_{sei}^0) \right) \cdot \delta_{SEI}} \quad (5.20)$$

To find relationships between the parasitic electrical current  $I_p$  and the electrical currents flowing through the electrodes ( $I_{pos}$ ,  $I_{neg}$ ), the SEI and negative electrode illustrated in FIGURE V-1 are described by an equivalent electrical circuit (FIGURE V-2).  $R_{sei}$ ,  $R_{tc}$  and  $R_p$  are the electrical resistances related to the SEI layer, charge transfer, and parasitic reaction of cyclable lithium-ions consumption, respectively.

$I_{pos}$  and  $I_{neg}$  are the electrical currents flowing through the positive and negative electrodes.  $I$  is the total electrical current flowing through the cell and  $I_p$  the parasitic electrical current due to SEI growth. As illustrated in FIGURE V-2:

$$I + I_{neg} = I_p \Rightarrow I_{neg} = I_p - I \quad (5.21)$$

$$I_{pos} = I \quad (5.22)$$

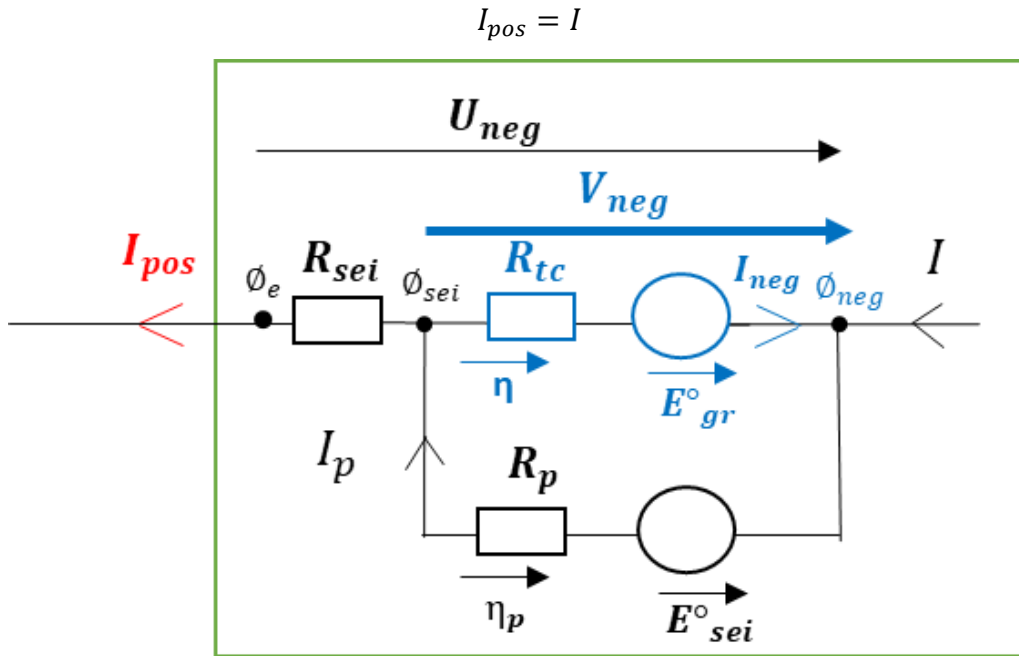


Figure V- 2: Electrical equivalent circuit of the SEI and negative electrode system.

The electrical current  $I_{neg}$  and  $I_{pos}$  can be related to the electrode's lithium contents  $\theta_{neg}$  and  $\theta_{pos}$ :

$$I_{pos} = -C_{pos} \frac{d\theta_{pos}}{dt} \quad (5.23)$$

$$I_{neg} = -C_{neg} \frac{d\theta_{neg}}{dt} \quad (5.24)$$

where  $\theta_{neg}$  and  $\theta_{pos}$  are the actual lithium contents corresponding to the amount of lithium inside the electrodes at the cell storage SOC (%). During the battery charge ( $I > 0$ ), the electrical currents  $I_{pos}$  and  $I_{neg}$  are respectively positive and negative because the positive electrode is delithiated (decrease of  $\theta_{pos}$ ) while the negative electrode is lithiated (an increase of  $\theta_{neg}$ ).

The minimum and maximum lithium content ( $\theta_{pos_{min}}, \theta_{pos_{max}}, \theta_{neg_{min}}, \theta_{neg_{max}}$ ) at a given aging state can be simulated using ( $C_{pos}, C_{neg}, OFS$ ) via the dual-tank OCV model (chapter 4, §. IV.1.1). Knowing the cell storage SOC (%), the actual lithium contents  $\theta_{neg}$  and  $\theta_{pos}$  can be calculated by:

$$\theta_{neg} = \theta_{neg_{min}} + (\theta_{neg_{max}} - \theta_{neg_{min}})SOC(\%) \quad (5.25)$$

$$\theta_{pos} = \theta_{pos_{max}} - (\theta_{pos_{max}} - \theta_{pos_{min}})SOC(\%) \quad (5.26)$$

As shown in [Figure V-2](#), the parasitic current  $I_p$  is driven by the  $\eta_p$  and thus by  $V_{neg}$ . Therefore, having access to the negative potential at the graphite/SEI interface is essential to know more about parasitic reactions inside the battery. For this reason, using a dual-tank OCV model is relevant to study the SEI growth as it allows using the graphite potential.

## V.2. Physics-based aging model

In this chapter, a physics-based aging model for the offset parameter ( $OFS$ ) is developed. It is based on the SEI growth model to consider the influence of loss of lithium inventory during calendar aging. The loss of active mass induced by the degradation of the electrodes is still considered considering an empirical approach. The same empirical aging laws developed in chapter 4 (§. IV.2.1) are considered.

### V.2.1. $OFS$ aging law

The electrode potential signals ( $V_{pos}, V_{neg}$ ) at a given state of aging are shown in [FIGURE V-3](#). The terms identified as “ $(1 - \theta_{pos})C_{pos}$ ” and “ $\theta_{neg}C_{neg}$ ” represent respectively the non-lithiated and lithiated capacity of the positive and negative electrode respectively at the cell storage SOC(%).

From this description, the offset parameter is linked to the positive and negative electrode capacities as well as the lithium content ( $\theta_{neg}, \theta_{pos}$ ):

$$OFS = (1 - \theta_{pos})C_{pos} - \theta_{neg}C_{neg} \quad (5.27)$$

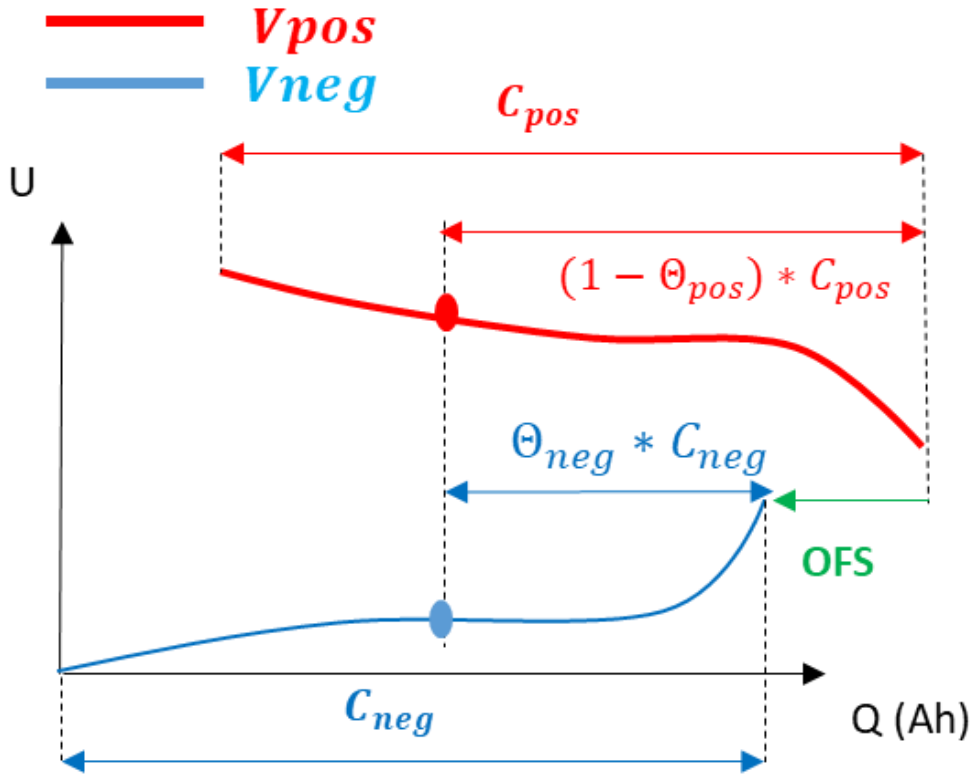


Figure V- 3: Positive and negative electrode potentials at a given state of charge and aging state.

To define the OFS aging law, the derivative of Eq. (5.27) is calculated:

$$\frac{dOFS}{dt} = - \left( \theta_{neg} \frac{dC_{neg}}{dt} + C_{neg} \frac{d\theta_{neg}}{dt} \right) + \left[ (1 - \theta_{pos}) \frac{dC_{pos}}{dt} - C_{pos} \frac{d\theta_{pos}}{dt} \right] \quad (5.28)$$

Introducing the current  $I_{neg}$  and  $I_{pos}$  via Eq.(5.23) and Eq.(5.24), the offset aging law  $\frac{dOFS}{dt}$  in Eq.(5.28) can be rewritten as follows:

$$\frac{dOFS}{dt} = - \left( \theta_{neg} \frac{dC_{neg}}{dt} - I_{neg} \right) + \left[ (1 - \theta_{pos}) \frac{dC_{pos}}{dt} + I_{pos} \right] \quad (5.29)$$

Considering Eqs. (5.21) and (5.22), the aging law  $\frac{dOFS}{dt}$  becomes:

$$\frac{dOFS}{dt} = - \left( \theta_{neg} \frac{dC_{neg}}{dt} - (I_p - I) \right) + \left[ (1 - \theta_{pos}) \frac{dC_{pos}}{dt} + I \right] \quad (5.30)$$

After simplifying:

$$\frac{dOFS}{dt} = I_p - \theta_{neg} \frac{dC_{neg}}{dt} + (1 - \theta_{pos}) \frac{dC_{pos}}{dt} \quad (5.31)$$

### V.2.2. Influence of degradation modes on the offset aging

This section details the evolution of the offset parameter between two aging states 'i' and 'i+1'. Three cases are considered where the cell experiences separately  $LLI$ ,  $LAM_{pos}$  and  $LAM_{neg}$  aging mechanisms.

#### V.2.2.1. Influence of $LLI$ on the offset parameter

The loss of lithium inventory ( $LLI$ ) is a shift of the negative electrode potential signal to the left as shown in **FIGURE V- 4(b)**. In calendar aging, the SEI formation leads to a decrease of the actual lithium content from  $\theta_{neg_i}$  to  $\theta_{neg_{i+1}}$  due to the lithium consumption at the SEI/Graphite interface. As the battery current,  $I$  is equal to zero, the actual lithium content at aging state 'i' for the positive electrode ( $\theta_{pos_i}$ ) remains the same at the aging state 'i+1'. As there is no loss of active mass either on the negative or positive electrode in the simulation illustrated in **FIGURE V- 4(a)**, both electrode capacities remain constant between the aging state 'i' and 'i+1'.

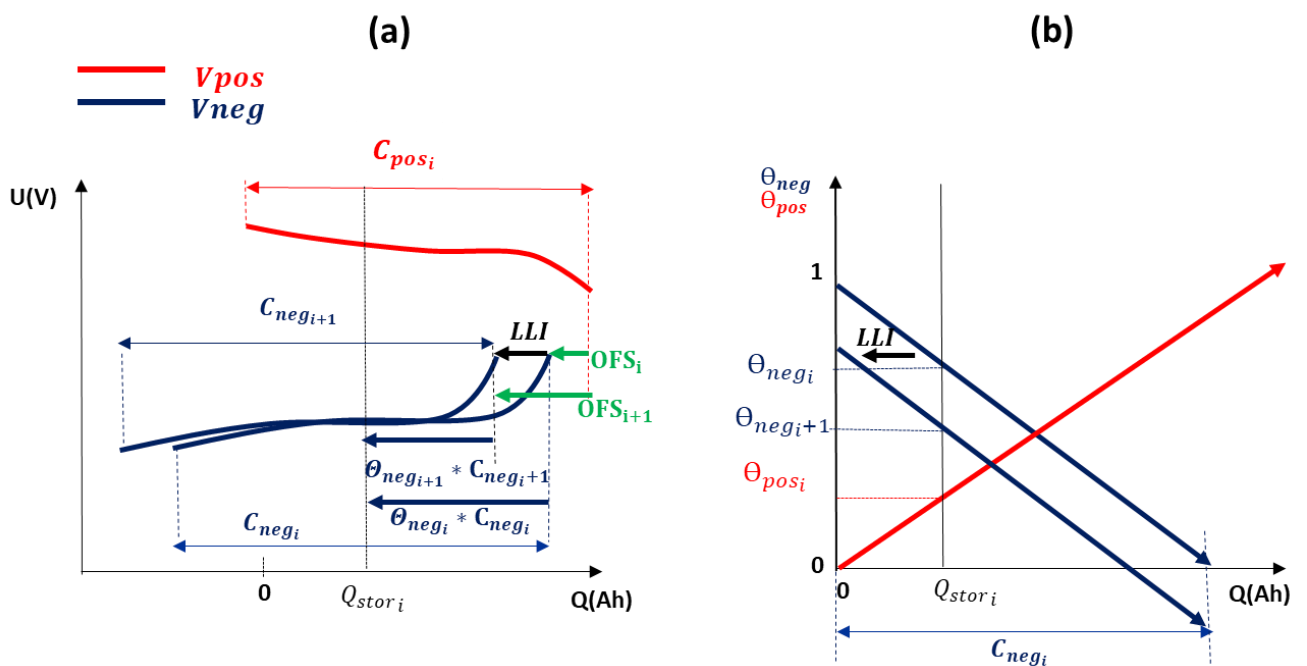


Figure V- 4: Influence of LLI on the offset aging.

In this aging conditions, the Eq. (5.31) simplifies as:

$$\frac{dOFS}{dt} = I_p \quad (5.32)$$

Considering Eqs. (5.21) and (5.22):

$$\frac{dOFS}{dt} = I_{neg} - I = I_{neg} - I_{pos} \quad (5.33)$$

As Eqs. (5.23) and (5.24) relate  $I_{pos}$  and  $I_{neg}$  to the actual lithium content  $\theta_{neg}$  and  $\theta_{pos}$ ,  $\frac{dOFS}{dt}$  can be rewritten:

$$\frac{dOFS}{dt} = -C_{neg} \frac{d\theta_{neg}}{dt} + C_{neg} \frac{d\theta_{pos}}{dt} \quad (5.34)$$

It is worth noting that the actual positive lithium content does not change with aging in this case, therefore, the derivative  $\frac{d\theta_{pos}}{dt}$  is equal to zero and Eq. (5.34) simplifies:

$$\frac{dOFS}{dt} = -C_{neg} \frac{d\theta_{neg}}{dt} \quad (5.35)$$

The discretization of Eq. 5.35 between the aging states 'i' and 'i+1', considering that the capacity  $C_{neg}$  is constant (equal to  $C_{neg_i}$ ) gives:

$$OFS_{i+1} = OFS_i + (\theta_{neg_i} - \theta_{neg_{i+1}}) * C_{neg_i} = OFS_i + \Delta LLI \quad (5.36)$$

In this first case, the offset aging is directly related to the increase of the cumulative loss of lithium inventory  $\Delta LLI$ , represented as the loss of lithium-ions during the insertion on the negative electrode.

#### V.2.2.2. Influence of the loss of active mass $LAM_{pos}$ on the offset parameter

The loss of active mass on the positive electrode corresponds to a shrinkage of the positive electrode potential signal as illustrated in [FIGURE V- 5\(a\)](#). This shrinkage is realized around the positive actual lithium content ([FIGURE V- 5\(b\)](#)) which does not change with aging. There is no loss of active mass on the negative electrode or  $LLI$  in the simulation illustrated in [FIGURE V- 5\(a\)](#).

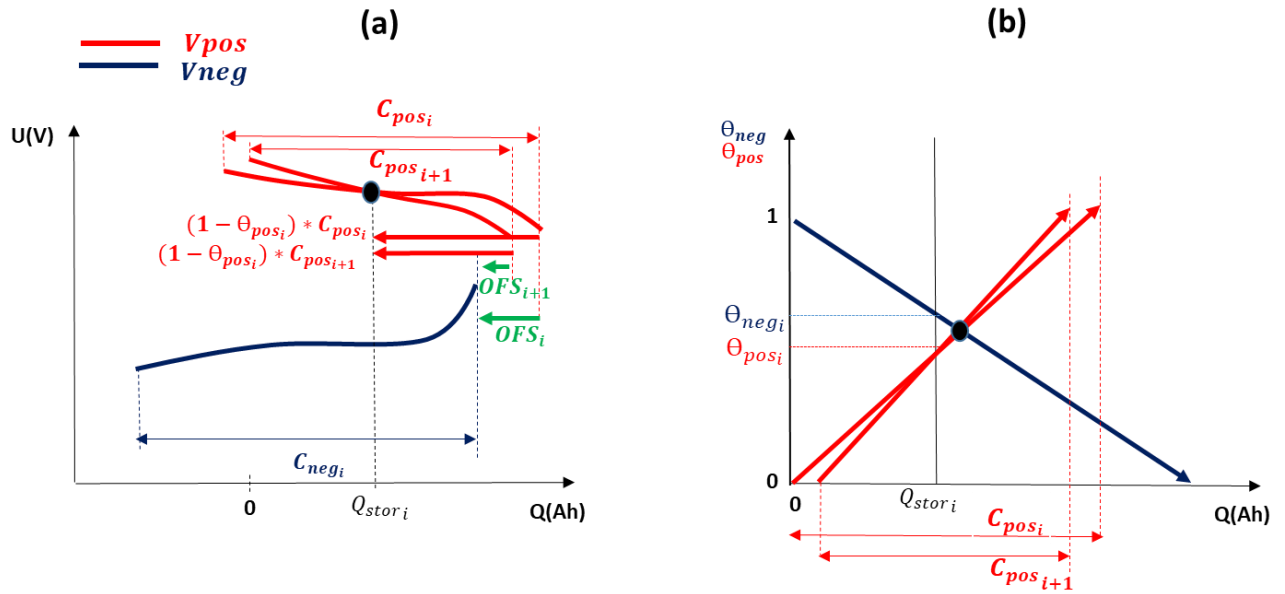


Figure V- 5: Influence of  $LAM_{pos}$  on the offset aging.

Using equation (5.31), the offset aging rate can be then expressed by:

$$\frac{dOFS}{dt} = (1 - \theta_{pos}) \frac{dC_{pos}}{dt} \quad (5.37)$$

As the actual positive lithium content does not evolve:

$$\theta_{pos} = \theta_{pos_i} \quad (5.38)$$

The discretization of Eq. (5.37) between the states 'i' and 'i+1' is given by:

$$OFS_{i+1} = OFS_i - (1 - \theta_{pos_i})(C_{pos_i} - C_{pos_{i+1}}) \quad (5.39)$$

In this second case, the offset change is directly related to the loss of non-lithiated active mass on the positive electrode, which decreases the offset parameter during aging.

#### V.2.2.3. Influence of the loss of active mass $LAM_{neg}$ on the offset parameter

As shown in FIGURE V- 6(a), the loss of active mass on the negative electrode corresponds to a shrinkage of the negative electrode signal around the negative lithium content  $\theta_{neg}$ . There is no loss of active mass on the positive electrode or  $LLI$  in the simulation illustrated FIGURE V- 6(a).

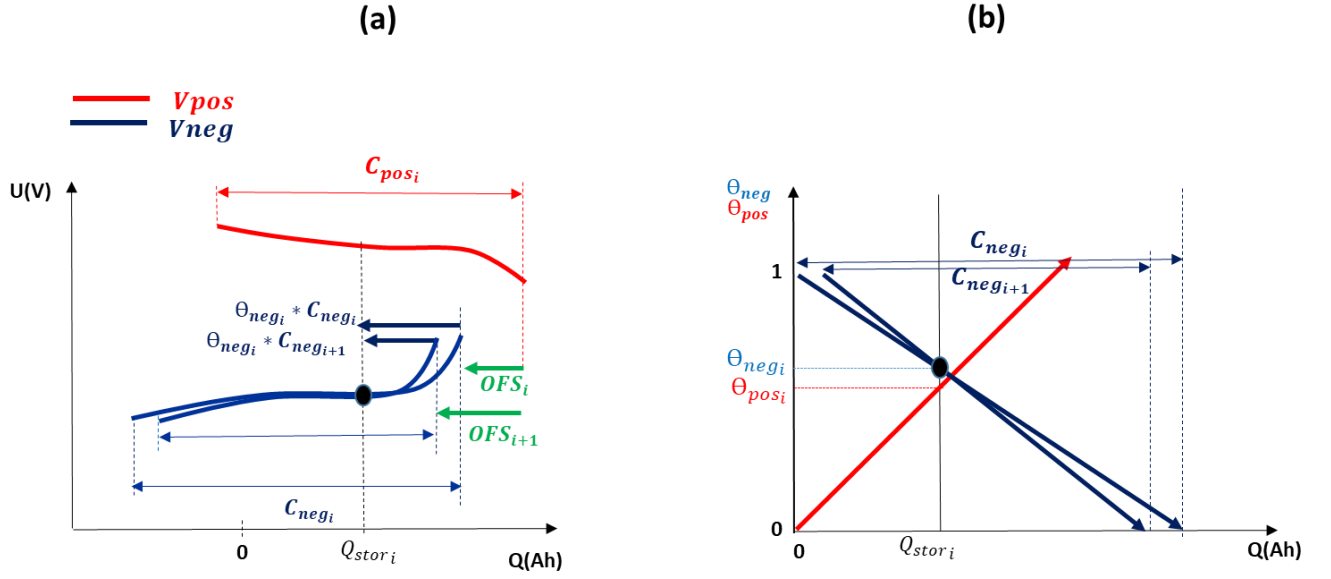


Figure V- 6: Influence of the LAM\_neg on the offset aging

Using equation (5.31), the offset aging rate can then be expressed by:

$$\frac{dOFS}{dt} = -\theta_{neg} \frac{dC_{neg}}{dt} \quad (5.40)$$

As the actual lithium content  $\theta_{neg}$  does not change with aging:

$$\theta_{neg} = \theta_{neg_i} \quad (5.41)$$

The discretization of Eq. (5.40) between the aging states 'i' and 'i+1' gives:

$$OFS_{i+1} = OFS_i + \theta_{neg_i} * (C_{neg_i} - C_{neg_{i+1}}) \quad (5.42)$$

In this third case, the offset change is directly related to the loss of lithiated active mass on the negative electrode, which increases the offset parameter during aging.

### V.2.3. Identification of the parameters of the physics-based aging model

The identification process is performed on the OFS parameter using the offset aging law described in Eq. (5.31). In this latter equation, the parasitic current  $I_p$  is given by Eq. (5.20). The influence of the temperature and SOC on the parasitic current is introduced below:

$$I_p = \frac{a_0(T) * \exp\left(-\frac{a_1}{T} (E_{gr}^0(SOC) - a_3)\right)}{1 + a_2(T) \exp\left(-\frac{a_1}{T} (E_{gr}^0(SOC) - a_3)\right)} * \delta_{SEI} \quad (5.43)$$

where parameters  $a_0$ ,  $a_2$  depend on the temperature and  $a_1$ ,  $a_3$  and  $a_4$  are some constant parameters.  $E_{gr}^0$ , the equilibrium potential depends on the cell storage SOC and thus the actual negative lithium content  $\theta_{neg}$  by using Eq. (5.25):

$$a_0(T) = S F k_{sei}(T) c_x^0 \quad (5.44)$$

$$(5.45)$$

$$a_1 = \frac{\alpha_c F}{R} \quad (5.46)$$

$$a_2(T) = \frac{k_{sei}(T)}{n D_x(T)} \quad (5.47)$$

$$a_3 = E_{sei}^0$$

Introducing Eqs. (5.14) and (5.19), the SEI growth model (Eq. (5.7)) gives the SEI thickness as a function of the parasitic current:

$$\frac{\partial \delta_{SEI}}{\partial t} = \frac{M_{sei}}{\rho_{sei} F S} I_p = a_4 * I_p \quad (5.48)$$

#### V.2.3.1. Identification method and results

As mentioned in §. 3.1.1, the dual-tank aging model for the positive and negative electrode capacities has already been set up in chapter 4 (§. IV.2.2). In this section only the parameters ( $a_0, a_1, a_2, a_3, a_4$ ) of  $I_p$  aging law (Eq.(5.43) and the SEI growth Eq.(5.48)) are identified in the offset aging law (Eq.(5.31)). This identification is performed by the optimization process as already explained in chapter 4 (§. IV.2.2).

The parameters  $a_0(T)$  and  $a_2(T)$  are identified at 4 breakpoints of temperature namely 0°C, 25°C, 45°C, and 60°C. Their values between the breakpoints of temperature are calculated using linear interpolation.

The identification results are summed up in Table V- 1 below:

Parameter	Unit	OFS
Initial value $OFS_{init}$	Ah	2.3
$a_0(T = 0^\circ C)$	A	1e-10
$a_0(T = 25^\circ C)$	A	9e-9
$a_0(T = 45^\circ C)$	A	2e-8
$a_0(T = 60^\circ C)$	A	5e-8
$a_1$	$C.J^{-1}.K$	151
$a_2(T = 0^\circ C)$	$mol^{-1}.m^{-1}$	9e-5
$a_2(T = 25^\circ C)$	$mol^{-1}.m^{-1}$	1e-5
$a_2(T = 45^\circ C)$	$mol^{-1}.m^{-1}$	4.08
$a_2(T = 60^\circ C)$	$mol^{-1}.m^{-1}$	5.17
$a_3$	V	0.95
$a_4$	$C.mm$	1.6e-7

TABLE V- 1:  $I_p$  AND SEI GROWTH AGING MODEL PARAMETERS IDENTIFICATION.

The parameters  $a_0$  and  $a_2$  increase with temperature as illustrated in FIGURE V- 7. In fact, the parasitic current is higher at high temperature as more lithium are consumed on the graphite/SEI interface.

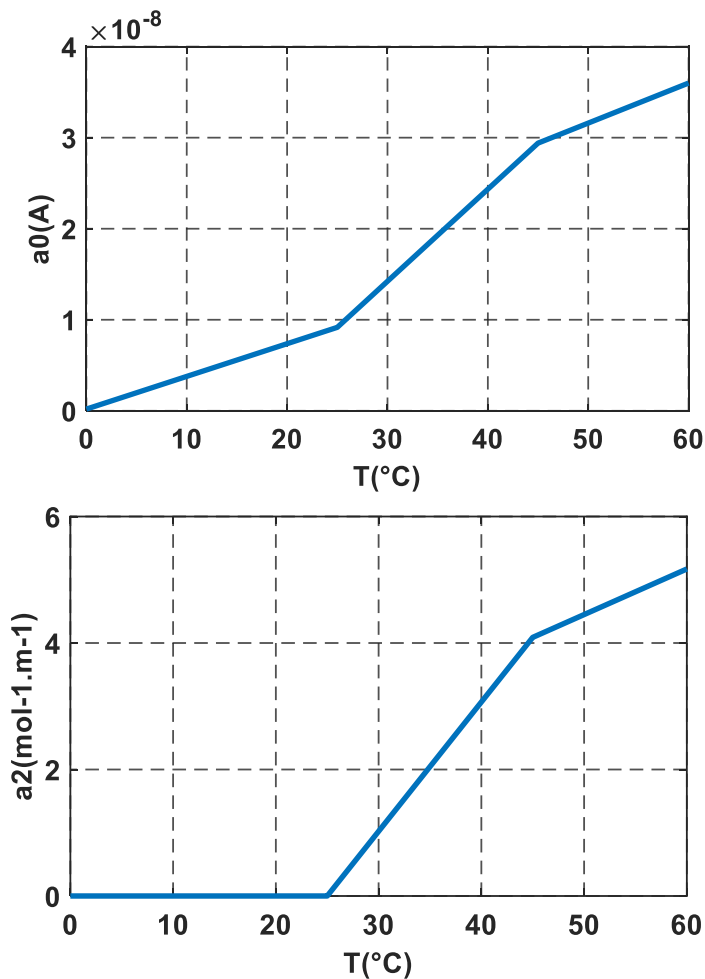


Figure V- 7: Evolution of aging parameters  $a_0$  and  $a_2$  with temperature.

The evolution of the offset with storage time is shown in [FIGURE V- 8](#). The initial value identified for the offset is 2.3Ah. The simulated offset is not so far from the offset data identified (in chapter 4, §. IV.1.2.2.3 ) especially at 0°C, 25°C and 45°C with a maximum error of up to 20%. The results are worst at temperature 60°C and SOC 80%, where the identified offset parameter (chapter 4, §. IV.1.2.2.3) does not follow a  $\sqrt{t}$  trend. In general, the identification has not been improved at temperatures 45°C (SOC 0% and 30%) and 60°C (SOC 80%). This can be a hint that all physical reactions at the SEI/electrolyte interface have not been considered.

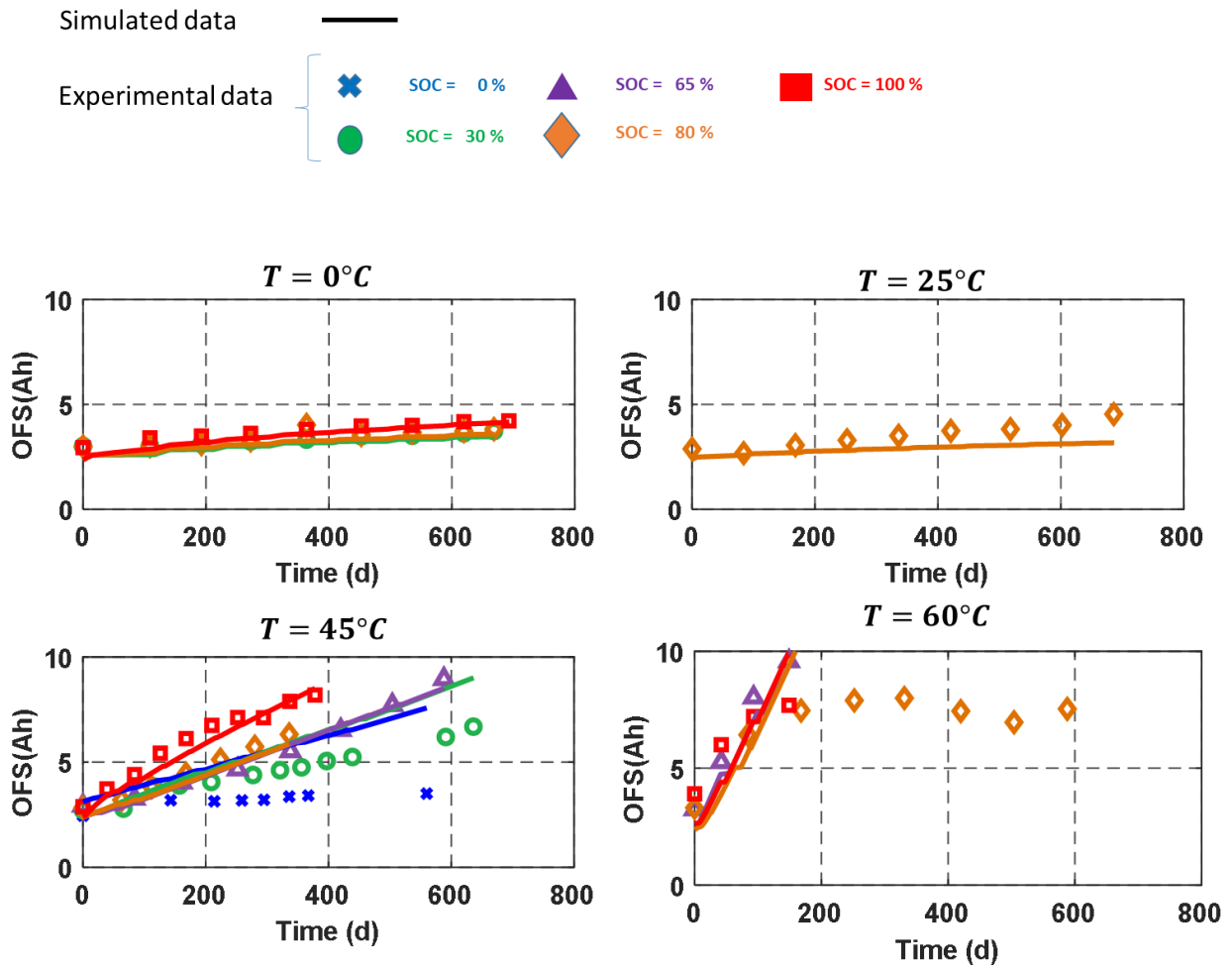


Figure V- 8: Calendar aging identification of the offset (OFS) parameter.

### V.2.3.2. SEI thickness growth

The identification of the parameters  $a_i$  allows simulating the SEI thickness growth (Eq. (5.48)) as a function of the calendar aging condition. The results are shown in Figure V- 9. The initial thickness is not the same for some calendar aging conditions as the cells were not stored at the same temperature and SOC conditions before starting the calendar aging campaign (see chapter 2, §. II.3).

The SEI growth at 0°C is not noticeable whatever the SOC.

At an ambient temperature of 25°C, the rate of SEI growth is like the trend at 0°C with an increase of approximately 30% from its initial value to reach  $\approx 400\text{nm}$  in less than 2 years of storage. This result is physically feasible since the SEI thickness in the literature reaches approximately a few hundred nanometers [85].

At higher temperatures, the SEI growth accelerates:

- At 45°C, the SEI thickness increases fast especially at high SOC (65% to 100%).
- At 60°C, the SEI growth is the highest at SOC 65% and 100% which are the most damaging conditions for the cell capacity fade.

In general, the evolution of the SEI thickness growth is mainly linear which means that the SEI growth is not limited yet by solvent diffusion.

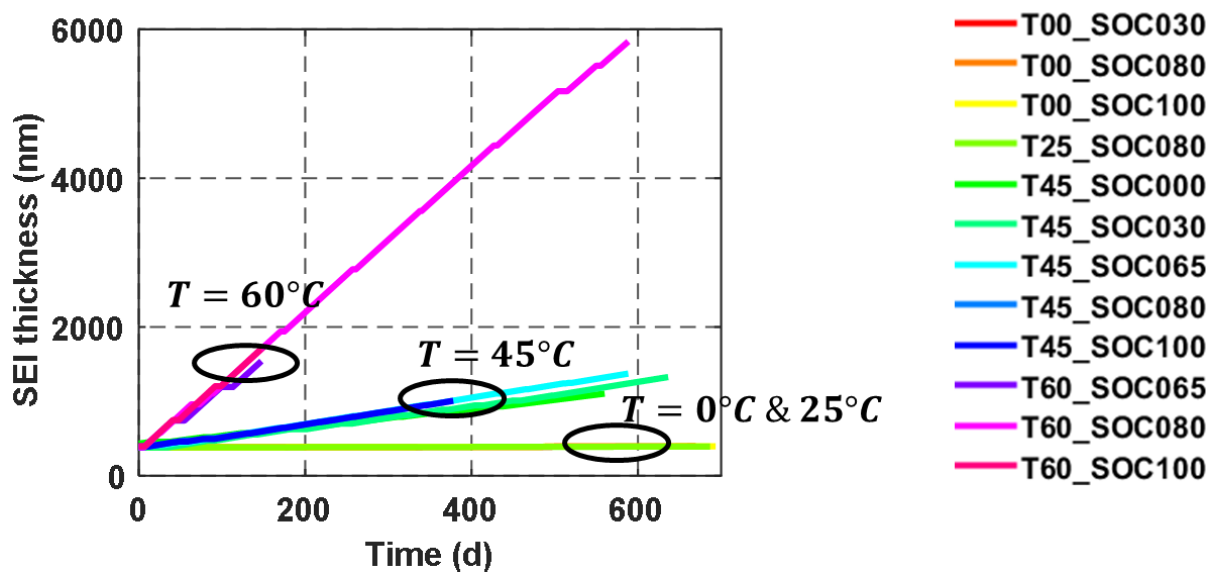


Figure V- 9: SEI thickness growth on calendar aging.

#### V.2.4. Aging evolution of the parameters of the physics-based aging model

The physics-based aging model is used to simulate the calendar condition at temperature 45°C and SOC 65%, adding some elements to the reference case study in chapter 4 (§. IV.3.1).

The §V.2.4.1 follows the electrode potential signals ( $V_{pos}, V_{neg}$ ) while the §V.2.4.2 depicts the evolution of the actual lithium contents ( $\theta_{neg}, \theta_{pos}$ ) along with aging, when the battery is stored at different initial SOC.

##### V.2.4.1. Evolution of the electrode potential signals with aging

The evolution of the electrode potential signals, at beginning-of-life and after 700 days of storage, for a calendar condition at ( $T= 45^\circ\text{C}$ ,  $\text{SOC}=65\%$ ), is shown in **FIGURE V- 10**. The dashed lines correspond to a simulation at BOL (state 1) while the solid lines correspond to a simulation after 700 days of storage (state 2).

As shown in **FIGURE V- 10**, at SOC 65%, the actual negative potential increases along with aging from  $V_{neg\theta_1}$  to  $V_{neg\theta_2}$ .

On the positive electrode, the positive signal is shrunk around the actual SOC at 65%. Thus, the actual positive potential remains steady ( $V_{pos\theta_1} = V_{pos\theta_2}$ ).

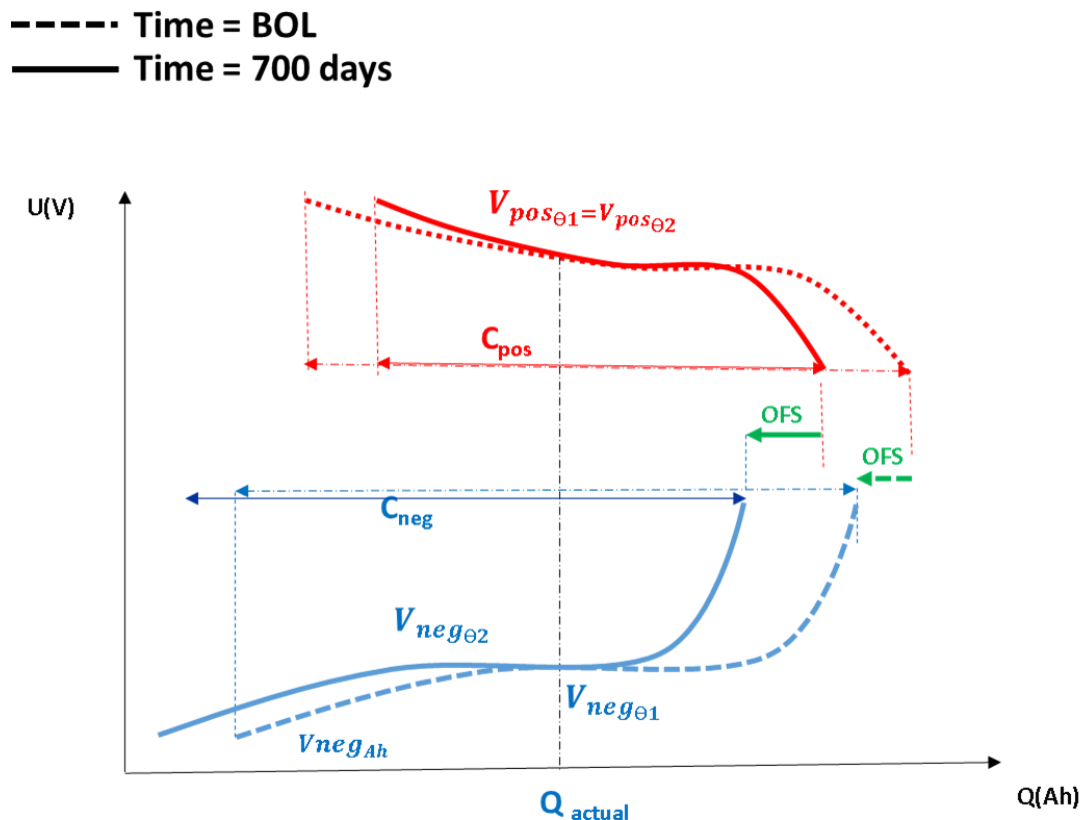


Figure V- 10: Evolution of the electrode potential signals after 700 days of pure calendar aging.

Storing the battery at different SOC at BOL (initial SOC), the physics-based aging is used to simulate the evolution of the actual lithium contents ( $\theta_{neg}$ ,  $\theta_{pos}$ ) along with aging, as illustrated in Figure V- 11. The actual electrode potentials  $V_{neg\theta}$  increases along with aging but  $V_{pos\theta}$  stays unchanged, as shown in FIGURE V- 10. Therefore, the actual lithium content on the negative electrode continuously decreases along with aging while it remains the same on the positive electrode through the whole simulation, as illustrated in Figure V- 11. In addition, the simulation also shows that the actual content in the negative electrode decreases progressively when the initial storage SOC of the battery escalates from 40% to 100%.

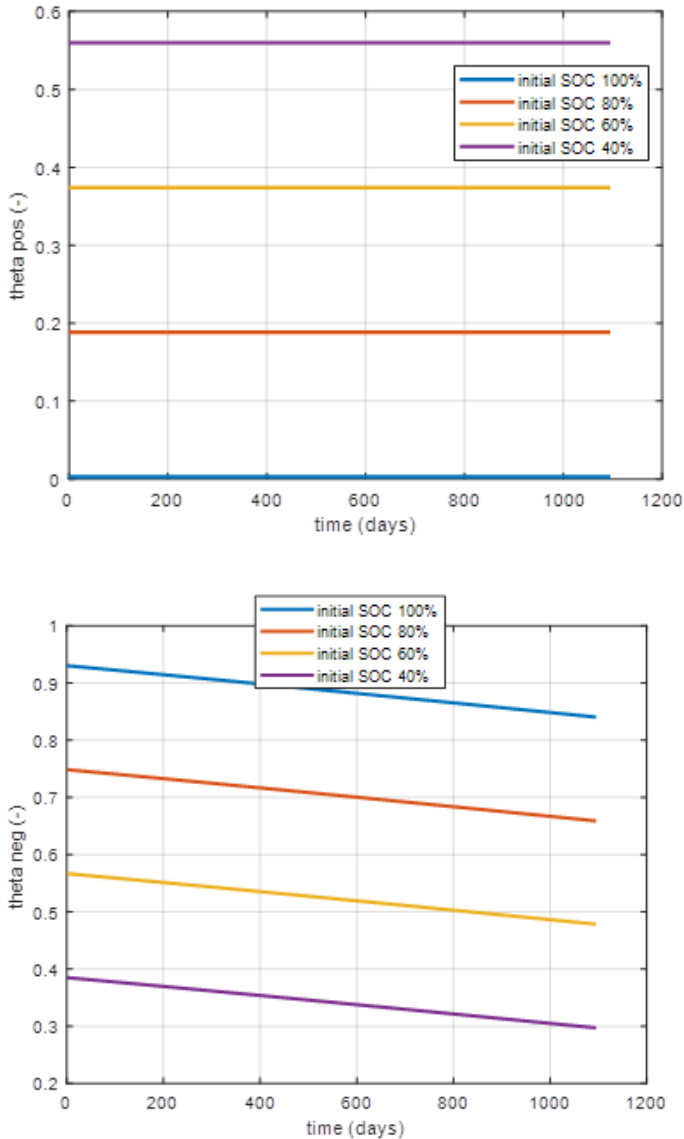
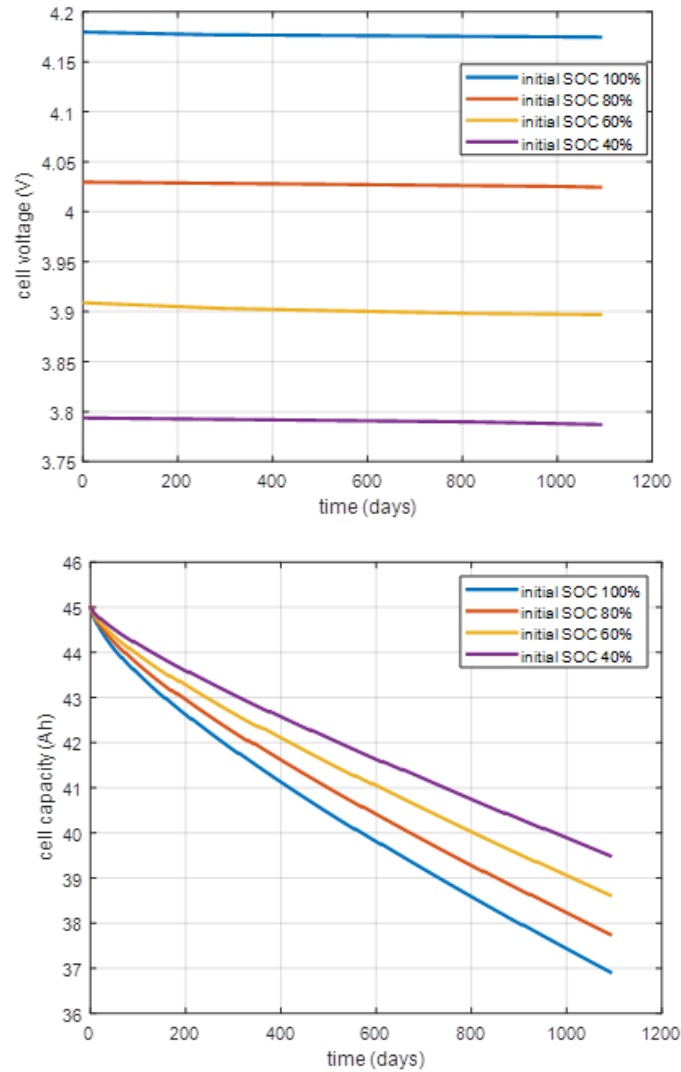


Figure V- 11: Evolution of the actual electrode lithium contents in the positive and negative electrode, starting from different initial SOC s (from 40% to 100%).

#### V.2.4.2. Evolution of the cell voltage and capacity with aging

As shown in **Figure V- 12**, the cell voltage decreases along with aging due to the evolution of the electrode potential signals previously depicted in **Figure v- 10**. This trend is particularly accentuated with the initial storage SOC increases from 40% to 100%. As a result, the simulation in **Figure V- 12** shows that the cell capacity of the Li-ion battery increasingly falls at higher SOC.



**Figure V- 12: Evolution of the cell voltage and capacity with aging, starting from different initial SOC s (from 40% to 100%).**

#### V.2.5. Validation of the physics-based aging model and comparison with the one-tank aging model

The same method described in chapter 4 (§. IV.2.3) is used to validate the physics-based aging model. The aging conditions used in chapter 4 (§. IV.2.3) for the aging model validation are simulated in this chapter: the variable SOC condition at 45°C and the thermal cycling condition at SOC 65% and SOC 100%. The validation of the physics-based aging model presented in [FIGURE V-13](#) shows a very good match between the experimental data and simulated ones for variable SOC condition (maximum error of 0.6%) and thermal cycling SOC 100% (maximum error of 1.4%). The thermal cycling prediction at SOC 65% is less good between 200 days and 600 days of storage (maximum error of 12%).

The validation results for the one-tank aging model are presented as well in [FIGURE V-13](#). It can be noticed that the overall error between experimental and simulated values decreases when using a physic-based aging model. By considering the influence of SEI thickness growth and loss of active mass on the offset parameter, the prognosis with the physic-based aging model has been improved compared to the one-tank aging model.

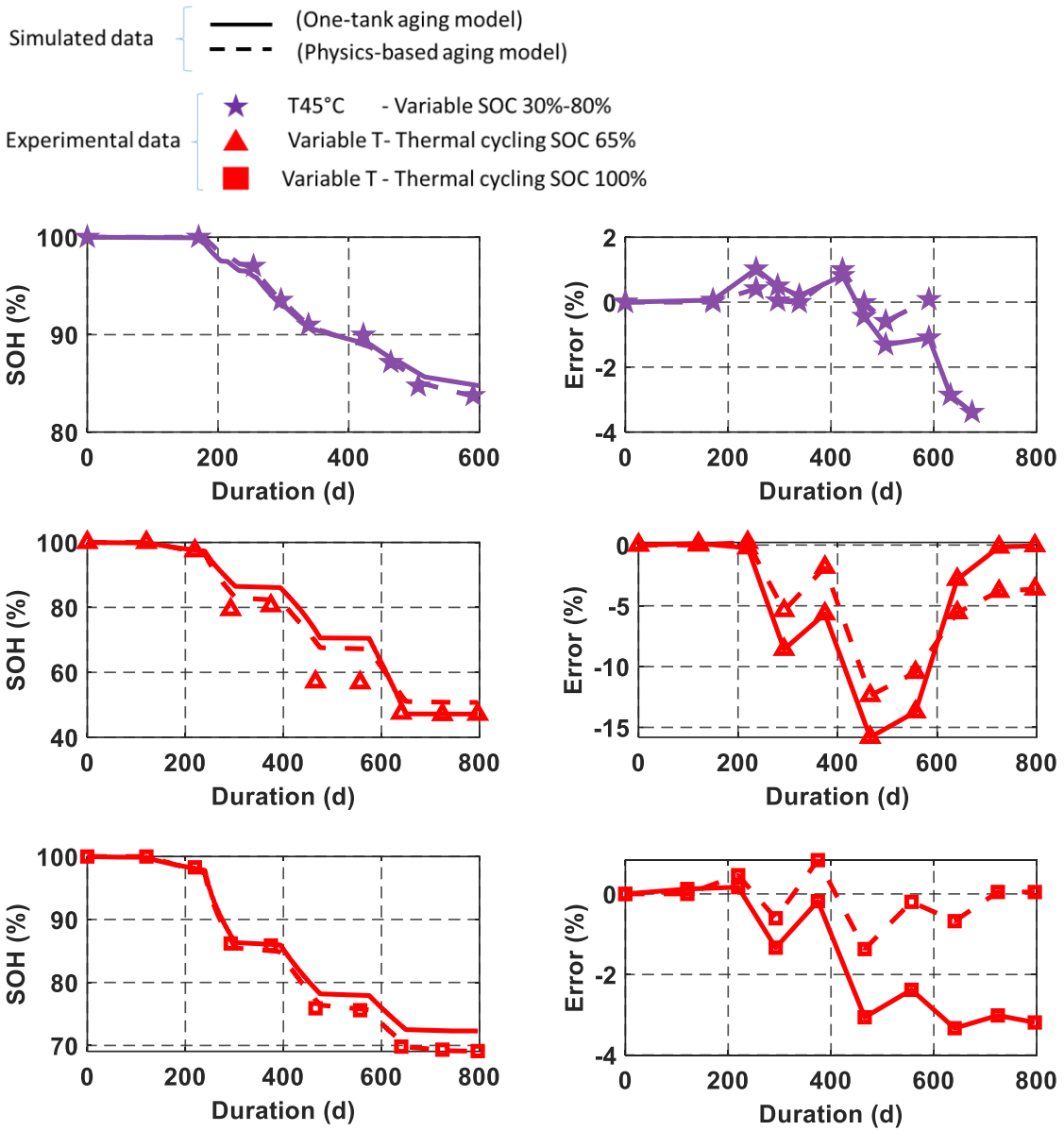


FIGURE V- 13: VALIDATION OF THE PHYSICS-BASED AGING MODEL (COMPARISON WITH ONE TANK-AGING MODEL).

## Conclusion:

The dual-tank aging model developed in chapter 4 showed satisfactory results for the SOH prediction on production lithium-ion batteries. In this chapter, this former dual-tank aging model was modified to add a physical approach to the one depicted in chapter 4 for the SOH prognosis. This physics-based aging model accounts for the lithium ions consumption due to the SEI growth. The lithium-ions consumption is related to the SEI formation/growth at the interface graphite/SEI and is represented by a parasitic current  $i_p$  given by a Tafel's law. This latter is used to express the SEI growth along with aging. The aging models for the electrode capacity loss had already been described in chapter 4 (§. IV.2.1).

The identification process of the physics-based aging model showed that the simulated offset parameter matches the data identified in chapter 4 (§. IV.1.2.2.3). The maximum error was approximatively 20% and the results have not been improved at temperatures 45°C (SOC 0% and 30%) and 60°C (SOC 80%).

The physics-based aging model for the OFS parameter allowed to follow the evolution of the SEI thickness growth on the graphite/SEI interface depending on the calendar aging conditions. The growth of SEI thickness was barely noticeable at low temperature (0°C and 25°C) but increased fast at higher temperature 45°C and 60°C especially for the SOC ranging from 65% and 100%. The SEI thickness had a linear evolution through aging, showing that the SEI growth is not limited by the solvent diffusion yet.

The study showed as well that the evolution of the parameters of the dual-tank OCV model led to the reduction of the lithium content in the negative electrode while the positive lithium content did not change. In addition, the evolution of the electrode potential signals led to the reduction of the cell voltage (and capacity) above all when the initial storage SOC of the battery increased from 40% to 100%.

Finally, the validation of the physics-based aging model showed very good results for two calendar aging conditions (variable SOC between 30% and 80% and thermal cycling at SOC 100%) with a maximum error of 0.6% and 1.4% respectively. The results were less good for the thermal cycling at SOC 65% with a maximum error of 12%. Nevertheless, the SOH prognosis of the production cell was slightly improved compared to the one-tank aging model. This improvement could be explained by the dissociation of the three contributions on the offset aging (loss of lithium inventory and loss of active mass on the electrodes).

## GENERAL CONCLUSION AND PERSPECTIVES

### VI.1. General conclusion

The main objectives of this Ph.D. thesis work were to develop new approaches for the prognosis of lithium-ion batteries state-of-health (SOH) while considering the influence of the operating conditions applied to the battery. This study was based on semi-empirical and physics-based models and aimed at predicting more accurately the Open-Circuit Voltage as well as the capacity changes of a production Li-ion battery.

Based on the state-of-art of the aging of Li-ion batteries, several degradation modes have been listed leading to a loss of performance of the battery. Based on this literature review, the one-tank aging model and especially the dual-tank aging model has been identified as a reliable tool for the prognosis of the battery SOH.

For this Ph.D. thesis work, experimental results from the MOBICUS project, a French national project were used. The aim of this latter project was to develop a semi-empirical aging model for the prognosis of the battery state-of-health. The experimental results of the aging campaign gave the evolution of the cell capacity for various calendar and cycling aging conditions.

A comparison between the aging model developed during the MOBICUS project and the one-tank aging model, a prognosis model based on the cell capacity, developed during this Ph.D. thesis work, was done. The results showed that the developed one-tank aging model was enhanced compared to the aging model developed during the MOBICUS project by the CEA team. The one-tank aging model was able to consider more precisely the influence of the SOC on the capacity aging, especially at high temperature (60°C) and for SOC below 50%.

To overcome the issue faced with this first approach, the development of the dual-tank aging model was performed. This aging model predicted the evolution of the cell capacity using a dual-tank OCV model and considering the operating conditions applied to the battery during calendar aging. Three parameters are used to define the dual-tank OCV model: the positive electrode capacity ( $C_{pos}$ ), the negative electrode capacity ( $C_{neg}$ ) and the offset between the electrode potential signals ( $OFFS$ ). The dual-tank aging model is based on a prognosis of these three variables (considered as an independent) for the capacity change. The identification results for the positive electrode ( $C_{pos}$ ) and the negative electrode ( $C_{neg}$ ) aging models agreed with the experimental ones with a maximum error of respectively 2% and 4%. The maximum error is higher for the offset parameter with a value of 20%. Following the identification process, the dual-tank aging model was validated using calendar conditions at variable SOC and thermal cycling at SOC 100%. The maximum error was below 4% between the experimental and simulated cell capacity. Finally, the dual-tank aging model was used to simulate the evolution of the electrode potential signals, parameters of the dual-tank OCV model ( $C_{pos}$ ,  $C_{neg}$ ,  $OFFS$ ) along with aging. A sensitivity analysis was performed and showed that the aging of ( $C_{pos}$ ,  $C_{neg}$ ,  $OFFS$ ) affected the evolution of the maximum and minimum lithium contents of both electrodes ( $\theta_{posmax}$ ,  $\theta_{negmax}$ ,  $\theta_{posmin}$ ,  $\theta_{negmin}$ ).

Finally, the development of a physics-based aging model for the *OFS* parameter was proposed. This physics-based aging model was related to the SEI growth on the graphite electrode introducing a parasitic current  $i_p$ , given by Tafel's law and considering the solvent diffusion and lithium consumption. The physics-based aging model for the *OFS* parameter allowed to follow the evolution of the SEI thickness and confirmed that the SEI thickness increases with temperature. The main advantage of the physics-based model was its capability of dissociating the contribution of the degradation modes ( $LLI, LAM_{neg}, LAM_{pos}$ ) depicted in the literature on the evolution of the *OFS*. In fact, the empirical dual-tank aging model developed in the Ph.D. thesis was only able to simulate separately the evolution of  $C_{pos}, C_{neg}, OFS$ . With this latter approach, the physics-based aging model was able to analyze the influence of the degradation routes of  $C_{pos}$  and  $C_{neg}$  and the contribution of loss of lithium inventory on the *OFS* parameter. The simulations showed that the lithium loss inventory and lithiated loss of active mass on the negative electrode increase the *OFS* while the loss of active mass on the positive electrode decreases the *OFS* parameter.

## VI.2. Perspectives

### VI.2.1. Dual-tank OCV model: hysteresis effect and validation of the identification process

The dual-tank OCV model presented in chapter 4 (§. IV.1.1) did not consider the hysteresis effect highlighted in the literature[86]. The voltage signals at C/10 used for the identification of the parameters ( $C_{pos}, C_{neg}, OFS$ ) were considered as OCV signals by averaging the measured charge and discharge curves. The dual-tank OCV model was only parametrized with three parameters ( $C_{pos}, C_{neg}, OFS$ ) but some authors in the literature have developed a dual-tank OCV model and considered another term identified as the battery overpotential [65].

Additional measurements of Open-Circuit Voltage data measured either by GITT method or voltages measurements at lower C-rates ( $\leq C/10$ ) should also be performed for the identification of ( $C_{pos}, C_{neg}$ ) at different aging states. The positive and negative electrodes at these aging states should as well be experimentally measured by coin cells made via the harvested electrodes at the different aging states. This way, the identification process of the parameters of the positive and negative electrodes ( $C_{pos}, C_{neg}$ ) could be validated depending on the method used for measuring the OCV. The influence of the C-rate identification process could be verified as well. Possibly for some C-rates, defining an overpotential term in the dual-tank OCV model would be unnecessary.

### VI.2.2. Dual-tank aging model: Effect of temperature and state-of-charge

The dual-tank aging model developed in chapter 4 (§. IV.2) considers the influence of the coupling effect of the temperature and state-of-charge with an activation energy  $E_a(SOC)$  depending on the state-of-charge. Some hypotheses were made to calibrate the activation energy  $E_a(SOC)$  for some state-of-charges due to lack of experimental data especially at SOC 0% and SOC 65%. Additional aging tests could improve the identification process and the prognosis of the battery capacity fade.

### VI.2.3. Physics-based aging model: modeling of the active mass loss on the electrodes

In this Ph.D. thesis work, a physics-based aging model of the offset parameter was modeled via the SEI growth model. It would be interesting to develop a physics-based aging model accounting for the active mass on the positive and negative electrodes as there are few models presented in the literature [51].

### VI.2.4. Physics-based aging model: Introduction of other mechanisms for the SEI

The results in in chapter 5 (§. V.2.3.1) show that the physics-based aging model failed to correctly predict the evolution of the offset parameter at 45°C (at SOC 0% & 30%) and 60°C (at SOC 80%). The reactions at graphite/SEI interface considered for this Ph.D. work might not be fully sufficient to model to OFS aging. Other's mechanisms such as the SEI breakage at the SEI/electrolyte side might be interesting to add in this study. This is relevant especially using LMO type because of the Manganese dissolution which can contaminate the anode side.

## REFERENCES

- [1] « Is Li-ion the Solution for the Electric Vehicle? – Battery University ». [https://batteryuniversity.com/learn/archive/is\\_li\\_ion\\_the\\_solution\\_for\\_the\\_electric\\_vehicle](https://batteryuniversity.com/learn/archive/is_li_ion_the_solution_for_the_electric_vehicle) (consulté le nov. 03, 2020).
- [2] P. Gyan et R. Sas, « MOBICUS PROJECT : BATTERY AGEING MODELS AND DURABILITY ASSESSMENT WITH THERMAL MANAGEMENT STRATEGIES », p. 34, 2017.
- [3] J. Vetter *et al.*, « Ageing mechanisms in lithium-ion batteries », *Journal of Power Sources*, vol. 147, n° 1-2, p. 269-281, sept. 2005, doi: 10.1016/j.jpowsour.2005.01.006.
- [4] Y. Cui *et al.*, « Multi-stress factor model for cycle lifetime prediction of lithium ion batteries with shallow-depth discharge », *Journal of Power Sources*, vol. 279, avr. 2015, doi: 10.1016/j.jpowsour.2015.01.003.
- [5] T. Yoshida *et al.*, « Degradation Mechanism and Life Prediction of Lithium-Ion Batteries », *J. Electrochem. Soc.*, vol. 153, n° 3, p. A576-A582, janv. 2006, doi: 10.1149/1.2162467.
- [6] P. Ramadass, B. Haran, P. M. Gomadam, R. White, et B. N. Popov, « Development of First Principles Capacity Fade Model for Li-Ion Cells », *J. Electrochem. Soc.*, vol. 151, n° 2, p. A196-A203, janv. 2004, doi: 10.1149/1.1634273.
- [7] S.-H. Kang, D. P. Abraham, A. Xiao, et B. L. Lucht, « Investigating the solid electrolyte interphase using binder-free graphite electrodes », *Journal of Power Sources*, vol. 175, n° 1, p. 526-532, janv. 2008, doi: 10.1016/j.jpowsour.2007.08.112.
- [8] E. Sarasketa-Zabala, F. Aguesse, I. Villarreal, L. M. Rodriguez-Martinez, C. M. López, et P. Kubiak, « Understanding Lithium Inventory Loss and Sudden Performance Fade in Cylindrical Cells during Cycling with Deep-Discharge Steps », *The Journal of Physical Chemistry C*, vol. 119, n° 2, p. 896-906, janv. 2015, doi: 10.1021/jp510071d.
- [9] M.-T. F. Rodrigues, K. Kalaga, S. E. Trask, I. A. Shkrob, et D. P. Abraham, « Anode-Dependent Impedance Rise in Layered-Oxide Cathodes of Lithium-Ion Cells », *J. Electrochem. Soc.*, vol. 165, n° 9, p. A1697-A1705, 2018, doi: 10.1149/2.0611809jes.
- [10] T. Waldmann, B.-I. Hogg, et M. Wohlfahrt-Mehrens, « Li plating as unwanted side reaction in Production Li-ion cells », *Journal of Power Sources*, vol. 384, p. 107-124, 2018, doi: 10.1016/j.jpowsour.2018.02.063.
- [11] D. Ren *et al.*, « Investigation of Lithium Plating-Stripping Process in Li-Ion Batteries at Low Temperature Using an Electrochemical Model », *J. Electrochem. Soc.*, vol. 165, n° 10, p. A2167-A2178, 2018, doi: 10.1149/2.0661810jes.
- [12] G. Liu et W. Lu, « A Model of Concurrent Lithium Dendrite Growth, SEI Growth, SEI Penetration and Regrowth », *Journal of The Electrochemical Society*, vol. 164, n° 9, p. A1826-A1833, 2017, doi: 10.1149/2.0381709jes.
- [13] L. Yang, M. Takahashi, et B. Wang, « A study on capacity fading of lithium-ion battery with manganese spinel positive electrode during cycling », *Electrochimica Acta*, vol. 51, n° 16, p. 3228-3234, avr. 2006, doi: 10.1016/j.electacta.2005.09.014.
- [14] M. Ochida *et al.*, « Influence of Manganese Dissolution on the Degradation of Surface Films on Edge Plane Graphite Negative-Electrodes in Lithium-Ion Batteries », *J. Electrochem. Soc.*, vol. 159, n° 7, p. A961-A966, janv. 2012, doi: 10.1149/2.031207jes.

- [15] E. Wang, D. Ofer, W. Bowden, N. Ilchev, R. Moses, et K. Brandt, « Stability of Lithium Ion Spinel Cells. III. Improved Life of Charged Cells », *J. Electrochem. Soc.*, vol. 147, n° 11, p. 4023-4028, janv. 2000, doi: 10.1149/1.1394013.
- [16] C. Delacourt *et al.*, « Effect of Manganese Contamination on the Solid-Electrolyte-Interphase Properties in Li-Ion Batteries », *J. Electrochem. Soc.*, vol. 160, n° 8, p. A1099-A1107, janv. 2013, doi: 10.1149/2.035308jes.
- [17] M. Dubarry et B. Y. Liaw, « Identify capacity fading mechanism in a Production LiFePO<sub>4</sub> cell », *Journal of Power Sources*, vol. 194, n° 1, p. 541-549, oct. 2009, doi: 10.1016/j.jpowsour.2009.05.036.
- [18] J. Zhu *et al.*, « Investigation of lithium-ion battery degradation mechanisms by combining differential voltage analysis and alternating current impedance », *Journal of Power Sources*, vol. 448, p. 227575, févr. 2020, doi: 10.1016/j.jpowsour.2019.227575.
- [19] C. R. Birkel, M. R. Roberts, E. McTurk, P. G. Bruce, et D. A. Howey, « Degradation diagnostics for lithium ion cells », *Journal of Power Sources*, vol. 341, p. 373-386, févr. 2017, doi: 10.1016/j.jpowsour.2016.12.011.
- [20] F. Baronti, R. Saletti, et W. Zamboni, « Open Circuit Voltage of Lithium-ion batteries for energy storage in DC microgrids », in *2015 IEEE First International Conference on DC Microgrids (ICDCM)*, juin 2015, p. 343-348, doi: 10.1109/ICDCM.2015.7152066.
- [21] A. Farmann et D. U. Sauer, « A study on the dependency of the open-circuit voltage on temperature and actual aging state of lithium-ion batteries », *Journal of Power Sources*, vol. 347, p. 1-13, avr. 2017, doi: 10.1016/j.jpowsour.2017.01.098.
- [22] M. Petit, E. Prada, et V. Sauvant-Moynot, « Development of an empirical aging model for Li-ion batteries and application to assess the impact of V2G strategies on battery lifetime », *Applied Energy*, vol. 172, n° June, p. 398–407, 2016, doi: 10.1016/j.apenergy.2016.03.119.
- [23] P. Khumprom et N. Yodo, « A Data-Driven Predictive Prognostic Model for Lithium-ion Batteries based on a Deep Learning Algorithm », *Energies*, vol. 12, n° 4, Art. n° 4, janv. 2019, doi: 10.3390/en12040660.
- [24] L. Wang, D. Lu, Q. Liu, L. Liu, et X. Zhao, « State of charge estimation for LiFePO<sub>4</sub> battery via dual extended kalman filter and charging voltage curve », *Electrochimica Acta*, vol. 296, p. 1009-1017, févr. 2019, doi: 10.1016/j.electacta.2018.11.156.
- [25] C. Weng, J. Sun, et H. Peng, « A unified open-circuit-voltage model of lithium-ion batteries for state-of-charge estimation and state-of-health monitoring », *Journal of Power Sources*, vol. 258, p. 228-237, juill. 2014, doi: 10.1016/j.jpowsour.2014.02.026.
- [26] Q.-Q. Yu, R. Xiong, L.-Y. Wang, et C. Lin, « A Comparative Study on Open Circuit Voltage Models for Lithium-ion Batteries », *Chin. J. Mech. Eng.*, vol. 31, n° 1, p. 65, déc. 2018, doi: 10.1186/s10033-018-0268-8.
- [27] L. Lavigne, J. Sabatier, J. M. Francisco, F. Guillemard, et A. Noury, « Lithium-ion Open Circuit Voltage (OCV) curve modelling and its ageing adjustment », *Journal of Power Sources*, vol. 324, p. 694-703, 2016, doi: 10.1016/j.jpowsour.2016.05.121.
- [28] I. Baghdadi, « Prise en compte des modes de vieillissement dans la modélisation des performances de batteries lithium-ion pour l'évaluation de leur durée de vie en usage automobile », Université de Bordeaux, 2017.
- [29] M. T. Todinov, « Necessary and sufficient condition for additivity in the sense of the Palmgren-Miner rule », *Computational Materials Science*, p. 10, 2001.
- [30] A. DELAILLE *et al.*, « SIMCAL Project: calendar aging results obtained on a panel of 6 Production Li-ion cells », in *224ème Electrochemical Energy Summit de l'Electrochemical Society*, San Fransisco, United States, oct. 2013, p. 1 p, Consulté le: mars 04, 2020. [En ligne]. Disponible sur: <https://hal.archives-ouvertes.fr/hal-00920366>.
- [31] P. Gyan *et al.*, « Experimental Assessment of Battery Cycle Life Within the SIMSTOCK Research Program », *Oil Gas Sci. Technol. – Rev. IFP Energies nouvelles*, vol. 68, n° 1, p. 137-147, janv. 2013, doi: 10.2516/ogst/2013106.
- [32] S. Grolleau *et al.*, « Calendar aging of Production graphite/LiFePO<sub>4</sub> cell – Predicting capacity fade under time dependent storage conditions », *Journal of Power Sources*, vol. 255, p. 450-458, juin 2014, doi: 10.1016/j.jpowsour.2013.11.098.
- [33] J. Wang *et al.*, « Cycle-life model for graphite-LiFePO<sub>4</sub> cells », *Journal of Power Sources*, vol. 196, n° 8, p. 3942-3948, avr. 2011, doi: 10.1016/j.jpowsour.2010.11.134.
- [34] I. Bloom *et al.*, « An accelerated calendar and cycle life study of Li-ion cells », *Journal of Power Sources*, vol. 101, n° 2, p. 238-247, oct. 2001, doi: 10.1016/S0378-7753(01)00783-2.
- [35] J. de Hoog *et al.*, « Combined cycling and calendar capacity fade modeling of a Nickel-Manganese-Cobalt Oxide Cell with real-life profile validation », *Applied Energy*, vol. 200, p. 47-61, août 2017, doi: 10.1016/j.apenergy.2017.05.018.
- [36] M. Makdessi, A. Sari, et P. Venet, « Metallized polymer film capacitors ageing law based on capacitance degradation », *Microelectronics Reliability*, vol. 54, n° 9, p. 1823-1827, sept. 2014, doi: 10.1016/j.microrel.2014.07.103.
- [37] J. Schmalstieg, S. Käbitz, M. Ecker, et D. U. Sauer, « A holistic aging model for Li(NiMnCo)O<sub>2</sub> based 18650 lithium-ion batteries », *Journal of Power Sources*, vol. 257, p. 325-334, juill. 2014, doi: 10.1016/j.jpowsour.2014.02.012.
- [38] A. Marongiu, M. Roscher, et D. U. Sauer, « Influence of the vehicle-to-grid strategy on the aging behavior of lithium battery electric vehicles », *Applied Energy*, vol. 137, p. 899-912, janv. 2015, doi: 10.1016/j.apenergy.2014.06.063.
- [39] J. Purewal, J. Wang, J. Graetz, S. Soukiazian, H. Tataria, et M. W. Verbrugge, « Degradation of lithium ion batteries employing graphite negatives and nickel-cobalt-manganese oxide + spinel manganese oxide positives: Part 2, chemical-mechanical degradation model », *Journal of Power Sources*, vol. 272, p. 1154-1161, déc. 2014, doi: 10.1016/j.jpowsour.2014.07.028.

- [40] M. Broussely, S. Herreyre, P. Biensan, P. Kasztejna, K. Nechev, et R. J. Staniewicz, « Aging mechanism in Li ion cells and calendar life predictions », *Journal of Power Sources*, vol. 97-98, p. 13-21, juill. 2001, doi: 10.1016/S0378-7753(01)00722-4.
- [41] N. Kamyab, J. W. Weidner, et R. E. White, « Mixed Mode Growth Model for the Solid Electrolyte Interface (SEI) », *J. Electrochem. Soc.*, vol. 166, n° 2, p. A334-A341, janv. 2019, doi: 10.1149/2.1101902jes.
- [42] E. Peled et S. Menkin, « Review—SEI: Past, Present and Future », *J. Electrochem. Soc.*, vol. 164, n° 7, p. A1703-A1719, janv. 2017, doi: 10.1149/2.1441707jes.
- [43] F. Single, B. Horstmann, et A. Latz, « Revealing SEI Morphology: In-Depth Analysis of a Modeling Approach », *Journal of The Electrochemical Society*, vol. 164, n° 11, p. E3132-E3145, 2017, doi: 10.1149/2.0121711jes.
- [44] D. Li, D. Danilov, Z. Zhang, H. Chen, Y. Yang, et P. H. Notten, « Modeling the SEI-formation on graphite electrodes in LiFePO<sub>4</sub> batteries », *Journal of The Electrochemical Society*, vol. 162, n° 6, p. A858–A869, 2015.
- [45] C. Kupper et W. G. Bessler, « Multi-Scale Thermo-Electrochemical Modeling of Performance and Aging of a LiFePO<sub>4</sub>/Graphite Lithium-Ion Cell », *J. Electrochem. Soc.*, vol. 164, n° 2, p. A304, déc. 2016, doi: 10.1149/2.0761702jes.
- [46] A. Deshpande, S. Phul, et B. Krishnamurthy, « A generalized mathematical model to understand the capacity fading in lithium ion batteries-effects of solvent and lithium transport », *Journal of Electrochemical Science and Engineering*, vol. 5, n° 3, Art. n° 3, sept. 2015, doi: 10.5599/jese.197.
- [47] M. Safari, M. Morcrette, A. Teyssot, et C. Delacourt, « Life-Prediction Methods for Lithium-Ion Batteries Derived from a Fatigue Approach: I. Introduction: Capacity-Loss Prediction Based on Damage Accumulation », *J. Electrochem. Soc.*, vol. 157, n° 6, p. A713, avr. 2010, doi: 10.1149/1.3374634.
- [48] H. J. Plöehn, P. Ramadass, et R. E. White, « Solvent Diffusion Model for Aging of Lithium-Ion Battery Cells », *J. Electrochem. Soc.*, vol. 151, n° 3, p. A456-A462, janv. 2004, doi: 10.1149/1.1644601.
- [49] N. Dufour, M. Chandesris, S. Genies, Mikaël Cugnet, et Y. Bultel, « Lithiation heterogeneities of graphite according to C-rate and mass-loading: A model study », *Electrochimica Acta*, vol. 272, p. 97-107, 2018, doi: 10.1016/j.electacta.2018.03.196.
- [50] M. Safari, M. Morcrette, A. Teyssot, et C. Delacourt, « Multimodal Physics-Based Aging Model for Life Prediction of Li-Ion Batteries », *J. Electrochem. Soc.*, vol. 156, n° 3, p. A145-A153, janv. 2009, doi: 10.1149/1.3043429.
- [51] C. Delacourt et M. Safari, « Life Simulation of a Graphite/LiFePO<sub>4</sub> Cell under Cycling and Storage », *J. Electrochem. Soc.*, vol. 159, n° 8, p. A1283-A1291, janv. 2012, doi: 10.1149/2.049208jes.
- [52] M. B. Pinson et M. Z. Bazant, « Theory of SEI Formation in Rechargeable Batteries: Capacity Fade, Accelerated Aging and Lifetime Prediction », *J. Electrochem. Soc.*, vol. 160, n° 2, p. A243-A250, 2011.
- [53] A. Banerjee *et al.*, « Review—Multifunctional Materials for Enhanced Li-Ion Batteries Durability: A Brief Review of Practical Options », *J. Electrochem. Soc.*, vol. 164, n° 1, p. A6315, janv. 2017, doi: 10.1149/2.0451701jes.
- [54] K. Edstrom, M. Herstedt, et D. P. Abraham, « A new look at the solid electrolyte interphase on graphite anodes in Li-ion batteries », *Journal of Power Sources*, vol. 153, n° 2, p. 380–384, 2006, doi: 10.1016/j.jpowsour.2005.05.062.
- [55] L. Liu et M. Zhu, « Modeling of SEI Layer Growth and Electrochemical Impedance Spectroscopy Response using a Thermal-Electrochemical Model of Li-ion Batteries », *ECS Trans.*, vol. 61, n° 27, p. 43-61, janv. 2014, doi: 10.1149/06127.0043ecst.
- [56] H. Ekström et G. Lindbergh, « A Model for Predicting Capacity Fade due to SEI Formation in a Production Graphite/LiFePO<sub>4</sub> Cell », *J. Electrochem. Soc.*, vol. 162, n° 6, p. A1003-A1007, janv. 2015, doi: 10.1149/2.0641506jes.
- [57] M. Dubarry, C. Truchot, et B. Y. Liaw, « Synthesize battery degradation modes via a diagnostic and prognostic model », *Journal of Power Sources*, vol. 219, p. 204-216, déc. 2012, doi: 10.1016/j.jpowsour.2012.07.016.
- [58] Z. Ma, Z. Wang, R. Xiong, et J. Jiang, « A mechanism identification model based state-of-health diagnosis of lithium-ion batteries for energy storage applications », *Journal of Cleaner Production*, vol. 193, p. 379-390, août 2018, doi: 10.1016/j.jclepro.2018.05.074.
- [59] X. Han, M. Ouyang, L. Lu, J. Li, Y. Zheng, et Z. Li, « A comparative study of Production lithium ion battery cycle life in electrical vehicle: Aging mechanism identification », *Journal of Power Sources*, vol. 251, p. 38-54, avr. 2014, doi: 10.1016/j.jpowsour.2013.11.029.
- [60] S. Schindler et M. A. Danzer, « A novel mechanistic modeling framework for analysis of electrode balancing and degradation modes in Production lithium-ion cells », *Journal of Power Sources*, vol. 343, p. 226-236, 2017, doi: 10.1016/j.jpowsour.2017.01.026.
- [61] X. Feng *et al.*, « Characterization of large format lithium ion battery exposed to extremely high temperature », *Journal of Power Sources*, vol. 272, n° Supplement C, p. 457-467, 2014, doi: 10.1016/j.jpowsour.2014.08.094.
- [62] M. A. Roscher et D. U. Sauer, « Dynamic electric behavior and open-circuit-voltage modeling of LiFePO<sub>4</sub>-based lithium ion secondary batteries », *Journal of Power Sources*, vol. 196, n° 1, p. 331-336, janv. 2011, doi: 10.1016/j.jpowsour.2010.06.098.
- [63] T. Lu, Y. Luo, Y. Zhang, W. Luo, L. Yan, et J. Xie, « Degradation Analysis of Production Lithium-Ion Battery in Long-Term Storage », *Journal of The Electrochemical Society*, vol. 164, n° 4, p. A775-A784, 2017, doi: 10.1149/2.1321704jes.
- [64] A. Marongiu, N. Nlandi, Y. Rong, et D. U. Sauer, « On-board capacity estimation of lithium iron phosphate batteries by means of half-cell curves », *Journal of Power Sources*, vol. 324, p. 158-169, août 2016, doi: 10.1016/j.jpowsour.2016.05.041.

- [65] N. Damay, G. Friedrich, C. Forgez, M. Juston, et K. Mergo Mbeya, *Off-line method to determine the electrode balancing of Li-ion batteries*. 2020.
- [66] J. Groot, *State-of-health estimation of Li-ion batteries: Ageing models*. Chalmers University of Technology, 2014.
- [67] « Li-Ion Battery Advantages / Disadvantages: Lithium Ion » *Electronics Notes* ». [https://www.electronics-notes.com/articles/electronic\\_components/battery-technology/li-ion-lithium-ion-advantages-disadvantages.php](https://www.electronics-notes.com/articles/electronic_components/battery-technology/li-ion-lithium-ion-advantages-disadvantages.php) (consulté le mai 14, 2020).
- [68] P. Gyan *et al.*, « Experimental Assessment of Battery Cycle Life Within the SIMSTOCK Research Program », *Oil Gas Sci. Technol. – Rev. IFP Energies nouvelles*, vol. 68, n° 1, Art. n° 1, janv. 2013, doi: 10.2516/ogst/2013106.
- [69] S. Belaid, R. Mingant, M. Petit, J. Martin, et J. Bernard, « Strategies to extend the lifespan of automotive batteries through battery modeling and system simulation: The MOBICUS project », 2018, vol. 2018-January, p. 1-9, doi: 10.1109/VPPC.2017.8330949.
- [70] M. Ben-Marzouk, A. Chaumond, E. Redondo-Iglesias, M. Montaru, et S. Pélissier, « Experimental Protocols and First Results of Calendar and/or Cycling Aging Study of Lithium-Ion Batteries – the MOBICUS Project », *World Electric Vehicle Journal*, vol. 8, n° 2, p. 388-397, juin 2016, doi: 10.3390/wevj8020388.
- [71] B. Pilipili Matadi, « Etude des mécanismes de vieillissement des batteries Li-ion en cyclage à basse température et en stockage à haute température : compréhension des origines et modélisation du vieillissement », thesis, Grenoble Alpes, 2017.
- [72] M. Broussely, « Aging Mechanisms and Calendar-Life : Predictions in Lithium-Ion Batteries », in *Advances in Lithium-Ion Batteries*, W. van Schalkwijk et B. Scrosati, Éd. Springer, 2002.
- [73] B. Y. Liaw, E. P. Roth, R. G. Jungst, G. Nagasubramanian, H. L. Case, et D. H. Doughty, « Correlation of Arrhenius behaviors in power and capacity fades with cell impedance and heat generation in cylindrical lithium-ion cells », *Journal of Power Sources*, vol. 119-121, p. 874-886, juin 2003, doi: 10.1016/S0378-7753(03)00196-4.
- [74] E. REDONDO-IGLESIAS, P. Venet, et S. Pelissier, « Eyring acceleration model for predicting calendar ageing of lithium-ion batteries », *Journal of Energy Storage*, vol. 13, p. 176-183, 2017, doi: 10.1016/j.est.2017.06.009.
- [75] « Development of a lifetime prediction model for lithium-ion batteries based on extended accelerated aging test data | Elsevier Enhanced Reader ». <https://reader.elsevier.com/reader/sd/pii/S0378775312008671?token=0FAF58172A5AC4664E47E5079B215F24B12811F8C35BF81A9296B646416A1ABA66615B5B5783F720BFE559F895BDF895> (consulté le janv. 26, 2020).
- [76] H. Wang, E. Rus, T. Sakuraba, J. Kikuchi, Y. Kiya, et H. D. Abruña, « CO<sub>2</sub> and O<sub>2</sub> Evolution at High Voltage Cathode Materials of Li-Ion Batteries: A Differential Electrochemical Mass Spectrometry Study », *Anal. Chem.*, vol. 86, n° 13, p. 6197-6201, juill. 2014, doi: 10.1021/ac403317d.
- [77] M. Onuki *et al.*, « Identification of the Source of Evolved Gas in Li-Ion Batteries Using #2#1 -labeled Solvents », *J. Electrochem. Soc.*, vol. 155, n° 11, p. A794, sept. 2008, doi: 10.1149/1.2969947.
- [78] B. Michalak, H. Sommer, D. Mannes, A. Kaestner, T. Brezesinski, et J. Janek, « Gas Evolution in Operating Lithium-Ion Batteries Studied In Situ by Neutron Imaging », *Sci Rep*, vol. 5, n° 1, p. 1-9, oct. 2015, doi: 10.1038/srep15627.
- [79] M. Broussely *et al.*, « Main aging mechanisms in Li ion batteries », *Journal of Power Sources*, vol. 146, n° 1, p. 90-96, août 2005, doi: 10.1016/j.jpowsour.2005.03.172.
- [80] Z. Mao, M. Farkhondeh, M. Pritzker, M. Fowler, et Z. Chen, « Calendar Aging and Gas Generation in Production Graphite/NMC-LMO Lithium-Ion Pouch Cell », *J. Electrochem. Soc.*, vol. 164, n° 14, p. A3469-A3483, 2017, doi: 10.1149/2.0241714jes.
- [81] Z. Ma, J. Jiang, W. Shi, W. Zhang, et C. C. Mi, « Investigation of path dependence in Production lithium-ion cells for pure electric bus applications: Aging mechanism identification », *Journal of Power Sources*, vol. 274, p. 29-40, janv. 2015, doi: 10.1016/j.jpowsour.2014.10.006.
- [82] A. M. Colclasure, K. A. Smith, et R. J. Kee, « Modeling detailed chemistry and transport for solid-electrolyte-interface (SEI) films in Li-ion batteries », *Electrochimica Acta*, vol. 58, p. 33-43, déc. 2011, doi: 10.1016/j.electacta.2011.08.067.
- [83] M. T. Lawder, P. W. C. Northrop, et V. R. Subramanian, « Model-Based SEI Layer Growth and Capacity Fade Analysis for EV and PHEV Batteries and Drive Cycles », *J. Electrochem. Soc.*, vol. 161, n° 14, p. A2099-A2108, 2014, doi: 10.1149/2.1161412jes.
- [84] A. Wang, S. Kadam, H. Li, S. Shi, et Y. Qi, « Review on modeling of the anode solid electrolyte interphase (SEI) for lithium-ion batteries », *npj Computational Materials*, vol. 4, n° 1, Art. n° 1, mars 2018, doi: 10.1038/s41524-018-0064-0.
- [85] « Capacity fade characteristics of lithium iron phosphate cell during dynamic cycle | Elsevier Enhanced Reader ». <https://reader.elsevier.com/reader/sd/pii/S0360544220312627?token=1EDA517AAB4FE3AB78AC0E49BA490F51C9D751049F06E6CBB1ACB2DFA2A0A61D46D5DD611704BE1587DE36DABF2D40DE> (consulté le oct. 30, 2020).
- [86] M. García-Plaza, J. Eloy-García Carrasco, A. Peña-Asensio, J. Alonso-Martínez, et S. Arnaltes Gómez, « Hysteresis effect influence on electrochemical battery modeling », *Electric Power Systems Research*, vol. 152, p. 27-35, nov. 2017, doi: 10.1016/j.epsr.2017.06.019.